Fluorine NMR Studies on the Dynamics and Structure of Biologically Active Peptides

by

Yuta Suzuki

A dissertation submitted in partial fulfillment
of the requirements for the degree of
Doctor of Philosophy
(Chemistry)
in the University of Michigan
2013

Doctoral Committee:

       Professor E. Neil G. Marsh, Chair
       Professor Carol A. Fierke
       Professor Vincent L. Pecoraro
       Professor Ayyalusamy Ramamoorthy
       Assistant Professor Matthew B. Soellner

Table of Contents

List of Figures

List of Tables

Abstract

Fluorine NMR Studies on the Dynamics and Structure of Biologically Active Peptides

By

Yuta Suzuki

Chair: E. Neil G. Marsh

^{19}F NMR is an excellent technique for studying changes in chemical environments due to its high sensitivity and large chemical shift dispersion. Since fluorine is not found in most biological systems, there is no competition from background signals, a problem that often afflicts measurements using ^{1}H, ^{13}C, and ^{15}N NMR. Therefore, it has been broadly applied to investigate protein conformational changes and dynamics as well as protein-ligand and protein-membrane interactions. In this thesis, ^{19}F NMR has been used to examine the structure and dynamics of biologically active peptides, including an antimicrobial peptide and amyloidogenic proteins.

Using a series of fluorinated MSI-78 antimicrobial peptides, a detailed examination how the structure and dynamics of the peptide changes on binding lipid bicelles was performed using ^{19}F chemical shifts, solvent isotope effects on chemical shifts, and changes in ^{19}F longitudinal and transverse relaxation rates. These results provide a detailed picture of the changes in the local chemical environment and peptide dynamics that occur when MSI-78 binds to the lipid bilayer.

Also described are direct, real-time measurements of amyloid formation for fluorinated islet amyloid polypeptide (IAPP) and Aβ, for which fiber formation is linked to type II diabetes

and Alzheimer's disease respectively. By using ^{19}F NMR, the consumption of monomeric peptides, rather than the formation of fibrils can be monitored. This study showed by comparing monomer depletion followed by ^{19}F NMR to fiber formation followed by thioflavin T (ThT) fluorescence assay that IAPP fibrillizes without accumulation of oligomeric intermediates. Inhibitory assays using ^{19}F NMR have suggested that ThT strongly competes with the amyloid inhibitor, epigallocatechin-3-gallate, for binding sites on IAPP fibers. In contrast to IAPP, time course studies using ^{19}F NMR have shown that small oligomers of Aβ accumulated. These types of experimental measurements are difficult to perform by other techniques, and the additional level of detail obtained by measuring the rate of monomer consumption by ^{19}F NMR might prove fruitful for further characterization of amyloid formation. Studies described in this thesis should contribute to develop the utility of ^{19}F NMR to investigate biological system as well as to help find potential therapeutic compounds.

Chapter 1

Introduction to the Use of ^{19}F NMR as a Probe in Biological System

1.1. Properties of Fluorine Nucleus and Its Advantages in NMR Studies

Fluorine is extremely rare in biological systems and has unique physical properties. Because it has the highest electronegativity of all the elements, the electronic properties of the C-F bonds are polarized in the opposite direction from C-H bonds (Figure 1.1). Fluorine is often considered as isosteric with hydrogen because the van der Waals radius of fluorine is 1.35 Å, similar to that of hydrogen (1.2 Å) even though C-F bond is significantly longer than C-H bond (~1.0 Å). Fluorine can usually replace hydrogen in small molecules with minimal effect on their binding to enzymes and proteins.
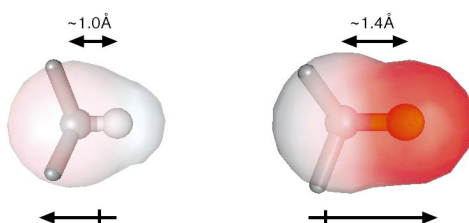
Figure 1.1. The properties of the carbon-hydrogen bond (left) and carbon-fluorine bond (right). The van der Waals surfaces are shaded according to the electrostatic potential. The image was taken from reference 5.

Fluorination therefore has been utilized extensively by the pharmaceutical industry to improve the pharmacokinetics and bioavailability of drugs (1-3). Because fluorocarbons are

highly chemically inert and hydrophobic, they have been used to modulate the physicochemical properties of proteins through the introduction of highly fluorinated amino acids in multiple positions (4, 5). In general, however, the substitution of hydrogen by fluorine does not appear to greatly change protein structures and activities (5-7).

The fluorine-19 (^{19}F) nucleus is a spin ½ nucleus, which exists in 100 % natural abundance, and therefore has excellent NMR properties comparable to that of proton NMR (83 % sensitivity relative to the proton) as shown in Table 1.1. One of the most useful features of ^{19}F NMR is the intrinsic sensitivity of the chemical shift of the fluorine nucleus to the local chemical environment. Fluorine chemical shift is more sensitive and larger than that of proton (Table 1.1) because the fluorine nucleus is surrounded by nine electrons rather than a single electron for hydrogen (8). Therefore, protein conformational changes (e.g. folding and unfolding, binding to small molecules, other proteins or lipid membrane) can be detected by 1D ^{19}F NMR (6, 7). Solvent (H_2O/D_2O) isotope effects on the fluorine chemical shift are also sensitive to study the structural changes of large proteins (7). The relaxation properties of the ^{19}F nucleus have also been utilized to provide information on protein dynamics. In addition, the large magnetogyric ratio translates into high sensitivity in 1D NMR spectroscopy as well as strong dipolar coupling that allows ^{19}F-^{19}F and ^{1}H-^{19}F Nuclear Overhauser effects (NOE) to be used to measure the distances between nuclei.

Another advantage is that fluorine is not found in most biological systems so that there is no overlap from background signals, a problem that often afflicts measurements using ^{1}H, ^{13}C, and ^{15}N NMR. This advantage potentially allows ^{19}F NMR spectroscopy to be used to study on multiple protein complexes as well as protein structural determination *in vivo*, where signals from the protein of interest are often attenuated in other NMR techniques. Therefore, the

incorporation of fluorine into biomolecules is a very attractive tool to investigate protein conformational changes and dynamics, enzyme mechanism, and protein-ligand and protein-membrane interactions in biological system.

Nucleus	Gyromagnetic ratio, rad^{-1} s^{-1} T × 10^{-7}	Natural Abundance (%)	NMR Frequency (MHz) at 11.75 T	Relative Sensitivity	Shift Parameter range (ppm)
^{1}H	26.7519	99.98	500	1.0	13
^{13}C	6.7283	1.108	125.7	0.0159	250
^{15}N	-2.712	0.37	50.7	0.00134	1700
^{19}F	25.181	100	470.4	0.83	400
^{31}P	10.841	100	200.2	0.066	530

Table 1.1. Properties of spin ½ nuclei. The image was adapted from reference 8.

1.2. Fluorinated Amino Acids as Probes in ^{19}F NMR

Various fluorinated amino acids have been synthesized, and some of them are now commercially available. Chemical structures of some of the ^{19}F labeled amino acid analogs utilized in ^{19}F NMR studies in chemical biology are shown in Figure 1.2. Fluorinated aromatic amino acid analogs including 4-fluorophenylalanine (4-fPhe) **1** (9-13), trifluoromethyl-phenylalanine (tfmPhe) **2** (13-16), 5-fluorotryptophan (5-fTrp) **3** (17-21), and 3-fluorotyrosine (3-fTyr) **4** (22-25) are commonly used for ^{19}F NMR studies because these analogs are easily incorporated into proteins by feeding. The syntheses of these amino acids are well established, and so they are generally commercially available. Fluorinated phenylalanine (Phe) **1, 2** and tryptophan (Trp) **3** are suitable probes for studying protein folding and unfolding since they are often in hydrophobic sites of the protein, thus in a buried environment in which the ^{19}F signal would shift or decrease due to the change of surrounding environment, as described in later

sections. 3-fTyr **4** has also been utilized to monitor structural changes and test surface exposure to bulk solvents using solvent isotope-induced chemical shift changes between H_2O and D_2O (23).
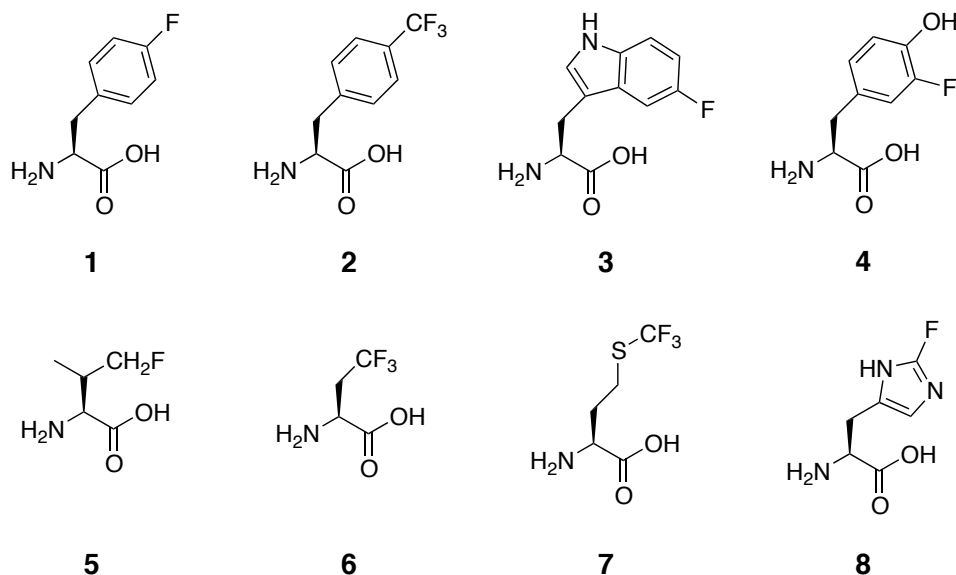
Figure 1.2. Representative chemical structures of fluorinated amino acid analogs utilized in ^{19}F NMR studies in biological systems.

^{19}F NMR studies have also been performed with fluorinated aliphatic amino acids including 5-fluoroleucine **5** (26), trifluoroethylglycine (tfeGly) **6** (27), trifluoromethionine (tfMet) **7** (28, 29), and 2-fluorohistidine **8** (30) as ^{19}F reporters to examine protein conformational changes. In addition to fluorinated amino acid analogs, fluorinated tags such as 2,2,2-trifluoroethanethiol (TFET) (7, 31, 32), are a complementary method to add ^{19}F probes into proteins as describe in section 1.3.

1.3. Synthesis of Fluorinated Proteins and Peptides

Incorporation of fluorinated probes into proteins and peptides can be accomplished in two ways: chemical modification of existing residues, or incorporation of fluorinated amino acids – either synthetically or biosynthetically. Chemical modification with fluorinated tags is often performed on nucleophillic side chains, most usually cysteine (Cys), either naturally present or introduced by mutagenesis (7, 31, 32). Although the preparation of proteins is generally straightforward, the addition of chemical probes might perturb the protein structure and/or activity depending on the size of probes.

Using fluorinated amino acids with Fluorenylmethyloxycarbonyl (Fmoc) or t-butyloxy-carbonyl (Boc) protection, peptides or proteins up to 50 residues (depending on sequence) can be synthesized by solid-phase peptide synthesis. Recently, native chemical ligation techniques have overcome this limitation and are able to synthesize proteins with about 200 hundred amino acids with several coupling steps (33-35). While peptide synthesis is straightforward and provides the high fidelity to incorporate at specific position(s), it becomes impractical to apply such a technique to medium – large size proteins.

Alternatively, biosynthetic techniques to substitute unnatural amino acids are applicable to incorporate some fluorinated amino acid analogs. An auxotrophic bacterial strain in a defined minimal media is often used to incorporate fluorinated amino acids such as 4-fPhe (9-13) **1**, 5-fTrp **3** (17-21), 3-fTyr **4** (22-25), and tfMet **7** (28, 29). Since this technique modifies all locations of one amino acid, it often results in the overlapping of signal peaks on ^{19}F NMR and is necessary to make mutations to assign ^{19}F signal peaks. In addition, this method usually does not achieve 100 % substitution of fluorinated amino acids; therefore, the heterogeneity of incorporation often causes difficulty for further studies. Multiple substitutions of fluorinated

amino acids in proteins would be beneficial to monitor different site protein dynamics and structural changes at the same time. To study specific positions in the protein, it is necessary to incorporate fluorinated amino acids site-specifically.

Lastly, Schultz and co-workers pioneered an orthogonal aminoacyl-tRNA synthase and tRNA pair for evolving proteins with an expanded genetic code to incorporate non-natural amino acids in specific positions on proteins of interest (36, 37). Recently, tfmPhe **2** were successfully incorporated into large proteins using this method as well as other non-canonical amino acids (13-15).

1.4. Application of Fluorinated Peptides and Proteins in ^{19}F NMR

1.4.1. Protein Unfolding and Folding

One of the most challenging aspects in protein folding is to detect the intermediate structures in this process. The difficulties in detecting intermediates are a consequence of their transient nature, heterogeneity, and low extent of accumulation. Frieden and colleagues overcame these difficulties by using ^{19}F NMR to examine intermediates during the folding process of rat intestinal fatty acid binding protein (IFABP) (10, 12). In this study, 4-fPhe **1** was incorporated as a ^{19}F probe to monitor the sequential IFABP folding steps using real-time ^{19}F NMR measurement (Figure 1.3). By monitoring eight 4-fPhe residues in IFABP, they detected a non-native like collapse in regions containing three 4-fPhes (4-fPhe-62, 68, and 93), suggesting there are conformational fluctuations during the folding process. The signals from these intermediates were decreased through cooperative rearrangement of the intermediates to form the final native structure. Because the detection of intermediates in protein folding is usually difficult, ^{19}F NMR would serve as a general method for study of protein folding processes.
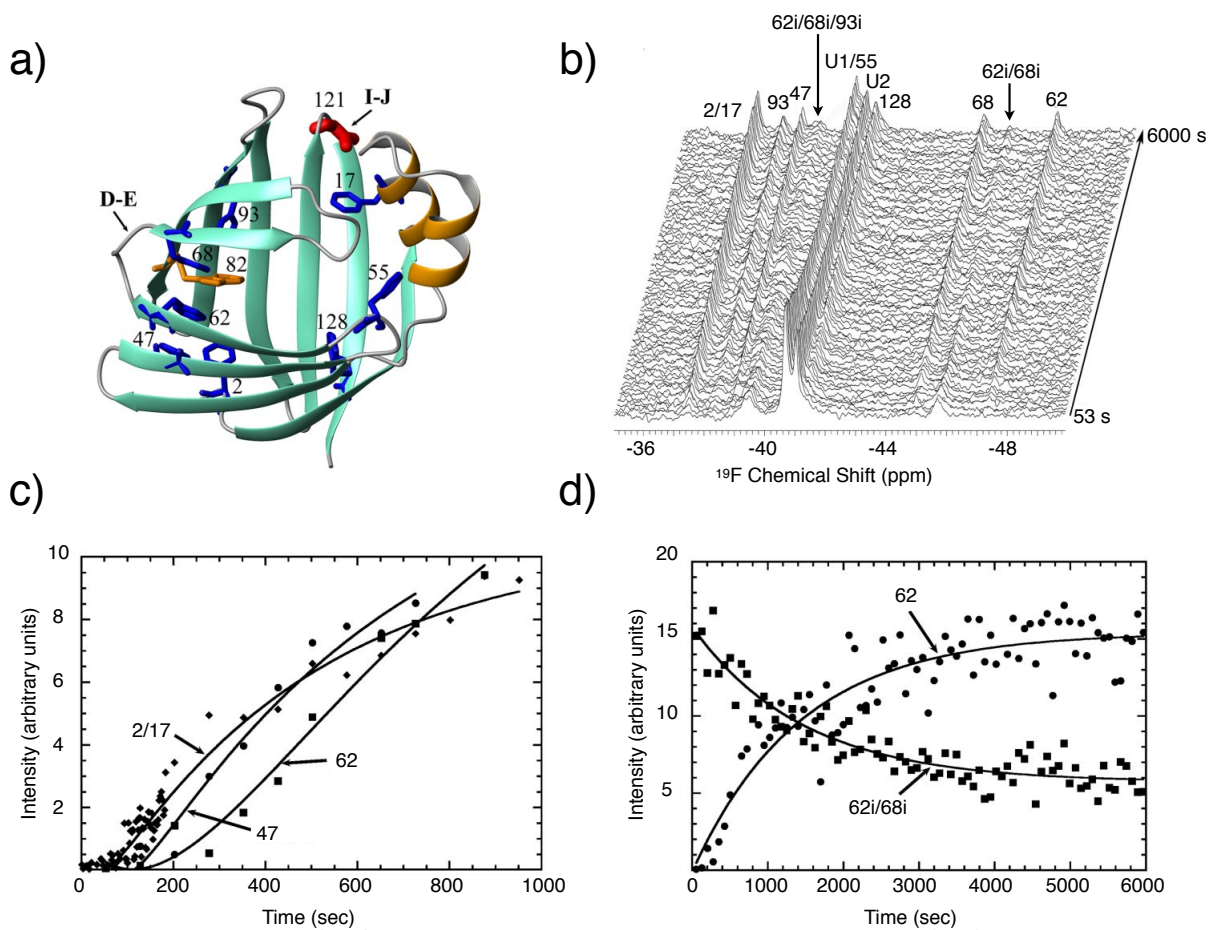
Figure 1.3. Real-time ^{19}F NMR experiments showing the kinetics of refolding of the G121V mutant of intestinal fatty acid binding protein labeled with 4-fPhe 1. (a) The crystal structure (Protein Data Bank entry 2IFB) of apo-IFABP. The location of eight Phe residues (blue), Trp-82 (gold), and the G121V mutation site are shown as red stick. (b) ^{19}F NMR kinetic spectra of ^{19}F labeled G121V IFBP right after diluting from 6 M to 1 M urea at 10 °C. Each ^{19}F spectrum corresponding to an average of 64 scans. (c) Plot of intensity changes for Phe-2/17, Phe-47 and Phe-62 in short time. (d) Plot of intensity changes of the disappearance of unfolding intermediates (Phe-62i/68i), and the appearance of the native folding state for Phe-62. The images were adapted from reference 10.

1.4.2. Protein-Small Molecule Interactions

The high sensitivity of the ^{19}F nucleus to the surrounding environment provides great advantages for ^{19}F NMR to investigate the structural changes accompanying proteins binding to natural ligands or inhibitors. Recently, the conformational changes of β$_2$-adrenergic receptor

(β_2AR) in complexes with various ligands were identified using ^{19}F NMR (Figure 1.4) (32).

Three native Cys residues in the cytoplasmic regions of the receptor were covalently linked with

TFET as ^{19}F probes. 1D ^{19}F NMR spectra showed changes in the relative populations of active

and inactive states of β_2AR due to different ligands binding. The structure-activity relationship

was determined by ^{19}F signal changes on two different labeling sites (Cys 265 and 327) as shown

in Figure 1.4.
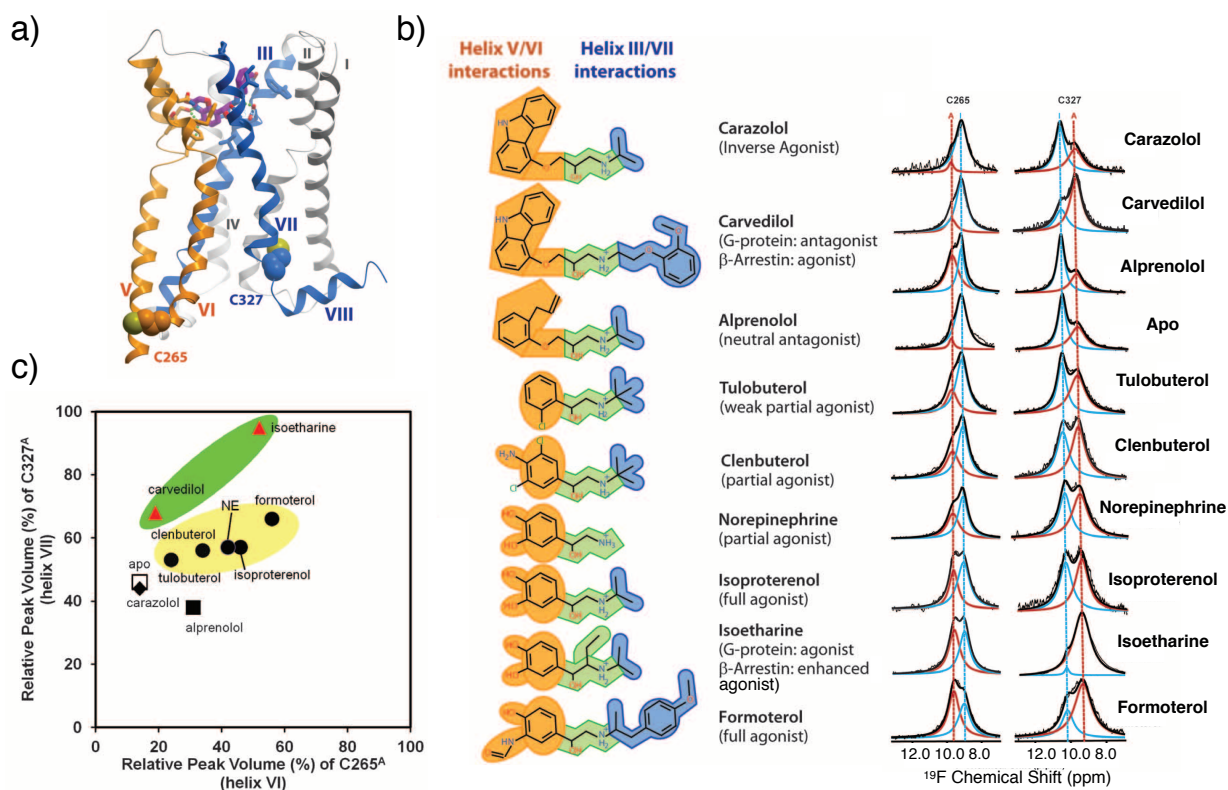
Figure 1.4. Two major conformation changes of β_2AR to ligand bindings were determined by ^{19}F NMR (a) The structure of active-state of β_2AR in the complex with the agonist BI-167107 (Protein Data Bank entry 3SN6). (b) Chemical structures, names and pharmacological efficacy of the ligands (left) and the relative population of active (red) and inactive (blue) states of β_2AR measured by the 1D ^{19}F NMR spectra (right). (c) Plot of the relative peak volumes for C265A versus C327A. The relative peak volume is calculated as the ratios of the active state volume and the sum of the active and inactive state volumes. Ligands are indicated as agonists (black circles with yellow background), biased ligands (red triangle with green background), and a neutral antagonist (black square), an inverse agonist (black diamond), and apo (open square). The images were taken from reference 32.

8

Characterization of inhibitors for protein-protein interactions was also recently achieved by observing of ^{19}F NMR signal changes (22). The utility of ^{19}F NMR in detecting protein-small molecule interactions could contribute as an analytical method to screen libraries of potential ligands for therapeutic uses.

1.4.3. Protein-Membrane Interactions

Many important biological processes involve interactions between proteins and lipid membranes. These interactions are often difficult and challenging to determine due to their dynamic and transient nature. Using ^{19}F NMR, Norton and his colleagues have studied interaction of the actinoporin equinatoxin II (EqTII), which is a family of sea anemone toxins that disrupts the cell membrane by pore formation (Figure 1.5) (21). To elucidate the binding interface of EqTII with lipid membranes, five Trp residues in this protein were replaced with 5-fTrp **3** (using a Trp auxotrophic strain of *E. coli*) because Trp residues are suggested to make key interactions with lipid membranes. Protein structural changes occurring upon the addition of lipid micelles or bicelles were followed using ^{19}F NMR. A large ^{19}F chemical shift for Trp 112 was observed in the presence of phospholipid micelles or bicelles. Further protein structural changes on model membranes were observed by following the chemical shift of Trp 116 upon the addition of sphingomyelin (SM). Through these experiments, the interaction and orientation of EqTII with respect to the lipid membrane could be deduced. Recently, an initial study for the interaction of antimicrobial peptide (AMP), MSI-78, with lipid bilayer was also performed in our laboratory as described later in this chapter (27, 38).
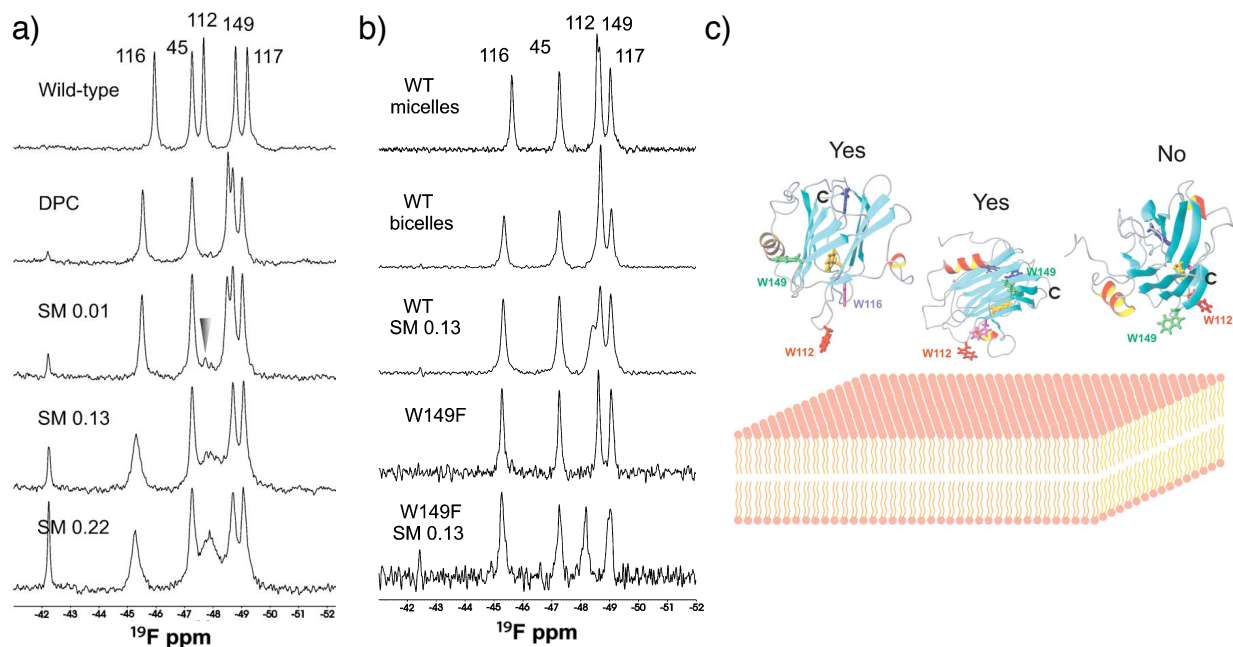
Figure 1.5. ¹⁹F NMR studies of the interaction of the actinoporin equinatoxin II with model membranes. (a) ¹⁹F NMR spectra of ¹⁹F labeled EqTII (described as wild type in figure) in DPC micelle with the addition of SM (ratio of SM to DPC was depicted next to each spectrum). (b) ¹⁹F NMR spectra of ¹⁹F labeled EqTIIs (WT of mutant W149F) in DMPC/DHPC bicelles in the absence or presence of SM. (c) Proposed models of the orientation of EqTII upon membrane binding based on ¹⁹F chemical shifts. The images were taken from reference 21.

1.4.4. In-cell Applications

Determination of protein dynamics and structural information in living cells is important for understanding how proteins function in their natural environment, which can be distinctly different from the condition employed *in vitro* studies. NMR signals from a protein of interest are hard to observe due to the crowded environment in the cell. This requires overexpressing the protein of interest and growing the cells on nutrients enriched with NMR active nuclei such as ¹⁵N or ¹³C to overcome the low signal of other cellular components. However, this approach

increases signal to noise ratio because label is also incorporated into other components in cell. In addition, protein leakage outside of the cell can cause artifacts for NMR measurements (39).

Since fluorine atoms usually are not found in biological systems and have 100% naturally abundant ½ spin nucleus processing high sensitivity (Table 1.1), ^{19}F NMR is attractive tool to investigate protein structures and dynamics in cells. Pielak and his co-workers have successfully examined both globular proteins (up to 100 kDa) and disordered proteins that incorporate the fluorinated amino acids, tfmPhe **2** and 3-fTyr **4** in detail (Figure 1.6) (13, 25).
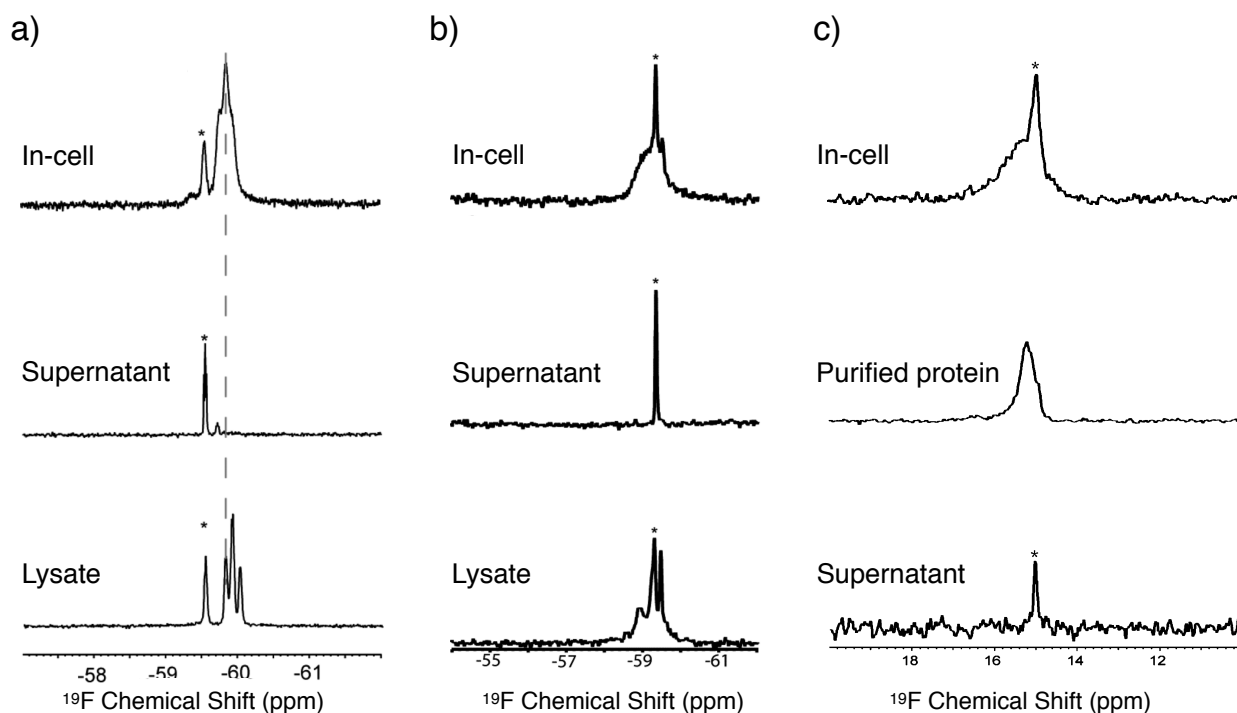
Figure 1.6. Protein ^{19}F NMR studies in *E. coli.* Representative 1D ^{19}F NMR spectra of α-synuclein (14.5 kDa) labeled with 3-fTyr **4** (a), calmodulin (16 kDa) labeled with 3-fTyr **4** (b), and histidinol dehydrogensase (98 kDa) labeled with tfmPhe **2** (c). Supernatant spectra were collected immediately after the in-cell spectra and taken to evaluate leakage, and lysate spectra were prepared from the supernatants of cleared lysates of in cell samples. The asterisks indicate the free 3-fTyr **4** resonances. Four other proteins are also tested in this study. The images were taken from reference 13.

In these studies, site-specific structural and dynamic information for proteins in cells was obtained from analysis of the fluorine chemical shift and line width. They could detect a small globular protein using ^{19}F NMR, even though it was difficult to detect same proteins using ^{15}N-^{1}H HSQC experiments (with use of ^{15}N-enriched proteins), because of the ten-fold increase of the rotational correlation times compared to diluted solution. In addition, they were able to measure protein leakage outside of cells, which caused artifacts for NMR measurements in their previous study (39). In the following studies, they have utilized ^{19}F NMR to understand crowding effects on protein stability (25). Since ^{19}F NMR spectra can be acquired in minutes (compared to one hour or more for ^{15}N-^{1}H HSQC experiments) on proteins at near physiological concentrations, it has the potential to monitor protein modifications involved in signal transduction and metabolism in real-time experiments (13).

1.5. Biologically Active Peptides

As described in Section 1.4, ^{19}F NMR is a unique and powerful tool to study protein structural changes, dynamics, and function. The goal of my research is to investigate the structure and dynamics of biologically active peptides, including the antimicrobial peptide MSI-78 (40) and amyloidogenic peptides (human islet amyloid polypeptide (IAPP) (41) and amyloid-beta (Aβ), whose amyloid formation are associated with type II diabetes and Alzheimer's disease, respectively) using ^{19}F NMR as a primary technique. In this section, the importance of further investigating antimicrobial and amyloid peptides are described.

1.5.1. Antimicrobial Peptides

The emergence of bacterial strains resistant to most of the clinically useful antibiotics has provided the motivation to develop new classes of antibiotics to combat these strains effectively. AMPs comprise a diverse family of membrane-active peptides and have shown promise as therapeutic agents against bacteria, fungi, and viruses. These peptides are formed as part of the innate immune system and also implicated in the activation of the adaptive immune response against microbes (Figure 1.7).

Although AMPs possess highly diverse sequences and structures, they share the property of being highly amphipathic, with one face of peptide being hydrophobic and the other face being a cluster of positively charged residues. The selectivity of AMPs for bacterial membranes arises primarily from electrostatic interactions between positively charged peptide and negatively charged phospholipids that predominate in bacterial cell membranes. Eukaryotic cell membranes are usually less subject to disruption by AMPs because they contain predominantly neutral phospholipids together with cholesterol that also helps in preventing disruption by AMP. Upon binding to the bacterial membrane, disruption of the membrane might proceed though a number of mechanisms including the formation of pores, membrane thinning, and detergent-like action (Figure 1.7).

Characterization of peptide-membrane interactions is challenging due to the transient nature of these interactions. In addition, the peptide may adopt different orientations with respect to the lipid membrane and have different oligomerization states that are concentration dependent. The structural models derived from solid-state NMR data are available for some AMPs bounds to lipid membranes; these experiments require higher concentration of peptide than their physiological active range (42-47). These include studies using fluorine-labeled AMPs to

provide information about peptide orientation in membranes. However, these experiments require peptide concentrations that are orders of magnitude higher than their physiologically active range, so it is not always clear whether such structures represent biologically active species.
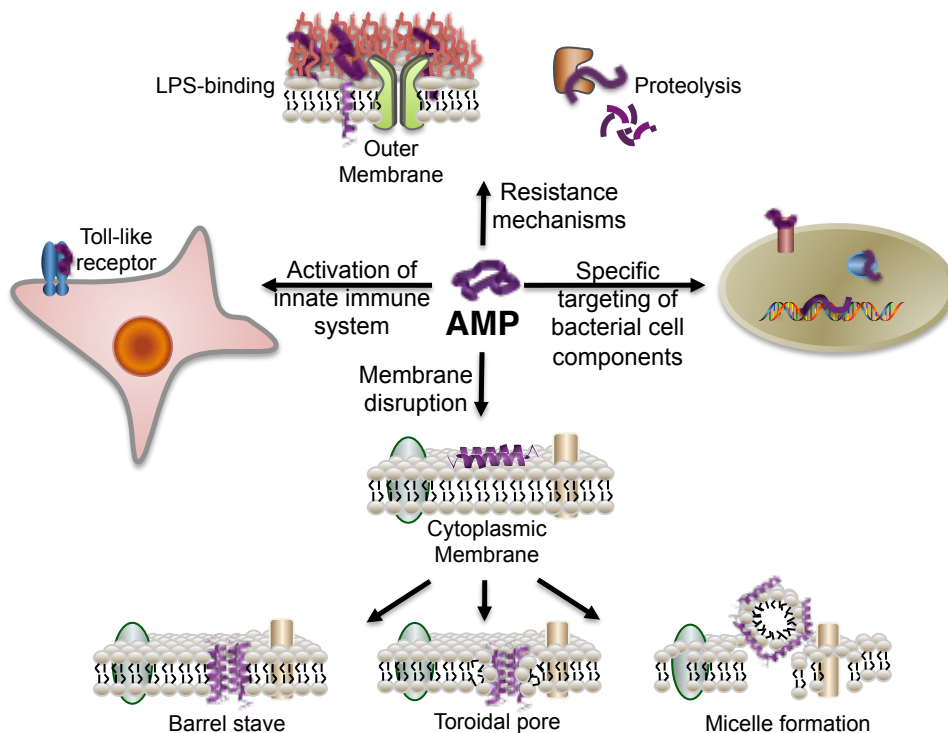
Figure 1.7. Summary of the broad range of cellular interactions associated with antimicrobial peptides. AMPs disrupt bacterial membranes with a number of mechanisms such as the formation of pores, membrane thinning, and detergent-like action. In addition, peptides might also interact with specific target proteins within microbial cells and activate the innate immune system. The binding of peptides to cell-surface lipopolysaccharides (LPS) molecules and proteolysis contribute to bacterial resistance to AMPs. The image was taken from reference 38.

In previous studies, our group and others have demonstrated that the incorporation of highly fluorinated amino acids in multiple sites into AMPs is an effective strategy for modulating their biological properties and can be used to study AMP interactions with membrane (48-51).

For example, we showed that incorporating hexafluoroleucine at four positions in the α-helical AMP MSI-78 resulted in increased potency toward some bacterial strains and protection against proteolysis when bound to lipid vesicles (49). The Marsh laboratory has now turned its attention to using fluorine-containing peptides to probe the interaction of AMPs with membranes by exploiting the sensitive NMR properties of the ^{19}F nucleus (27, 40).

1.5.2. Amyloid Peptides

The accumulation of misfolded proteins in protein aggregation, known as amyloid, is a hallmark of number of human disorders including neurodegenerative disorders such as Alzheimer's diseases and Parkinson's diseases and metabolic diseases such as type II diabetes (52-54). Protein conformational changes would facilitate the formation of amyloid, disrupting the regular function of protein and leading to the formation of toxic species. Even though the soluble precursor of these amyloidogenic proteins/peptides have diverse structures, such as globular proteins or largely unstructured peptides, the amyloid aggregates share common characteristics (Figure 1.8) (55). Under pathological conditions, the soluble precursor form of these proteins or peptides are triggered to self-assemble into long, linear and often twisted structures a few nanometers in diameter (56-58). Amyloid fibers generally exhibit a characteristic cross-β X-ray diffraction pattern, which indicates that the amyloid structure is composed of β-sheets running perpendicular to the fibril axis (59, 60). They also share the same optical behavior on binding affinity to certain dye molecules such as Congo red and Thioflavin T (ThT).
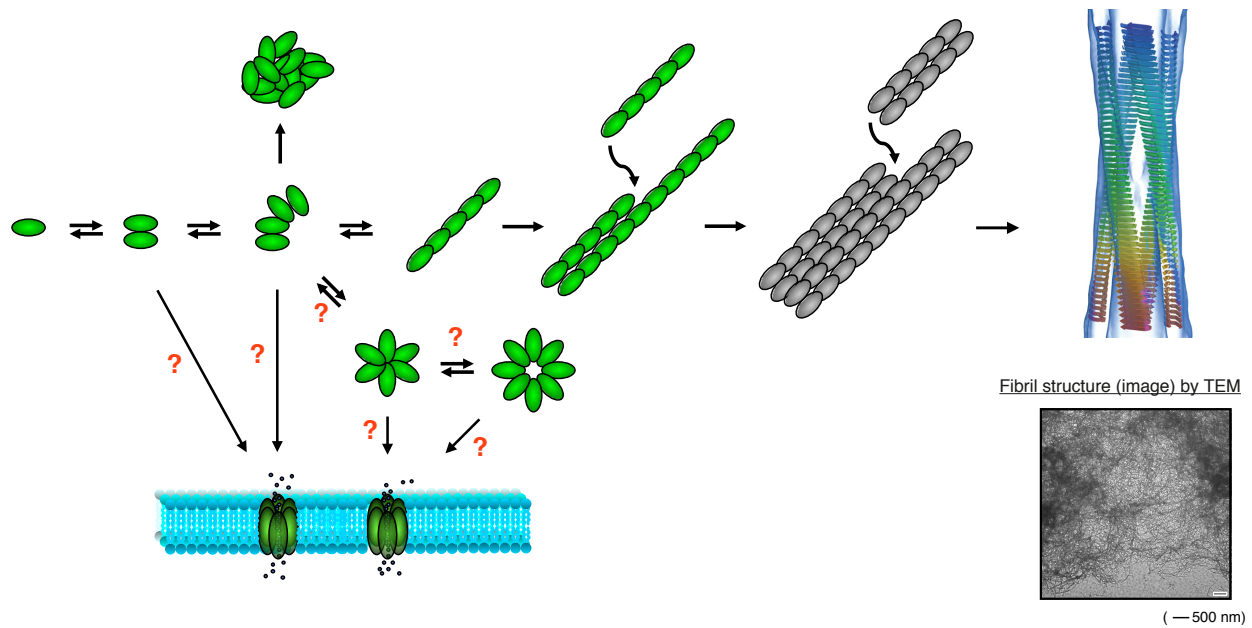
Figure 1.8. The proposed pathway of amyloid fiber formation. The formation of soluble oligomers is suggested to be involved in the amyloid fiber formation and the neurotoxic species. The accumulation of precursors result the formation of cross β-sheet sheet structure. The formation of aggregates is shown by transmission electron microscopy (TEM) image. It is also suggested that the oligomerization are induced on membrane surface, and the oligomeric species would disrupt the membrane by forming transmembrane pore or detergent-like process as AMPs (Figure 1.7) (61).

The most common method for measuring amyloid formation is to track the fluorescence increase when ThT binds to the fibers. The fibrillation of amyloid proteins is generally considered as a nucleation-dependent polymerization process consisting of two phases: a lag phase and an elongation phase (Figure 1.9) (61, 62). During a lag phase in the fibril formation, the monomeric peptides associate to form small oligomers. Nucleus formation is a thermodynamically unfavorable reaction, representing the rate-limiting step in amyloid fibril formation. After nucleation has occurred, the further addition of monomers becomes thermodynamically favorable, resulting in rapid growth of amyloid fibrils in the elongation period. Similarly, reporters of secondary structures such as circular dichroism (CD), Fourier transform infrared (FT-IR) and multidimensional NMR spectroscopy are commonly used to

track the formation of amyloid fiber as well as the ThT fluorescence assay.

The cytotoxicity of amyloid-related disorders was thought to be due to the insoluble amyloid fibrils, but now attention has shifted to soluble oligomeric intermediates formed during nucleation, which have recently been suggested to be more neurotoxic (63, 64). Therefore, the identification and characterization of oligomeric species formed as intermediates in the amyloid pathway is essential not only to understand the mechanism of fiber formation but also to develop the therapeutic molecules to treat these diseases. Unfortunately, the details of this process have been obscured by the limitations in the methods that can follow this reaction in real-time.
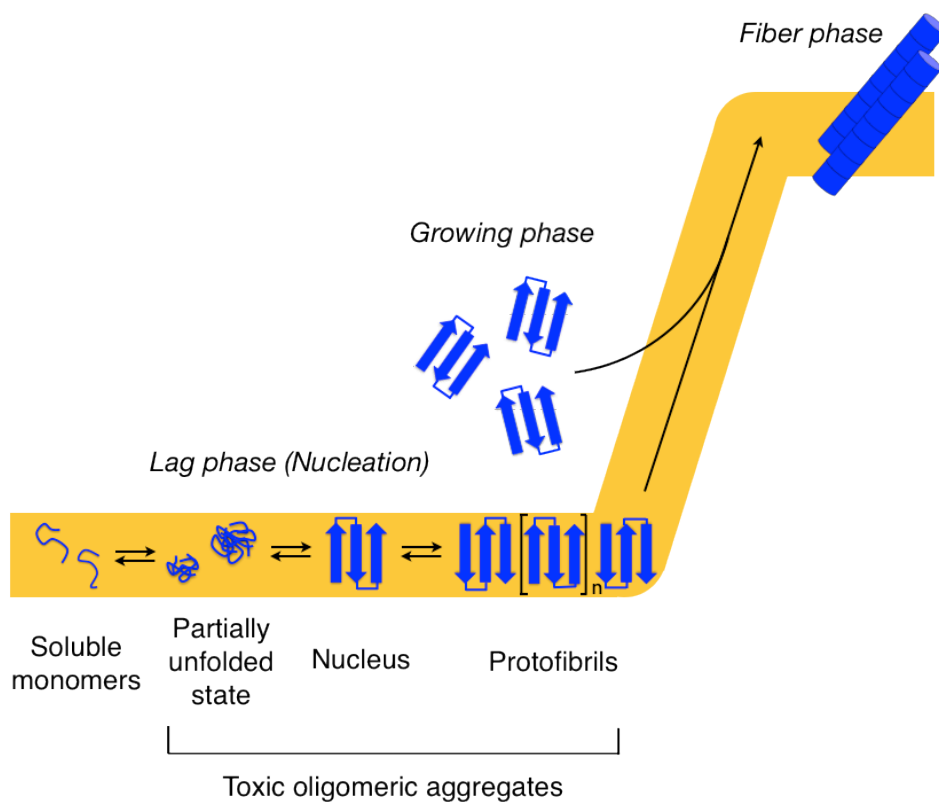
Figure 1.9. Illustration of the nucleation polymerization model for amyloid fibrillogenesis. Soluble precursors are self-assembled into oligomeric species in lag phase. The nucleus would elongate through the addition of monomers or other oligomers into the fibrils cooperatively and rapidly. The amyloid fibrils are thermodynamically stable and the product of this pathway. This process is generally shown as sigmoidal curve with ThT fluorescence assay. The image was adapted from reference 61.

1.6. Goals

Fluorinated amino acids have long been used as a sensitive and nonperturbing NMR probes to study protein dynamics and structural changes. Methods to incorporate fluorinated amino acids into peptides and proteins are well established and this can be accomplished in a variety of ways. The goal of my research is to use ^{19}F NMR as a tool to obtain the detailed structural and dynamic information for biologicaly important peptides including antimicrobial peptide (MSI-78) and amyloid peptides (IAPP and Aβ). The changes due to MSI-78 binding to lipids were measured by ^{19}F chemical shifts, solvent isotope effects on chemical shifts, and changes in longitudinal and transverse relaxation measurements of the ^{19}F nucleus (Chapter 2) (40). This study has provided a detailed picture of the local changes in the chemical environment of peptide dynamics that occurs when MSI-78 binds to the lipid bilayer.

I have also demonstrated the utility of ^{19}F NMR to make direct and real-time measurements of amyloid formation by monitoring monomeric peptide consumption. By comparing monomer depletion by ^{19}F NMR to fiber formation by ThT, I showed that IAPP fibrillizes with no formation of oligomeric intermediates (Chapter 3) (41). To further develop the usage of ^{19}F NMR, I have also measured the interaction of polyphenolic inhibitor (epigallocatechin-3-gallate (EGCG)) with IAPP. In contrast to IAPP fiber formation, it has been possible to detect the formation of small oligomers of Aβ peptides using ^{19}F NMR (Chapter 4).

This research aims to contribute to demonstrate the utility of ^{19}F NMR in chemical biology. ^{19}F NMR cannot only be applied to studying changes of protein structure and dynamics in solution NMR as shown in this thesis but also to investigating these structure changes using solid phase NMR. In addition, this technique is able to apply to magnetic resonance imaging (MRI) *in vivo* studies. The long-term goal of using ^{19}F NMR would be to use it as a tool to help

find potential therapeutic compounds.

1.7. References

1.   Begue, J. P., and Bonnet-Delpon, D. (2006) Recent advances (1995-2005) in fluorinated pharmaceuticals based on natural products, *J. Fluorine Chem. 127*, 992-1012.

2.   Purser, S., Moore, P. R., Swallow, S., and Gouverneur, V. (2008) Fluorine in medicinal chemistry, *Chem. Soc. Rev. 37*, 320-330.

3.   Muller, K., Faeh, C., and Diederich, F. (2007) Fluorine in pharmaceuticals: Looking beyond intuition, *Science 317*, 1881-1886.

4.   Buer, B. C., and Marsh, E. N. G. (2012) Fluorine: A new element in protein design, *Protein Sci. 21*, 453-462.

5.   Marsh, E. N. G. (2000) Towards the nonstick egg: designing fluorous proteins, *Chem. Biol. 7*, R153-R157.

6.   Cobb, S. L., and Murphy, C. D. (2009) ^{19}F NMR applications in chemical biology, *J. Fluorine Chem. 130*, 132-143.

7.   Kitevski-LeBlanc, J. L., and Prosser, R. S. (2012) Current applications of ^{19}F NMR to studies of protein structure and dynamics, *Prog. Nucl. Magn. Reson. Spectrosc. 62*, 1-33.

8.   Gerig, J. T. (2001) Fluorine NMR. Online textbook <http://www.biophysics.org/ Portals/1/PDFs/Education/gerig.pdf>

9.   Li, C., Lutz, E. A., Slade, K. M., Ruf, R. A., Wang, G. F., and Pielak, G. J. (2009) ^{19}F NMR studies of α-synuclein conformation and fibrillation, *Biochemistry 48*, 8578-8584.

10.   Li, H., and Frieden, C. (2007) Observation of sequential steps in the folding of intestinal fatty acid binding protein using a slow folding mutant and ^{19}F NMR, *Proc. Natl. Acad. Sci. U.S.A. 104*, 11993-11998.

11.   Li, H., and Frieden, C. (2007) Comparison of C40/82A and P27A C40/82A barstar mutants using ^{19}F NMR, *Biochemistry 46*, 4337-4347.

12.   Li, H., and Frieden, C. (2005) NMR studies of 4-^{19}F-phenylalanine-labeled intestinal fatty acid binding protein: Evidence for conformational heterogeneity in the native state, *Biochemistry 44*, 2369-2377.

13. Li, C., Wang, G. F., Wang, Y., Creager-Allen, R., Lutz, E. A., Scronce, H., Slade, K. M., Ruf, R. A., Mehl, R. A., and Pielak, G. J. (2010) Protein ^{19}F NMR in Escherichia coli, *J. Am. Chem. Soc. 132*, 321-327.

14. Jackson, J. C., Hammill, J. T., and Mehl, R. A. (2007) Site-specific incorporation of a [19]F -amino acid into proteins as an NMR probe for characterizing protein structure and reactivity, *J. Am. Chem. Soc. 129*, 1160-1166.

15. Wang, G. F., Li, C., and Pielak, G. J. (2010) Probing the micelle-bound aggregation-prone state of alpha-synuclein with ^{19}F NMR spectroscopy, *ChemBioChem 11*, 1993-1996.

16. Loscha, K. V., Herlt, A. J., Qi, R. H., Huber, T., Ozawa, K., and Otting, G. (2012) Multiple-Site Labeling of Proteins with Unnatural Amino Acids, *Angew. Chem. Int. Ed. 51*, 2243-2246.

17. Evanics, F., Bezsonova, I., Marsh, J., Kitevski, J. L., Forman-Kay, J. D., and Prosser, R. S. (2006) Tryptophan solvent exposure in folded and unfolded states of an SH3 domain by ^{19}F and ^{1}H NMR, *Biochemistry 45*, 14120-14128.

18. Peersen, O. B., Pratt, E. A., Truong, H. T. N., Ho, C., and Rule, G. S. (1990) Site-Specific Incorporation of 5-Fluorotryptophan as a Probe of the Structure and Function of the Membrane-Bound D-Lactate Dehydrogenase of Escherichia-Coli - a [19]F Nuclear-Magnetic-Resonance Study, *Biochemistry 29*, 3256-3262.

19. Luck, L. A., and Falke, J. J. (1991) ^{19}F NMR - Studies of the D-Galactose Chemosensory Receptor .1. Sugar Binding Yields a Global Structural-Change, *Biochemistry 30*, 4248-4256.

20. Luck, L. A., Vance, J. E., OConnell, T. M., and London, R. E. (1996) ^{19}F NMR relaxation studies on 5-fluorotryptophan- and tetradeutero-5-fluorotryptophan-labeled E-coli glucose/galactose receptor, *J. Biomol. NMR 7*, 261-272.

21. Anderluh, G., Razpotnik, A., Podlesek, Z., Macek, P., Separovic, F., and Norton, R. S. (2005) Interaction of the eukaryotic pore-forming cytolysin equinatoxin II with model membranes: ^{19}F NMR studies, *J. Mol. Biol. 347*, 27-39.

22. Pomerantz, W. C., Wang, N., Lipinski, A. K., Wang, R., Cierpicki, T., and Mapp, A. K. (2012) Profiling the dynamic interfaces of fluorinated transcription complexes for ligand discovery and characterization, *ACS Chem. Biol. 7*, 1345-1350.

23. Evanics, F., Kitevski, J. L., Bezsonova, I., Forman-Kay, J., and Prosser, R. S. (2007) ^{19}F NMR studies of solvent exposure and peptide binding to an SH3 domain, *Bba-Gen Subjects 1770*, 221-230.

24. Eccleston, J. F., Molloy, D. P., Hinds, M. G., King, R. W., and Feeney, J. (1993) Conformational Differences between Complexes of Elongation-Factor Tu Studied by ^{19}F -NMR Spectroscopy, *Eur. J. Biochem. 218*, 1041-1047.

25. Schlesinger, A. P., Wang, Y., Tadeo, X., Millet, O., and Pielak, G. J. (2011) Macromolecular crowding fails to fold a globular protein in cells, *J. Am. Chem. Soc. 133*, 8082-8085.

26. Feeney, J., McCormick, J. E., Bauer, C. J., Birdsall, B., Moody, C. M., Starkmann, B. A., Young, D. W., Francis, P., Havlin, R. H., Arnold, W. D., and Oldfield, E. (1996) ^{19}F nuclear magnetic resonance chemical shifts of fluorine containing aliphatic amino acids in proteins: Studies on Lactobacillus casei dihydrofolate reductase containing (2S,4S)-5-fluoroleucine, *J. Am. Chem. Soc. 118*, 8700-8706.

27. Buer, B. C., Chugh, J., Al-Hashimi, H. M., and Marsh, E. N. G. (2010) Using fluorine nuclear magnetic resonance to probe the interaction of membrane-active peptides with the lipid bilayer, *Biochemistry 49*, 5760-5765.

28. Holzberger, B., Rubini, M., Moller, H. M., and Marx, A. (2010) A Highly Active DNA Polymerase with a Fluorous Core, *Angew. Chem. Int. Ed. 49*, 1324-1327.

29. Duewel, H., Daub, E., Robinson, V., and Honek, J. F. (1997) Incorporation of trifluoromethionine into a phage lysozyme: Implications and a new marker for use in protein ^{19}F NMR, *Biochemistry 36*, 3404-3416.

30. Eichler, J. F., Cramer, J. C., Kirk, K. L., and Bann, J. G. (2005) Biosynthetic incorporation of fluorohistidine into proteins in E-coli: A new probe of macromolecular structure, *ChemBioChem 6*, 2170-2173.

31. Klein-Seetharaman, J., Getmanova, E. V., Loewen, M. C., Reeves, P. J., and Khorana, H. G. (1999) NMR spectroscopy in studies of light-induced structural changes in mammalian rhodopsin: Applicability of solution ^{19}F NMR, *Proc. Natl. Acad. Sci. U.S.A. 96*, 13744-13749.

32. Liu, J. J., Horst, R., Katritch, V., Stevens, R. C., and Wuthrich, K. (2012) Biased signaling pathways in β2-adrenergic receptor characterized by ^{19}F -NMR, *Science 335*, 1106-1110.

33. Kent, S. B. H. (2009) Total chemical synthesis of proteins, *Chem. Soc. Rev. 38*, 338-351.

34. Dawson, P. E., and Kent, S. B. H. (2000) Synthesis of native proteins by chemical ligation, *Annu. Rev. Biochem. 69*, 923-960.

35. Dawson, P. E., Muir, T. W., Clarklewis, I., and Kent, S. B. H. (1994) Synthesis of Proteins by Native Chemical Ligation, *Science 266*, 776-779.

36. Wang, L., Brock, A., Herberich, B., and Schultz, P. G. (2001) Expanding the genetic code of Escherichia coli, *Science 292*, 498-500.

37. Wang, L., Xie, J., and Schultz, P. G. (2006) Expanding the genetic code, *Annu. Rev. Biophys. Biomol. Struct. 35*, 225-249.

38. Marsh, E. N. G., Buer, B. C., and Ramamoorthy, A. (2009) Fluorine - a new element in the design of membrane-active peptides, *Mol. BioSyst. 5*, 1143-1147.

39. Bryant, J. E., Lecomte, J. T. J., Lee, A. L., Young, G. B., and Pielak, G. J. (2007) Protein dynamics in living cells (Retraction of vol 44, pg 9275, 2005), *Biochemistry 46*, 8206-8206.

40. Suzuki, Y., Buer, B. C., Al-Hashimi, H. M., and Marsh, E. N. G. (2011) Using Fluorine Nuclear Magnetic Resonance To Probe Changes in the Structure and Dynamics of Membrane-Active Peptides Interacting with Lipid Bilayers, *Biochemistry 50*, 5979-5987.

41. Suzuki, Y., Brender, J. R., Hartman, K., Ramamoorthy, A., and Marsh, E. N. G. (2012) Alternative Pathways of Human Islet Amyloid Polypeptide Aggregation Distinguished by [19]F Nuclear Magnetic Resonance-Detected Kinetics of Monomer Consumption, *Biochemistry 51*, 8154-8162

42. Ramamoorthy, A., Thennarasu, S., Lee, D. K., Tan, A., and Maloy, L. (2006) Solid-state NMR investigation of the membrane-disrupting mechanism of antimicrobial peptides MSI-78 and MSI-594 derived from magainin 2 and melittin, *Biophys. J. 91*, 206-216.

43. Mani, R., Cady, S. D., Tang, M., Waring, A. J., Lehrer, R. I., and Hong, M. (2006) Membrane-dependent oligomeric structure and pore formation of a β-hairpin antimicrobial peptide in lipid bilayers from solid-state NMR, *Proc. Natl. Acad. Sci. U.S.A. 103*, 16242-16247.

44. Mani, R., Tang, M., Wu, X., Buffy, J. J., Waring, A. J., Sherman, M. A., and Hong, M. (2006) Membrane-bound dimer structure of a β-hairpin antimicrobial peptide from rotational-echo double-resonance solid-state NMR, *Biochemistry 45*, 8341-8349.

45. Afonin, S., Grage, S. L., Ieronimo, M., Wadhwani, P., and Ulrich, A. S. (2008) Temperature-dependent transmembrane insertion of the amphiphilic peptide PGLa in lipid bilayers observed by solid state ^{19}F NMR spectroscopy, *J. Am. Chem. Soc. 130*, 16512-16514.

46. Buffy, J. J., Waring, A. J., and Hong, M. (2005) Determination of peptide oligomerization in lipid bilayers using ^{19}F spin diffusion NMR, *J. Am. Chem. Soc. 127*, 4477-4483.

47. Ieronimo, M., Afonin, S., Koch, K., Berditsch, M., Wadhwani, P., and Ulrich, A. S. (2010) ^{19}F NMR analysis of the antimicrobial peptide PGLa bound to native cell membranes from bacterial protoplasts and human erythrocytes, *J. Am. Chem. Soc. 132*, 8822-8824.

48. Gottler, L. M., de la Salud Bea, R., Shelburne, C. E., Ramamoorthy, A., and Marsh, E. N. G. (2008) Using fluorous amino acids to probe the effects of changing hydrophobicity on the physical and biological properties of the beta-hairpin antimicrobial peptide protegrin-1, *Biochemistry 47*, 9243-9250.

49.   Gottler, L. M., Lee, H. Y., Shelburne, C. E., Ramamoorthy, A., and Marsh, E. N. G. (2008) Using fluorous amino acids to modulate the biological activity of an antimicrobial peptide, *ChemBioChem 9*, 370-373.

50.   Wang, P., Tang, Y., and Tirrell, D. A. (2003) Incorporation of trifluoroisoleucine into proteins in vivo, *J. Am. Chem. Soc. 125*, 6900-6906.

51.   Meng, H., and Kumar, K. (2007) Antimicrobial activity and protease stability of peptides containing fluorinated amino acids, *J. Am. Chem. Soc. 129*, 15615-15622.

52.   Chiti, F., and Dobson, C. M. (2006) Protein misfolding, functional amyloid, and human disease, *Annu. Rev. Biochem. 75*, 333-366.

53.   Dobson, C. M. (2003) Protein folding and misfolding, *Nature 426*, 884-890.

54.   DeToma, A. S., Salamekh, S., Ramamoorthy, A., and Lim, M. H. (2012) Misfolded proteins in Alzheimer's disease and type II diabetes, *Chem. Soc. Rev. 41*, 608-621.

55.   Sunde, M., and Blake, C. (1997) The structure of amyloid fibrils by electron microscopy and X-ray diffraction, *Advances in Protein Chemistry, 50*, 123-159.

56.   Luca, S., Yau, W. M., Leapman, R., and Tycko, R. (2007) Peptide conformation and supramolecular organization in amylin fibrils: constraints from solid-state NMR, *Biochemistry 46*, 13505-13522.

57.   Nelson, R., and Eisenberg, D. (2006) Recent atomic models of amyloid fibril structure, *Curr. Opin. Struct. Biol. 16*, 260-265.

58.   Tycko, R. (2011) Solid-state NMR studies of amyloid fibril structure, *Annu. Rev. Phys. Chem. 62*, 279-299.

59.   Fandrich, M. (2007) On the structural definition of amyloid fibrils and other polypeptide aggregates, *Cell. Mol. Life Sci. 64*, 2066-2078.

60.   Fandrich, M., Meinhardt, J., and Grigorieff, N. (2009) Structural polymorphism of Alzheimer A beta and other amyloid fibrils, *Prion 3*, 89-93.

61.   Butterfield, S. M., and Lashuel, H. A. (2010) Amyloidogenic Protein Membrane Interactions: Mechanistic Insight from Model Systems, *Angew. Chem. Int. Ed. 49*, 5628-5654.

62.   Wilson, M. R., Yerbury, J. J., and Poon, S. (2008) Potential roles of abundant extracellular chaperones in the control of amyloid formation and toxicity, *Mol. BioSyst. 4*, 42-52.

63.   Ferreira, S. T., Vieira, M. N., and De Felice, F. G. (2007) Soluble protein oligomers as emerging toxins in Alzheimer's and other amyloid diseases, *IUBMB Life 59*, 332-345.

64.   Haataja, L., Gurlo, T., Huang, C. J., and Butler, P. C. (2008) Islet amyloid in type 2 diabetes, and the toxic oligomer hypothesis, *Endocr. Rev. 29*, 303-316.

Chapter 2

Using ^{19}F NMR to Probe Changes in Structure and Dynamics of Membrane-Active

Peptides Interacting with Lipid Bilayers

2.1. Introduction

The work described in this chapter has been published as: "Using Fluorine NMR to Probe Changes in Structure and Dynamics of Membrane-Active Peptides Interacting with Lipid Bilayers." Yuta Suzuki, Benjamin C. Buer, Hashim M. Al-Hashimi, and E. Neil G. Marsh (2011) Biochemistry, 50 (27): 5979 – 5987 (1). The co-authors were very helpful in conducting this research and analyzing the results. Dr. Buer assisted me with NMR and MIC experiments and provided two peptides, MSI-F6 and MSI-F7, for this study. Numerous suggestions and guidance on NMR came from Prof. Hashimi AI-Hashimi. I also would like to acknowledge Dr. Jeetender Chugh for helpful discussions and advice on CPMG experiments.

The interaction of small peptides with the lipid bilayer of the cell membrane is important in a variety of biological processes (2-7). These membrane-active peptides may have protective properties such as AMPs, anti-cancer and anti-viral peptides, or be involved in pathological processes such as cell-penetrating peptides, viral fusion peptides and venom peptides. For all

these classes of peptides, interactions between the membrane lipid bilayer and the peptide are central to their biological functions.

Characterizing peptide-membrane interactions is often challenging because of the transient and dynamic nature of these interactions. The peptide may adopt different orientations with respect to the lipid bilayer and different oligomerization states that are concentration-dependent. Solid-state NMR experiments have used various NMR-active nuclei to investigate the structures and orientations of AMPs bound to lipid membranes (8-13). These include studies using fluorine-labeled AMPs to provide information on peptide orientation in membranes. However, these experiments require peptide concentrations that are orders of magnitude higher than their physiologically active range, so it is not always clear whether such structures represent biologically active species. Solution-phase ^{19}F NMR has proved an informative tool for investigating biological interactions; for example in probing the dynamics of soluble proteins (14-16) and the immersion depth of lipophilic molecules in lipid bilayers (17, 18).

AMPs are a diverse family of membrane-active peptides found in essentially all multi-cellular organisms. Although some AMPs have specific intracellular targets (2), most exert their antimicrobial activity by binding directly to the microbial membrane and compromising its integrity (Figure 1.7) (19-21). Almost all AMPs are highly amphipathic, with one face of the peptide being hydrophobic and the other face presenting a cluster of positively charged residues (22-24). The selectivity of AMPs for bacterial membranes arises primarily from electrostatic interactions between the positively charged peptide and the negatively charged phospholipids that predominate in bacterial cell membranes. Eukaryotic membranes, which contain predominantly neutral phospholipids, are usually less susceptible to disruption by AMPs; the presence of cholesterol in eukaryotic membranes also helps prevent membrane disruption by

AMPs (25). Upon association with the membrane, disruption of the bacterial membrane may proceed through a number of mechanisms, including the formation of pores, membrane thinning and detergent-like action (21, 26, 27).
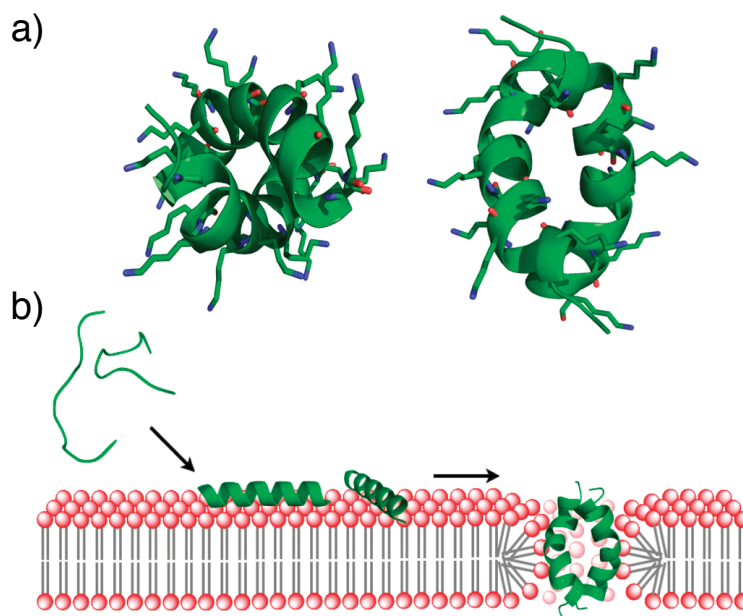
Figure 2.1. The proposed structure and mechanism of MSI-78 on lipid membranes (a) Two views of the structure of MSI-78, determined from NMR experiments (29), with peripheral Lys residues shown as sticks. (b) Cartoon illustrating the mechanism for insertion of MSI-78 into a lipid bilayer to form toroidal pores.

My studies have focused on the potent, synthetic AMP, MSI-78 (pexiganan), which provides a convenient model system to investigate peptide-membrane interactions. MSI-78 is thought to disrupt bacterial membranes by forming toroidal pores in the lipid bilayer (28), as illustrated in Figure 2.1. Based on a combination of solution and solid-state NMR experiments the peptide has been shown to adopt a dimeric α-helical coiled-coil structure (Figure 2.1) in the presence of liposomes (29). The dimer interface is formed by contacts between hydrophobic residues, and the positively charged lysine (Lys) residues that face the exterior of the structure

interact with hydrophilic lipid head groups. Using a series of MSI-78 peptides that incorporate tfeGly **6** (Figure 1.2), a small and sensitive NMR probe, the local structure and dynamics of the peptide changes on binding the lipid bilayer were investigated. In previous studies in our laboratory (30), the binding of two fluorinated MSI-78 variants incorporating tfeGly at a positively charged exterior position (Lys-7) or a hydrophobic position (leucine (Leu)-6) to small unilamellar vesicles and bicelles was detected by following changes in the ^{19}F chemical shift and measuring the dynamics of peptide the transverse relaxation rate (R_2) of the ^{19}F nucleus using The Carr-Purcell-Meiboom-Gill (CPMG) relaxation dispersion experiments. Whereas these initial studies provided a "proof of concept", we considered it important to conduct a more comprehensive study to determine, more generally, how sensitive fluorine probes are for distinguishing chemical environment and local dynamics.

In this chapter, I have extended our investigation by synthesizing a series of MSI-78 variants in which tfeGly has been introduced at strategic positions throughout the 22-residue peptide. These peptides are named as MSI-F*n*, when *n* refers to the position in the peptide that has been substituted with tfeGly. Guided by the NMR structure of the peptide bound to lipids (29), I introduced tfeGly at four hydrophobic positions and at four Lys residues spaced along the length of the peptide, including the C-terminal residue Lys-22; I also substituted the N-terminal glycine (Gly), which may be expected to show a large change in mobility. The positions that were substituted are shown in Figure 2.2. For each peptide, I have measured the changes in ^{19}F chemical shifts, longitudinal and transverse relaxation rates (R_1 and R_2, respectively), and D$_2$O-induced ^{19}F chemical shifts that occur upon peptide binding to lipid bicelles. This has allowed a detailed picture to be obtained of the local changes in chemical environment peptide dynamics that occur when MSI-78 binds to the lipid bilayer.
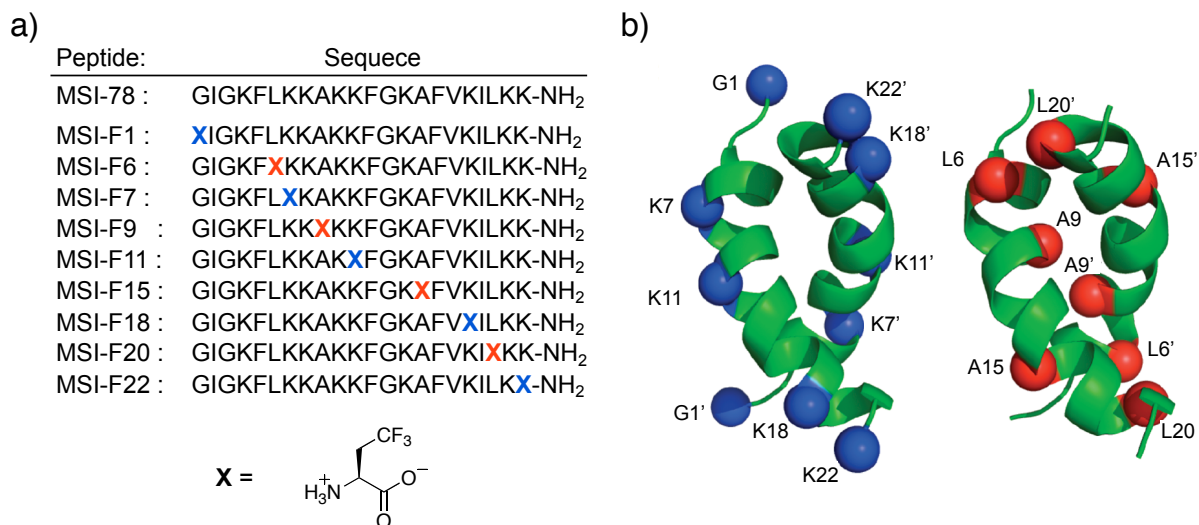
Figure 2.2. Substituted positions of tfeGly in MSI-78 (a) The primary sequence of MSI-78 and the sequences of tFeGly-substituted peptides used in this study. (b) The positions of amino acid substitutions are mapped on to the structure MSI-78 dimer formed in DPC micelles (32). Substitutions at hydrophilic positions (blue balls) are shown on the structure to the left; substitutions at hydrophobic positions (red balls) are shown on the structure to the right. Structures are rotated ~ 180° with respect to each other.

2.2. Experimental Procedures

2.2.1. Peptide Preparation

Racemic tfeGly was purchased from SynQuest Labs and acetylated to enzymatically resolved (porcine kidney acylase I) resulting in L-4,4,4-trifluoroethylglycine (tfeGly) having >99% enantiomeric excess (31, 32). The pure amino acid was converted to its Boc- or Fmoc-derivative by standard procedures. The sequences of MSI-78 derivatives are shown in Figure 2.2. Peptides were synthesized manually by either standard Boc procedure on MBHA resin or by Fmoc procedure on PAL-PEG resin, as described previously (32-34). Peptides were purified by reverse phase high-performance liquid chromatography (HPLC) using a gradient of water/acetonitrile with 0.1% trifluoroacetic acid (TFA); excess residual TFA was removed by a Stratosphere SPE column (Varian). Stock peptide concentrations were determined using [19]F

NMR with a known concentration of TFA as an internal reference. Peptide identities were confirmed using Matrix-assisted Laser Desorption/Ionization Mass Spectrometry (MALDI-MS).

2.2.2. Lipid Preparation

1,2-dimyristoyl-sn-glycero-3-phosphocholine (DMPC), 1,2-dimyristoyl-sn-glycero-3-phospho-(1'-rac-glycerol) (DMPG) and 1,2-dihexanoyl-sn-glycero-3-phosphocholine (DHPC) were purchased from Avanti Polar Lipids. Dodecylphosphocholine (DPC) was purchased from Affymetrix. Isotropic bicelles were made in PBS buffer, pH 7.4 with 10% D_2O by adding a solution of 3:1 DMPC/DMPG to a solution of DHPC giving q=0.5 resulting in a clear, non-viscous solution.

2.2.3. Circular Dichroism

CD spectra of peptides were collected with an Aviv 62DS spectropolarimeter using a 0.2 cm pathlength cell. CD measurements were performed at peptide concentration of $80 - 200$ μM in 75 mM sodium chloride and 25mM sodium phosphate (pH 7.4) in the presence or absence of 100 μM SDS micelles at 30 °C. Mean residue ellipticities, [θ], were calculated using [θ] = $\theta_{obsd}/10lcn$ where θ_{obsd} is the ellipticity measured in millidegrees, c is the molar concentration, l is the cell path length in centimeters, and n is the number of residues in the peptide. All the peptides exhibited CD spectra characteristic of unstructured peptides in plain buffer, which converted to spectra characteristic of extensively helical peptides upon addition of 100 mM sodium dodecyl sulfate (SDS), as shown in the plots in Figure 2.3.

2.2.4. MIC Determinations

The peptide minimum inhibitory concentrations (MICs) against *E. coli* K12 were determined by the microdilution antimicrobial assay procedure, using 96-well plates in replicates of four, as described previously (35).

2.2.5. Proton NMR spectroscopy

Samples were prepared in PBS, pH 6.0, containing 10% D_2O, 100 mM DPC and 400 μM peptide. A water suppression pulse sequence (WET) was employed in the acquisition of NMR spectra (Figure 2.4).

2.2.6. ^{19}F NMR spectroscopy

All ^{19}F NMR experiments were performed at 30 °C using a Varian Inova 500 MHz NMR spectrometer equipped with a double-tuned [1]H-^{19}F room-temperature probehead. Peptide and lipid samples were prepared with 10% D_2O in PBS, pH 7.4. All experiments were performed at a constant peptide concentration of 400 mM unless indicated otherwise and referenced to TFA at 0 ppm. To measure solvent isotope-induced changes in chemical shift, peptide and lipid samples were first prepared with 10% D_2O in PBS, pH 7.4. The samples were then lyophilized overnight and re-dissolved in either 90% D_2O. The solvent-induced changes were referenced to TFA at 0 ppm as an external standard in PBS, pH 7.4, 10% D_2O.

[19]F CPMG relaxation dispersion experiments were performed for the peptides in the free state and in the presence of lipid bicelles (200 mM total lipid concentration, q=0.5, long chain lipids 3:1 mol/mol DMPC/DMPG and short chain lipid being DHPC). CPMG delays (τ_{cp}) were varied from 0.5 to 10.0 ms with each data point recorded as a series of standard 1-D transverse

relaxation rate measurements with T_2 delays of 0.05, 0.1, 0.2, 0.4, 0.8 and 1.6 ms for free peptide and 0.0125, 0.025, 0.05, 0.1, 0.2 and 0.4 ms for bicelle-bound peptide. The pulse width was 7.9 ms. Data sets were recorded with acquisition time of 1 s in T_1 along with a 10 s pre-scan delay. 16 scans, net acquisition time of 17 min/data point, were required to achieve adequate signal-to-noise ratios for peptides in the free state; 32 scans, net acquisition time of 35 min/data point, were required to achieve adequate signal-to-noise ratios for peptides bound to bicelles. [19]F spin-lattice relaxation times (T_1) were acquired by an inversion recovery sequence ($180° – \tau - 90°$) using a total of six τ values of 0.0625, 0.125, 0.25, 0.5, 1.0, 2.0 s. Data were processed and analyzed using VNMRJ software and plotted using the Kaleidagraph software package. All other experimental details have been described previously (30, 36).

2.3. Results and Discussion

2.3.1. Effects of tfeGly Substitution on Secondary Structure and Biological Activity

The feasibility of using fluorine-labeled amino acids to probe the chemical environment and dynamics of membrane-bound peptides containing tfeGly was demonstrated previously in our laboratory (30). tfeGly provides a useful probe, as it is relatively small (approximately comparable to valine), is commercially available, and is readily incorporated into peptides. The C-3 methylene group affords one degree of rotational motion to the trifluoromethyl group, but on the time scale of our experiments, backbone dynamics are likely to dominate its NMR behavior. Although substitution of hydrophilic residues, such as Lys, with tfeGly obviously cannot be considered as conservative, numerous experiments with AMPs have shown that their biological properties and structure depend primarily on their overall physicochemical properties and are not highly dependent on sequence.

Substitution of tfeGly at different positions in these peptides does not appear to cause any gross structural changes or changes in biological activity. The peptides all appear to adopt a predominantly random coil structure in plain buffer (Figure 2.3a), and exhibit extensively helical CD spectra in the presence of SDS micelles (Figure 2.3b). The mean residue ellipticities, θ_{222}, of the peptides varied by less than 10% (20200 cm^2 dmol^{-1} residue^{-1} > θ_{222} > 21900 cm^2 dmol^{-1} residue^{-1}) between the different peptides and are similar to that of MSI-78 (θ_{222} = 20700 cm^2 dmol^{-1} residue^{-1}). The MIC values for all the peptides were within the range of 3 – 6 µg/mL against *E. coli* K12 strains; any differences in MICs between the parent MSI-78 peptide (37) and the tfeGly-labeled peptides were not statistically significant (Figure 2.3c).

a)   b)   c)

Peptide	MIC (µg/mL)
MSI-78	3.125
MSI-F1	< 3.125
MSI-F6	3.125
MSI-F7	3.125
MSI-F9	3.125
MSI-F11	< 3.125
MSI-F15	3.125
MSI-F18	6.250
MSI-F20	3.125
MSI-F22	3.125
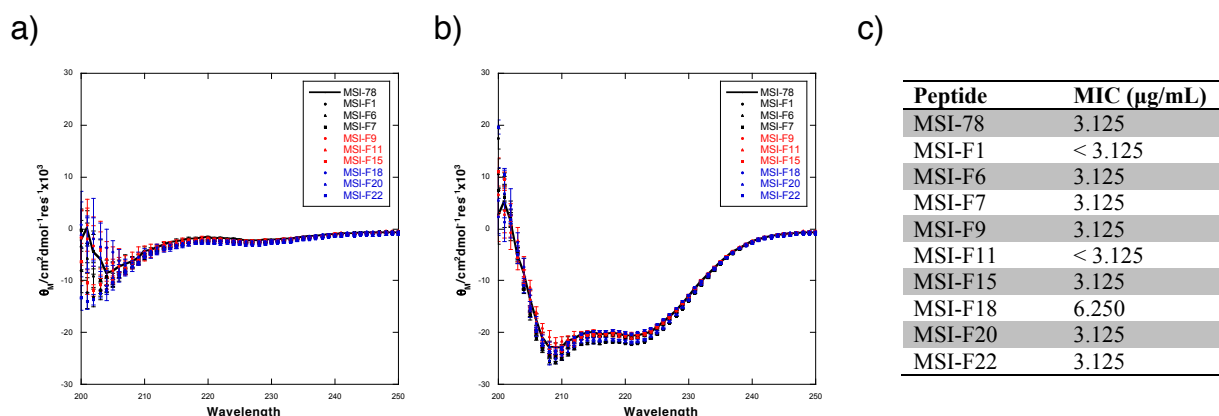
Figure 2.3. Effects of tfeGly substitution on secondary structure and biological activity (a) CD spectra of MSI peptides in plain buffer (b) CD spectra of MSI peptides in buffer containing 100 mM SDS micelles (c) MICs against *E. coli* K12 for MSI peptides.

As a further check on the structural integrity of the tfeGly-labeled peptides, one-dimensional proton NMR spectra of the peptides were recorded for the peptides bound to DPC micelles (Figure 2.4). In each case, the peptides exhibited well-dispersed resonances in the amide

region, characteristic of structured peptides. As expected, small changes between the spectra of each tfeGly-labeled peptide and MSI-78 were observed, which may reflect small local structural changes and/or slight differences in sample preparation. The resonances from the three Phe side chains in the peptide could clearly be distinguished and were very similar in each case, indicating that the hydrophobic core of the dimeric peptide bundle remains intact. Resonances from the aliphatic side chains were obscured by signals from DPC micelles.
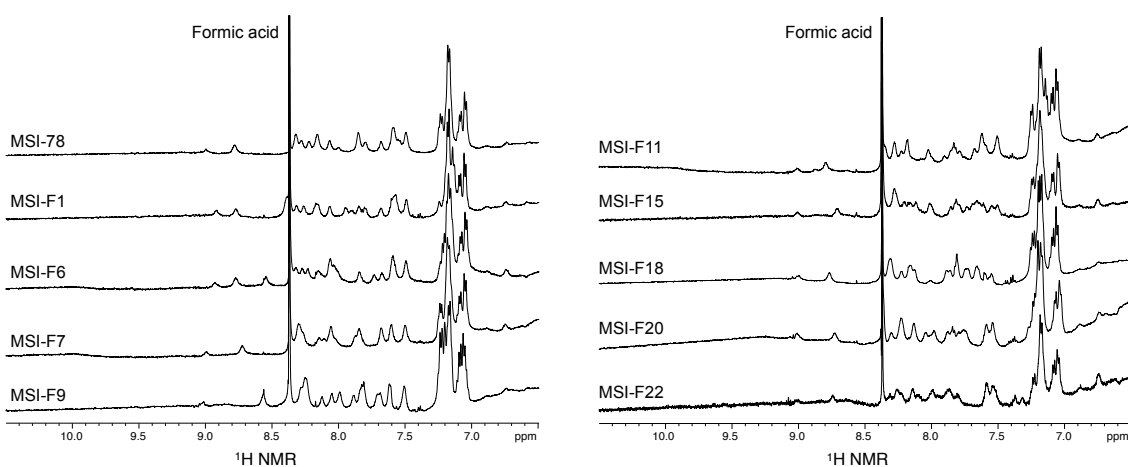
Figure 2.4. Proton NMR spectra of MSI peptides bound to DPC micelles.

2.3.2. Sensitivity of [19]F Chemical Shifts to the Position of Fluorination

In the absence of lipids, all the peptides, except MSI-F1, exhibited a sharp triplet in the ^{19}F NMR spectrum between 11.40 and 11.73 ppm relative to TFA (Figure 2.5 and Table 2.1). The resonance for MSI-F1, in which Gly is substituted with tfeGly, is shifted significantly downfield at 12.15 ppm. This is likely due to the influence of the positively charged amino group at the N-terminus (Table 2.1).
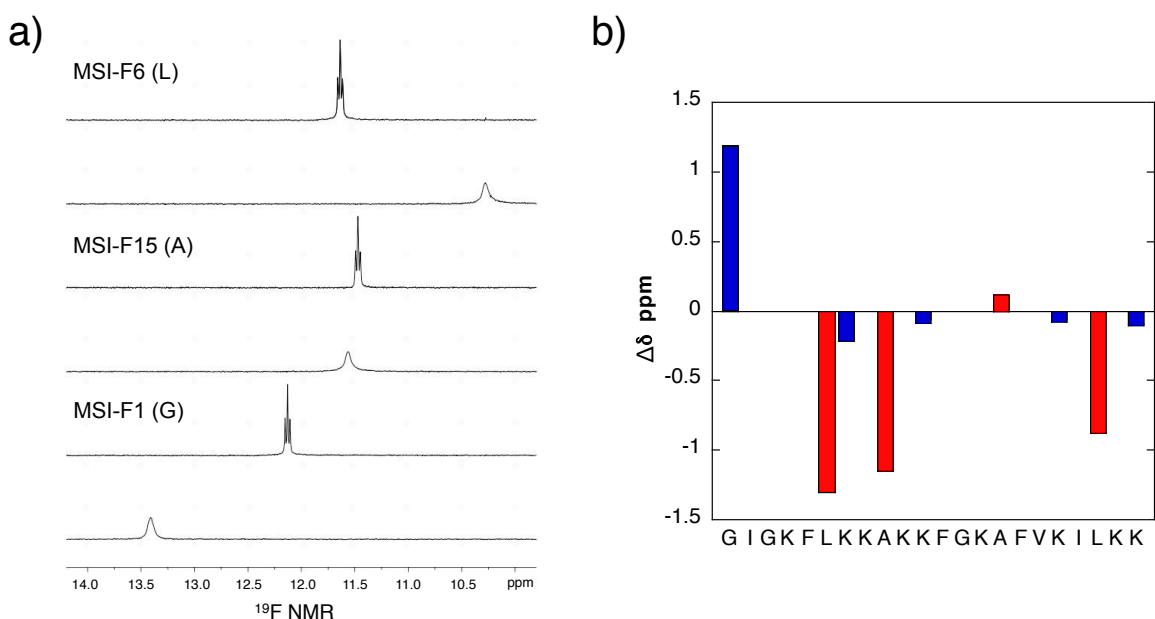
Figure 2.5. Sensitivity of ^{19}F chemical shifts to the position of fluorination (a) Representative ^{19}F NMR spectra illustrating changes in chemical shift and peak width that occur when tfeGly-substituted peptides bind to lipid bicelles. The upper trace in pair of spectra is for the free peptide and the lower trace for the peptide bound to bicelles. Spectra were recorded at 30 °C at pH 7.4 in PBS buffer with 10% D$_2$O and referenced to TFA. (b) Chemical shift changes, Δδ, associated with peptide binding to bicelles plotted as a function of label position. Hydrophilic and hydrophobic residues are colored blue and red, respectively.

I then examined the binding of the fluorinated MSI-78 variants to lipid bicelles, which are commonly used as a model membrane system. As described previously (30), for these studies bicelles are preferable to small unilamellar vesicles (SUVs), which are also commonly used to study AMP-membrane interactions. Bicelles are more stable than SUVs and present a flat, rather than highly curved, surface for peptide binding. All the peptides exhibited distinct changes in their ^{19}F chemical shifts upon binding to bicelles, which appeared as broadened single peaks (Figure 2.5).

The change in chemical shift was highly dependent on the position of the tfeGly residue (Table 2.1), demonstrating the sensitivity of the ^{19}F nucleus to the local chemical environment.

The positions that exhibited the largest upfield shifts, ranging from 0.9 to 1.3 ppm, are those at hydrophobic positions that are deeply buried in the core of the coiled coil (Figure 2.6). The Lys positions, which project out from the coiled coil and interact with the lipid head groups, exhibited smaller upfield shifts ranging from 0.06 to 0.26 ppm (Figure 2.5). Two positions seem to deviate from this general trend. Substituting tfeGly at the N-terminal Gly position (MSI-F1) results in a large downfield shift of 1.2 ppm; MSI-F15, in which alanine (Ala) is substituted by tfeGly, also showed a downfield shift, although this was quite small, only 0.09 ppm.

Peptide	Amino acid substituted	[a]δ_{free} (ppm)	[a]δ_{bound} (ppm)	R_{1free} (Hz)	R_{1bound} (Hz)	[b]R_{2free} (Hz)	[b]R_{2bound} (Hz)
MSI-F1	Gly	12.13	13.41	1.40 ± 0.05	2.55 ± 0.06	1.7 ± 0.1	27 ± 1
MSI-F6	Leu	11.64	10.29	2.18 ± 0.05	3.09 ± 0.04	3.7 ± 0.2	58 ± 9
MSI-F7	Lys	11.65	11.38	2.31 ± 0.03	3.10 ± 0.14	3.7 ± 0.2	22 ± 2
MSI-F9	Ala	11.73	10.57	2.37 ± 0.05	3.10 ± 0.14	4.1 ± 0.2	43 ± 3
MSI-F11	Lys	11.55	11.49	2.30 ± 0.04	3.06 ± 0.05	4.1 ± 0.2	27 ± 3
MSI-F15	Ala	11.47	11.56	2.26 ± 0.05	3.86 ± 0.11	3.9 ± 0.1	49 ± 3
MSI-F18	Lys	11.52	11.46	2.23 ± 0.05	3.24 ± 0.07	3.1 ± 0.1	29 ± 2
MSI-F20	Leu	11.60	10.69	2.05 ± 0.03	3.12 ± 0.09	2.8 ± 0.2	36 ± 2
MSI-F22	Lys	11.40	11.25	1.53 ± 0.06	2.27 ± 0.05	2.1 ± 0.2	20 ± 0.4
tfeGly		11.62		0.54 ± 0.03		1.1 ± 0.1	

Table 2.1. [19]F Chemical shifts, R_1 and R_2 values for MSI-F peptides. [a] chemical shift relative to TFA
[b] value at $1/\tau_{cp}$ = 2000 Hz

Although ^{19}F chemical shifts are influenced by various factors (38), the "anomalous" chemical shift of MSI-F15 might be explained by the fact that the tfeGly side chain is expected to protrude toward the charged face of the α-helix (Figure 2.6). Its chemical shift is likely to be influenced by the positively charged Lys residues that are adjacent to it; this could result in deshielding of the nucleus and thereby shift the resonance to lower field. In contrast, substitution of Ala-9 with tfeGly (MSI-F9) places the side chain pointing into the hydrophobic core (Figure

2.6), presumably resulting in a more shielded environment. The downfield shift observed when tfeGly is at the N-terminal position is harder to explain. Possibly, in its folded state, the N-terminus of the peptide is less well solvated so that the deshielding effect of the positively charged amino terminus is greater. The N-terminus is also in the proximity of the amino group of the C-terminal Lys of the peptide forming the opposite strand of the coiled coil, which could also influence the fluorine chemical shift.
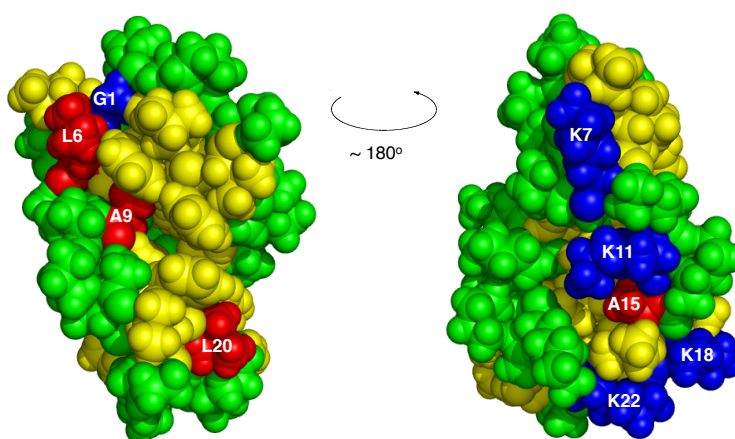
Figure 2.6. Space filling models of the MSI-78 dimer illustrating the chemical environment of the positions substituted by tfeGly. Residues substituted by tfeGly are colored blue (hydrophilic) and red (hydrophobic). Other hydrophobic and hydrophilic residues are colored yellow and green respectively. For clarity, the substituted positions are only shown on one peptide of the dimer. The two structures are related to each other by a ~ 180° rotation about the vertical axis.

Changes in ^{19}F chemical shift provide a simple way of detecting binding at concentrations that are close to those at which the peptide is biologically active. For MSI-78, spectral shifts were apparent for all the tfeGly-labeled peptides, regardless of the position of the label. In these studies, spectra were recorded on a 500 MHz spectrometer at a peptide concentration of 400 μM to facilitate CPMG experiments; however, 40 μM tfeGly-labeled peptide is readily detected at a signal-to-noise ratio of 4:1 after 64 scans in a spectrum that takes

only 2 min to acquire. Another advantage is that the wide range of chemical shift changes observed potentially allows multiple peptides to be studied in one experiment (or multiple fluorine probes to be introduced into one peptide), so that more complex multicomponent interactions can be studied.

2.3.3. Changes in Solvent Exposure upon Binding to Lipid Bicelles

The ^{19}F chemical shift is sensitive to the isotopic composition of the solvent, e.g., whether H_2O or D_2O (14, 16), and this provides a means to investigate changes in solvent exposure that may occur when MSI-78 binds to lipid bilayers. In the absence of bicelles, changing the solvent composition from 10% D_2O to 90% D_2O results in the ^{19}F chemical shift for each of the peptides moving fairly uniformly upfield by 0.08 to 0.11 ppm (Figure 2.7). In the presence of bicelles, the chemical shift changes, $\Delta\delta_{(H_2O - D_2O)}$, $(\Delta\delta_{(H_2O - D_2O)} = \delta_{H_2O} - \delta_{D_2O})$, are more variable and range from 0.01 to 0.08 ppm (changes of ≤ 0.01 ppm were not considered significant).

In theory, positions that are deeply buried should exhibit no changes in chemical shift with a change in the solvent, whereas positions that are completely exposed should exhibit changes similar to those observed for the unbound peptides. Inspection of the data reveals this to be qualitatively true: positions 7, 11, 18, and 22, which are occupied by Lys in MSI-78, exhibit the largest chemical shift changes ($\Delta\delta = 0.08 - 0.06$ ppm). These are somewhat smaller than those observed for the free peptide, indicating that interactions with the lipid head groups may reduce the level of solvent exposure. In contrast, at positions 6, 9, 15, and 20, which are occupied by hydrophobic residues in MSI-78, $\Delta\delta_{(H_2O - D_2O)}$ is very small, -0.01 to 0.03 ppm. This indicates a very low degree of solvent exposure in the bound state and provides support for the proposed

38

structural model of MSI-78 in which these positions form part of the hydrophobic core of the coiled coil peptide dimer in the membrane.
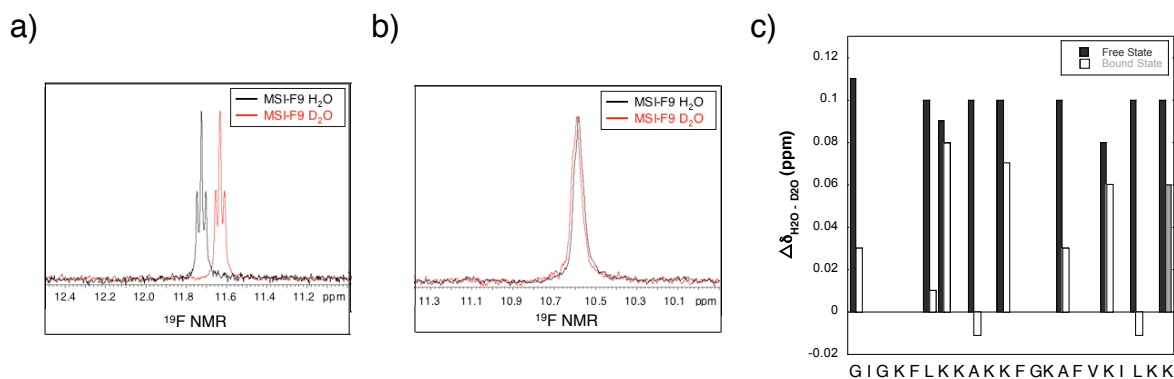
Figure 2.7. Changes in solvent exposure upon binding to lipid bicelles determined by solvent isotope effect (a, b) Representative ^{19}F NMR spectra (MSI-F9) illustrating changes in chemical shift that occur in solvent isotope effect (H_2O/D_2O). Peptide is in 10% (v/v) D_2O (red) and 90% D_2O (black) in free solution (a) and in bicelles (b). (c) Solvent isotope effects on ^{19}F chemicals shift ($\Delta\delta_{(H_2O - D_2O)}$) plotted as a function of label position. Black bars: peptides in free solution; white bars: peptides bound to lipid bicelles.

Effects of solvent isotopes (H_2O vs D_2O) on the fluorine chemical shift demonstrate that this technique also provides a simple but effective probe of peptide-membrane interactions (14, 16). In this case, it is evident that, even when embedded in the membrane, the Lys positions remain predominantly solvated whereas the hydrophobic positions are extensively shielded from the solvent. This supports the model in which MSI-78 forms toroidal pores in the lipid bilayer (28), in which the Lys side chains interact with hydrophilic lipid headgroups.

2.3.4. Changes in Peptide Dynamics Probed by ^{19}F Longitudinal and Transverse Relaxation Rates

Various studies of fluorinated proteins have shown that ^{19}F longitudinal relaxation rates ($R_1 = 1/T_1$) are generally faster for buried residues in proteins than for solvent-exposed residues

(14, 16), and these measurements have been used to probe protein structure and folding. Therefore, I also investigated how R_1 changed when the peptides bound to bicelles. The R_1 values for the free peptides range from 1.4 to 2.4 Hz, with the terminal residues exhibiting the lowest R_1 values (Table 2.1). The R_1 values increase fairly uniformly for the peptides on binding bicelles with R_1 values ranging from 2.3 to 3.9 Hz (Table 2.1). It appears that longitudinal relaxation measurements are not especially sensitive to differences in the local chemical environment for this particular system.

The transverse relaxation rates of the free peptides (R_{2f}) were measured using a CPMG experiment in which $1/\tau_{cp}$ was varied from 100 to 2000 Hz. For all the peptides, R_2 values are similar and are independent of τ_{cp} (Figure 2.8a), as expected for an unstructured peptide in free solution. The experimental R_2 values (Figure 2.8b) generally agree well with that calculated for a random coil peptide in free solution (30); however, residues at the N- and C-termini exhibit significantly slower R_{2f} values (Figure 2.8b and Table 2.1). This indicates that the ends of the peptide are more mobile than the center, which would be expected for an unstructured peptide chain.

The transverse relaxation rates were measured for each peptide bound to bicelles, R_{2b}, using the same set of CPMG pulse sequences. Under the conditions used in the experiment, nearly all of the peptide was bound to the lipid bilayer (as shown in Figure 2.5, no signal for the free peptide could be detected). As discussed previously (30, 39, 40), when τ_{cp} is short relative to the residence time, τ_b, of the peptide in the lipid, the observed R_{2b} values reflect the intrinsic relaxation rates of the ^{19}F nuclei unencumbered by chemical exchange. Under these conditions, differences in R_{2b} may be attributed to changes in the local dynamics of the peptide.
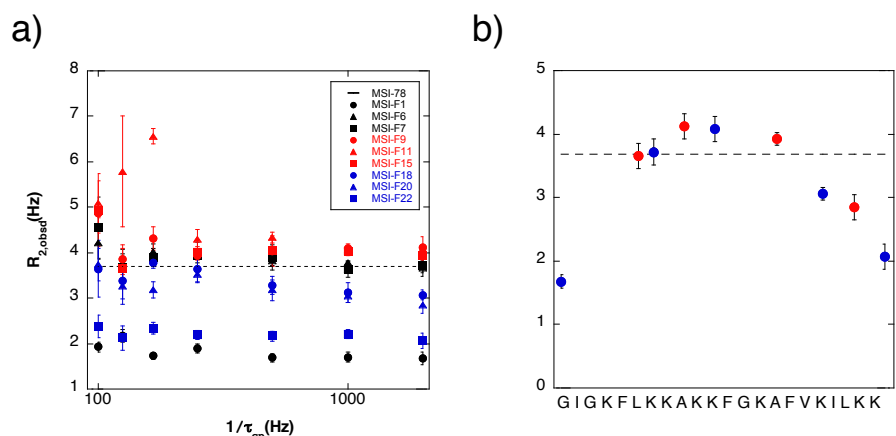
Figure 2.8. Observed transverse relaxation rates, $R_{2,observed}$, for MSI-F peptides in free solution (a) plotted as a function of CPMG pulsing rate ($1/\tau_{cp}$). Symbols used are MSI-F1 (●); MSI-F6 (▲); MSI-F7 (■); MSI-F9 (●); MSI-F11 (▲); MSI-F15 (■); MSI-F18 (●); MSI-F20 (▲); MSI-F22 (■). (b) plotted as a function of sequence. The data were obtained using $1/\tau_{cp} = 2000$ Hz so that the chemical exchange component is removed. The calculated $R_2 = 3.7$ Hz for free peptide is indicated by the dashed line. Hydrophilic and hydrophobic residues are colored blue and red, respectively.

The observed R_{2b} values for all the peptides were essentially invariant for values of $1/\tau_{cp}$ greater than 250 Hz, consistent with our previous results (30). At longer pulse intervals, R_{2b} appears to increase, indicative of chemical exchange (Figure 2.9a). However, at these time scales, the experiment approaches the limits of sensitivity because of interconversion between in-phase and antiphase magnetization during the spin echo period, as well as loss of signal intensity due to chemical exchange. Therefore, measurements are accompanied by large uncertainty in the value of R_{2b}, and τ_b cannot be reliably determined from the data. However, the experiment does allow us to put an upper limit on the rate at which the peptide dissociates from the membrane ($1/\tau_b$) of ~200 s^{-1}, consistent with our previous data (30).
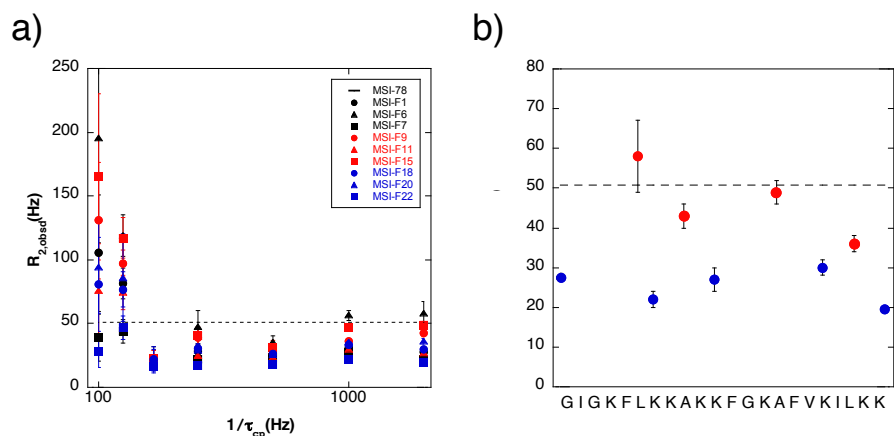
Figure 2.9. Observed transverse relaxation rates, $R_{2,observed}$, for MSI-F peptides bound to lipid bicelles (a) plotted as a function of CPMG pulsing rate ($1/\tau_{cp}$). Symbols used are MSI-F1 (●); MSI-F6 (▲); MSI-F7 (■); MSI-F9 (●); MSI-F11 (▲); MSI-F15 (■); MSI-F18 (●); MSI-F20 (▲); MSI-F22 (■). (b) plotted as a function of sequence. The data were obtained using $1/\tau_{cp}$ = 2000 Hz so that the chemical exchange component is removed. The calculated R_2 = 50.8 Hz for the peptide bound to lipid bicelles (assuming relaxation is only due tumbling of bicelles) is indicated by the dashed line. Hydrophilic and hydrophobic residues are colored blue and red, respectively.

The transverse relaxation rates measured for the CF_3 reporter group varied significantly depending upon the location of the reporter nuclei (Figure 2.9b). The R values for each of the peptides determined at a $1/\tau_{cp}$ of 2000 Hz are listed in Table 2.1. The hydrophobic positions exhibit the fastest relaxation rates (e.g., Leu-6, R_{2b} = 58 Hz; Ala-15, R_{2b} = 49 Hz), indicating that these residues, which are predicted to be in the hydrophobic core of the coiled coil, are relatively immobile. Moreover, the relaxation rates are close to the theoretical value, ~50 Hz, predicted if relaxation is dominated by the tumbling motion of the lipid bicelle. Hydrophilic positions, which are predicted to be on the surface of the coiled coil and interact with lipid headgroups, exhibit slower relaxation rates, indicating that these positions have greater mobility. The R_{2b} values do not vary greatly along the length of the peptide [e.g., Gly-1 (28 Hz), Lys-11 (27 Hz), and Lys-18 (29 Hz)], although the C-terminal Lys appears to be slightly more mobile. These data suggest

that the N-terminus is quite well structured when bound to the lipid and does not appear to undergo fraying on the time scale of these experiments. This is consistent with the significant degree of solvent protection observed for the N-terminus in the solvent isotope effect study. The C-terminus of the peptide is more dynamic, but compared to that of the free peptide, it is clearly less mobile and better structured.

The changes in chemical shifts and transverse relaxation rates observed when the peptides bind to bicelles appear to be independent of each other. Thus, although the positions occupied by Ala-9 and Ala-15 both appear to be quite immobile (R_{2b} = 43 and 49 Hz, respectively), Ala-9 shifts downfield by 1.15 ppm whereas Ala-15 shifts slightly upfield by 0.11 ppm. The chemical shifts of N- and C-terminal positions change in opposite directions (1.19 and 0.10 ppm, respectively) even though both positions exhibit similar mobilities as judged by their R_{2b} values (Figure 2.9).

From the measurements of transverse relaxation rates along the peptide backbone, I have obtained detailed information about the local dynamics of MSI-78 bound to the lipid bilayer. The hydrophobic positions of the amphipathic peptide that form the core of the coiled coil are the least dynamic positions. This suggests a well-packed core in which side chain rotations are restricted. The positively charged face of the coiled coil, which interacts with the hydrophilic lipid headgroups, is more dynamic, although far less so than in the unbound peptide. Moreover, positions toward the center of the peptide appear to be less dynamic than the ends of the peptide. This would be consistent with the peptides forming toroidal pores in the lipid bilayer, as has been deduced for MSI-78. If I assume the peptide sits centrally in the pore, the constriction of the peptide by the lipid bilayer would by greatest at the center of the pore, where the opening is narrowest.

The ^{19}F transverse relaxation data provide new and more detailed information about the local dynamics of peptide upon binding to a lipid membrane. The changes in ^{19}F chemical shifts can only be interpreted qualitatively using the structural model of MSI-78 determined by NMR (29). However, density functional theory methods have been used to calculate ^{19}F chemical shifts for a large number of fluorinated small molecules (41, 42) with a reasonable degree of accuracy. In a study particularly pertinent to these experiments, it was found that hindered rotation of CF_3 groups led to an upfield shift of the ^{19}F signal (42). Future advances in computational methods will likely allow ^{19}F chemical shifts in fluorinated peptides and proteins to be calculated. This would permit the relationship among structure, dynamics, and chemical shift to be quantitatively understood, providing a further tool for analyzing peptide-membrane interactions.

2.4. Conclusion

Studies in this chapter demonstrate that ^{19}F NMR provides a relatively sensitive and general technique for investigating the interactions of peptides and proteins with their membrane targets. Using a series of MSI-78 peptides that incorporate tfeGly, a small and sensitive NMR probe, I investigated how the local structure and dynamics of the peptide changes on binding the lipid bilayer. In particular, the chemical shift and transverse relaxation rates are highly sensitive to the position of the fluorine label in the peptide and provide information about changes in local peptide motions. Future work will aim toward using ^{19}F NMR to study peptide-membrane interactions *in vivo* at physiologically relevant concentrations.

2.5. References

1. Suzuki, Y., Buer, B. C., Al-Hashimi, H. M., and Marsh, E. N. G. (2011) Using Fluorine Nuclear Magnetic Resonance To Probe Changes in the Structure and Dynamics of Membrane-Active Peptides Interacting with Lipid Bilayers, *Biochemistry 50*, 5979-5987.

2. Brogden, K. A. (2005) Antimicrobial peptides: pore formers or metabolic inhibitors in bacteria?, *Nat. Rev. Microbiol. 3*, 238-250.

3. Dennison, S. R., Whittaker, M., Harris, F., and Phoenix, D. A. (2006) Anticancer alpha-helical peptides and structure/function relationships underpinning their interactions with tumour cell membranes, *Curr. Protein Pept. Sci. 7*, 487-499.

4. Dhople, V., Krukemeyer, A., and Ramamoorthy, A. (2006) The human β-defensin-3, an antibacterial peptide with multiple biological functions, *Biochim. Biophys. Acta. 1758*, 1499-1512.

5. Gennaro, R., and Zanetti, M. (2000) Structural features and biological activities of the cathelicidin-derived antimicrobial peptides, *Biopolymers 55*, 31-49.

6. Koyama, Y., Motobu, M., Hikosaka, K., Yamada, M., Nakamura, K., Saido-Sakanaka, H., Asaoka, A., Yamakawa, M., Sekikawa, K., Kitani, H., Shimura, K., Nakai, Y., and Hirota, Y. (2006) Protective effects of antimicrobial peptides derived from the beetle Allomyrina dichotoma defensin on endotoxic shock in mice, *Int. Immunopharmacol. 6*, 234-240.

7. Nomura, K., and Corzo, G. (2006) The effect of binding of spider-derived antimicrobial peptides, oxyopinins, on lipid membranes, *Biochim. Biophys. Acta. 1758*, 1475-1482.

8. Ramamoorthy, A., Thennarasu, S., Lee, D. K., Tan, A., and Maloy, L. (2006) Solid-state NMR investigation of the membrane-disrupting mechanism of antimicrobial peptides MSI-78 and MSI-594 derived from magainin 2 and melittin, *Biophys. J. 91*, 206-216.

9. Mani, R., Cady, S. D., Tang, M., Waring, A. J., Lehrer, R. I., and Hong, M. (2006) Membrane-dependent oligomeric structure and pore formation of a β-hairpin antimicrobial peptide in lipid bilayers from solid-state NMR, *Proc. Natl. Acad. Sci. U.S.A. 103*, 16242-16247.

10. Mani, R., Tang, M., Wu, X., Buffy, J. J., Waring, A. J., Sherman, M. A., and Hong, M. (2006) Membrane-bound dimer structure of a β-hairpin antimicrobial peptide from rotational-echo double-resonance solid-state NMR, *Biochemistry 45*, 8341-8349.

11. Afonin, S., Grage, S. L., Ieronimo, M., Wadhwani, P., and Ulrich, A. S. (2008) Temperature-dependent transmembrane insertion of the amphiphilic peptide PGLa in lipid bilayers observed by solid state ^{19}F NMR spectroscopy, *J. Am. Chem. Soc. 130*, 16512-16514.

12. Buffy, J. J., Waring, A. J., and Hong, M. (2005) Determination of peptide oligomerization in lipid bilayers using ^{19}F spin diffusion NMR, *J. Am. Chem. Soc. 127*, 4477-4483.

13. Ieronimo, M., Afonin, S., Koch, K., Berditsch, M., Wadhwani, P., and Ulrich, A. S. (2010) ^{19}F NMR analysis of the antimicrobial peptide PGLa bound to native cell membranes from bacterial protoplasts and human erythrocytes, *J. Am. Chem. Soc. 132*, 8822-8824.

14. Evanics, F., Bezsonova, I., Marsh, J., Kitevski, J. L., Forman-Kay, J. D., and Prosser, R. S. (2006) Tryptophan solvent exposure in folded and unfolded states of an SH3 domain by ^{19}F and ^{1}H NMR, *Biochemistry 45*, 14120-14128.

15. Hull, W. E., and Sykes, B. D. (1974) Fluorotyrosine alkaline phosphatase. ^{19}F nuclear magnetic resonance relaxation times and molecular motion of the individual fluorotyrosines, *Biochemistry 13*, 3431-3437.

16. Hull, W. E., and Sykes, B. D. (1976) Fluorine nuclear magnetic resonance study of fluorotyrosine alkaline phosphatase: the influence of zinc on protein structure and a conformational change induced by phosphate binding, *Biochemistry 15*, 1535-1546.

17. Kitevski-LeBlanc, J. L., Evanics, F., and Prosser, R. S. (2009) Approaches for the measurement of solvent exposure in proteins by ^{19}F NMR, *J. Biomol. NMR 45*, 255-264.

18. Prosser, R. S., Luchette, P. A., Westerman, P. W., Rozek, A., and Hancock, R. E. (2001) Determination of membrane immersion depth with O_2: a high-pressure ^{19}F NMR study, *Biophys. J. 80*, 1406-1416.

19. Huang, H. W., Chen, F. Y., and Lee, M. T. (2004) Molecular mechanism of Peptide-induced pores in membranes, *Phys. Rev. Lett. 92*, 198304.

20. Oren, Z., and Shai, Y. (1998) Mode of action of linear amphipathic α-helical antimicrobial peptides, *Biopolymers 47*, 451-463.

21. Wimley, W. C. (2010) Describing the mechanism of antimicrobial peptide action with the interfacial activity model, *ACS Chem. Biol. 5*, 905-917.

22. Hancock, R. E., and Lehrer, R. (1998) Cationic peptides: a new source of antibiotics, *Trends Biotechnol. 16*, 82-88.

23. Shai, Y. (1999) Mechanism of the binding, insertion and destabilization of phospholipid bilayer membranes by α-helical antimicrobial and cell non-selective membrane-lytic peptides, *Biochim. Biophys. Acta. 1462*, 55-70.

24. Wu, M., Maier, E., Benz, R., and Hancock, R. E. (1999) Mechanism of interaction of different classes of cationic antimicrobial peptides with planar bilayers and with the cytoplasmic membrane of *Escherichia coli*, *Biochemistry 38*, 7235-7242.

25. Epand, R. F., Ramamoorthy, A., and Epand, R. M. (2006) Membrane lipid composition and the interaction of pardaxin: the role of cholesterol, *Protein Pept. Lett. 13*, 1-5.

26. Oren, Z., and Shai, Y. (1997) Selective lysis of bacteria but not mammalian cells by diastereomers of melittin: structure-function study, *Biochemistry 36*, 1826-1835.

27. Selsted, M. E., Novotny, M. J., Morris, W. L., Tang, Y. Q., Smith, W., and Cullor, J. S. (1992) Indolicidin, a novel bactericidal tridecapeptide amide from neutrophils, *J. Biol. Chem. 267*, 4292-4295.

28. Hallock, K. J., Lee, D. K., and Ramamoorthy, A. (2003) MSI-78, an analogue of the magainin antimicrobial peptides, disrupts lipid bilayer structure via positive curvature strain, *Biophys. J. 84*, 3052-3060.

29. Porcelli, F., Buck-Koehntop, B. A., Thennarasu, S., Ramamoorthy, A., and Veglia, G. (2006) Structures of the dimeric and monomeric variants of magainin antimicrobial peptides (MSI-78 and MSI-594) in micelles and bilayers, determined by NMR spectroscopy, *Biochemistry 45*, 5793-5799.

30. Buer, B. C., Chugh, J., Al-Hashimi, H. M., and Marsh, E. N. G. (2010) Using fluorine nuclear magnetic resonance to probe the interaction of membrane-active peptides with the lipid bilayer, *Biochemistry 49*, 5760-5765.

31. Tsushima, T., Kawada, K., Ishihara, S., Uchida, N., Shiratori, O., Higaki, J., and Hirata, M. (1988) Fluorine-Containing Amino-Acids and Their Derivatives. 7. Synthesis and Antitumor-Activity of Alpha-Substituted and Gamma-Substituted Methotrexate Analogs, *Tetrahedron 44*, 5375-5387.

32. Chiu, H. P., Suzuki, Y., Gullickson, D., Ahmad, R., Kokona, B., Fairman, R., and Cheng, R. P. (2006) Helix propensity of highly fluorinated amino acids, *J. Am. Chem. Soc. 128*, 15556-15557.

33. Lee, H. Y., Lee, K. H., Al-Hashimi, H. M., and Marsh, E. N. G. (2006) Modulating protein structure with fluorous amino acids: increased stability and native-like structure conferred on a 4-helix bundle protein by hexafluoroleucine, *J. Am. Chem. Soc. 128*, 337-343.

34. Gottler, L. M., de la Salud-Bea, R., and Marsh, E. N. G. (2008) The fluorous effect in proteins: properties of α4F6, a 4-α-helix bundle protein with a fluorocarbon core, *Biochemistry 47*, 4484-4490.

35. Shelburne, C. E., An, F. Y., Dholpe, V., Ramamoorthy, A., Lopatin, D. E., and Lantz, M. S. (2007) The spectrum of antimicrobial activity of the bacteriocin subtilosin A, *J. Antimicrob. Chemother. 59*, 297-300.

36. Huhta, M. S., Chen, H. P., Hemann, C., Hille, C. R., and Marsh, E. N. G. (2001) Protein-coenzyme interactions in adenosylcobalamin-dependent glutamate mutase, *Biochem. J. 355*, 131-137.

37. Gottler, L. M., Lee, H. Y., Shelburne, C. E., Ramamoorthy, A., and Marsh, E. N. G. (2008) Using fluorous amino acids to modulate the biological activity of an antimicrobial peptide, *ChemBioChem 9*, 370-373.

38. Lau, E. Y., and Gerig, J. T. (2000) Origins of fluorine NMR chemical shifts in fluorine-containing proteins?, *J. Am. Chem. Soc. 122*, 4408-4417.

39. Dubois, B. W., and Evers, A. S. (1992) ^{19}F-NMR spin-spin relaxation (T2) method for characterizing volatile anesthetic binding to proteins. Analysis of isoflurane binding to serum albumin, *Biochemistry 31*, 7069-7076.

40. Luz, Z., and Meiboom, S. (1963) Nuclear Magnetic Resonance Study of Protolysis of Trimethylammonium Ion in Aqueous Solution - Order of Reaction with Respect to Solvent, *J. Chem. Phys. 39*, 366-369.

41. Fukaya, H., and Ono, T. (2004) DFT-GIAO calculations of ^{19}F NMR chemical shifts for perfluoro compounds, *J. Comput. Chem. 25*, 51-60.

42. Liu, Z., and Goddard, J. D. (2009) Predictions of the fluorine NMR chemical shifts of perfluorinated carboxylic acids, CnF(2n+1)COOH (n = 6-8), *J. Phys. Chem. A 113*, 13921-13931.

Chapter 3

Alternative Pathways of Human Islet Amyloid Polypeptide Aggregation Distinguished by ^{19}F NMR-Detected Kinetics of Monomer Consumption

3.1. Introduction

The work described in this chapter has been published as: "Alternative Pathways of Human Islet Amyloid Polypeptide Aggregation Distinguished by ^{19}F NMR-Detected Kinetics of Monomer Consumption." Yuta Suzuki, Jeffrey R. Brender, Kevin Hartman, Ayyalusamy Ramamoorthy, and E. Neil G. Marsh (2012) Biochemistry, 51 (41), 8154 − 8162 (1). The co-authors were very helpful in conducting this research and analyzing the results. Dr. Hartman assisted me with fluorescent experiments and acquiring electron microscopy data. Numerous suggestions and guidance on experiments came from Dr. Jeffrey R. Brender and Prof. Ayyalusamy Ramamoorthy.

The formation of amyloid fibers is associated with a wide range of pathologies including Alzheimer's disease, Parkinson's disease, and type II diabetes (2). Under pathological conditions, amyloidogenic proteins self-assemble into long fibrillar structures with a characteristic β-sheet core (3-5). Although a detailed mechanism is lacking for most amyloidogenic proteins, amyloidogenesis is believed to be a complex, multi-step process,

typically involving the formation of energetically unfavorable intermediates before the formation of the final amyloid product (Figure 1.8) (6-9).

Because amyloid formation is such a complex process, a full understanding of the pathology caused by amyloid formation requires establishing both the identity of intermediates along the amyloid pathway and the kinetics of their formation. The actual identity of the species responsible for toxicity is elusive and has been the subject of much debate since the discovery of amyloid plaques more than a century ago (8-10). A current hypothesis holds that small to intermediate size (~5-6 nm in diameter) oligomers may be responsible for much of the toxicity of amyloid proteins (7, 9). For the Aβ protein, probably the best studied amyloidogenic protein, oligomers of this type have been isolated both *in vitro* and *in situ* from tissue samples of Alzheimer's patients. While a large body of literature exists linking small oligomers of this type to the pathological action of other amyloidogenic proteins besides Aβ, their actual existence in many other amyloidogenic proteins has largely been inferred rather than directly tested (8). For IAPP in particular, the existence of small oligomeric species of this type is controversial (8, 9). Most attempts at detection has used the conformation-specific antibody A11, whose specificity towards non-Aβ oligomers has been called into question (8), as it appears to give both false positives and false negatives under some conditions (8, 11-14). Attempts at direct detection of these oligomers have largely been negative, although these experiments have used an equilibrium approach that may not detect transient oligomers (15, 16). In the absence of well-defined targets, research attempting to attenuate amyloid-linked toxicity has been substantially impeded.

Towards this end, various methods have recently been exploited to monitor the kinetics of amyloid fibril formation including fluorescence (17-20), NMR (21, 22), 2D-infrared (23, 24),

and mass spectroscopy (25, 26). The most common method for measuring amyloid formation exploits the increase in fluorescence when the dye, ThT binds to the fibers. Although the ThT assay is simple and relatively sensitive, it does not accurately distinguish between oligomeric species (27). Therefore, it is not particularly useful by itself to investigate amyloidogenic intermediates. Similarly, reporters of secondary structures such as CD, Fourier transform infrared and multidimensional NMR spectroscopy have difficulty in detecting the underlying spectral signature of the intermediate species, which may be transient and not form a majority of the total population.

On the other hand, real-time ^{1}H NMR measurements, in theory, allow the signal from each species to be resolved and analyzed independently. Unfortunately, ^{1}H NMR is relatively insensitive to changes in structure due to small chemical shift dispersion associated with the ^{1}H nucleus. Whereas ^{13}C and ^{15}N experiments are more sensitive to environmental changes, the low sensitivity of these nuclei makes it difficult to acquire data sufficiently rapidly to track intermediates during aggregation. In contrast, ^{19}F combines both excellent sensitivity and large chemical shift dispersion, making it an excellent reporter for changes in the chemical environment (28, 29). Thus ^{19}F NMR has been broadly applied to investigate protein conformational changes and dynamics as well as protein-ligand and protein-membrane interactions in biological systems (30-42) as described in chapter 1. Whereas the properties of ^{19}F NMR spectroscopy are attractive for amyloid research, applications to amyloid proteins have been relatively limited (43, 44). In particular, detailed time-resolved studies of protein aggregation or inhibition assays using ^{19}F NMR have not been performed.

In this chapter, I demonstrate the utility of ^{19}F NMR to provide a direct, sensitive and real-time measurement of amyloid formation by the highly amyloidogenic peptide, IAPP, which

is achieved by monitoring the consumption of monomeric protein rather than the formation of fibrils by dye binding. IAPP is a 37-residue peptide hormone secreted from pancreatic β-cells along with insulin to contribute to glycemic control (45). However, an insoluble fibril form of IAPP is found in the pancreas of up to 90% of patients with type II diabetes that may contribute to the pathology of the disease (8, 9, 46, 47). Using real-time ^{19}F NMR in combination with other techniques to measure conformational changes during the aggregation pathway, I show IAPP forms fibers from monomeric IAPP at pH 7.3 without an appreciable buildup of small oligomeric intermediates during aggregation, in contrast to most amyloidogenic proteins (7). However, this pathway can be altered towards the formation of non-fibrillar intermediates using inhibitors such as EGCG.

3.2. Experimental Procedures

3.2.1. Peptide Preparation

Peptide (IAPP-tfmPhe23) was synthesized manually in the free acid form by solid-phase Fmoc-based chemistry using pseudoproline dipeptides to disrupt aggregation during synthesis, as described previously (48). Fluorinated Phe, tfmPhe **2** (Figure 1.2) was used to replace Phe at position 23.

Peptide sequence: KCNTATCATQRLANFLVHSSNN(tfmPhe)GAILSSTNVGSNTY

The disulfide bridge between Cys2 and Cys7 in IAPP was formed on the resin using thallium (III) trifluoroacetate as a mild oxidant, and cleaved from resin using 95% TFA (48). Crude peptides were dissolved in 35% acetic acid (v/v) and purified on a reverse-phase HPLC using a Waters semi-preparative C18 column equilibrated in 0.045% HCl. The peptides were eluted with a linear gradient of 0% to 80% acetonitrile at a flow rate of 10 ml/min. Peptide

identity was confirmed using MALDI-MS.

3.2.2. Sample Preparation

To remove preformed aggregates, the purified peptide was dissolved in hexafluoroisopropanol followed by the removal of the solvent by lyophilization. A 850 μM stock solution was made before each set of experiments by first dissolving the lyophilized peptide in 0.1 mM HCl (pH 4.0). The stock solution was then passed though a 0.22 μm filter before dilution into the final buffer solution immediately before the start of each experiment. The concentrations of peptide stock solutions were determined by the absorbance of tyrosine 37 in water ($\varepsilon = 1215$ L mol^{-1} cm^{-1} at 280 nm) (49). All experiments were performed at a constant peptide concentration of 85 μM. The final solutions contained 20 mM sodium phosphate, 50 mM NaCl (pH 7.3), 10% D$_2$O, and various concentrations of EGCG, ThT, and 1-Ethyl-3-(3-dimethylaminopropyl)carbodiimide hydrochloride (EDC) and *N*-hydroxysulfosuccinimide (Sulfo-NHS) as indicated in the figure captions. For NMR measurements, ^{19}F chemical shifts were referenced to an internal standard of trifluoroethanol (TFE) (100 μM, at 0 ppm).

3.2.3. Kinetic Studies Using ^{19}F NMR Spectroscopy

All ^{19}F NMR experiments were performed using a Varian VNMRS 500 MHz NMR spectrometer equipped with a double-tuned ^{1}H-^{19}F probe. After the addition of peptide into the NMR solution, a series of ^{19}F spectra were recorded without spinning. Each ^{19}F spectrum takes 116 s using 64 transients (25°C and 37 °C) or 232 s using 128 transients (10 °C) with a 1.0 s pulse delay between each transient. Line broadening of 3.0 Hz was used to process the final

spectra. All of the samples were pre-equilibrated at the indicated temperatures before mixing with peptide stock solution. Origin 8.5 was used for plotting and fitting the data (50).

3.2.4. Kinetic Studies Using ThT Fluorescence

The kinetics of IAPP amyloid formation was measured using the increase in fluorescence intensity observed when the amyloid specific dye ThT binds to the amyloid fibrils. The samples were prepared as described above for the NMR solution except that 100 uM ThT was premixed with buffer solution before the addition of peptide. Time traces were recorded with a FluoroMax-2 spectrofluorometer using a 440 nm excitation filter and a 485 nm emission filter at a constant temperature without shaking.

3.2.5. Kinetic Studies Using Circular Dichroism

CD measurements were performed with an Aviv 62DS spectropolarimeter using a 0.1 cm pathlength cell. The samples were prepared as described above for the NMR solution. Mean residue ellipticities, $[\theta]$, were calculated using $[\theta] = \theta_{obsd}/(10lcn)$ where θ_{obsd} is the ellipticity measured in millidegrees, c is the molar concentration, l is the cell path length in centimeters, and n is the number of residues in the peptide. Full spectra were smoothed by Savitzky-Golay smoothing (5 point window).

3.2.6. Transmission Electron Microscopy

Aliquots were directly taken from the NMR or ThT samples at the time-points indicated. 6 μL aliquots were incubated onto Formvar-coated copper grids (Ernest F. Fullam, Inc., Latham, NY) for 2 min, washed five times with 6 μL of deionized water, and then negatively stained for 1 min with 2% uranyl acetate. Samples were imaged using a Philips CM10 Transmission Electron Microscope.

3.3. Results and Discussion

3.3.1. ^{19}F NMR Sensitively Measures Monomer Consumption During Aggregation

To study fibril formation using ^{19}F NMR, I synthesized a ^{19}F-labeled IAPP (IAPP-tfmPhe23) in which Phe23 is substituted by tfmPhe. Phe23 is solvent exposed in the unstructured monomeric peptide (19, 51), but is believed to be become buried when the peptide forms aggregates (3, 19, 52, 53). The ^{19}F chemical shifts and line-widths of the trifluoromethyl groups should change significantly as the peptide changes its secondary structure and oligomerization state, as has been observed for other fluorinated peptides and proteins (39-41). In particular, if oligomeric intermediates on the amyloid-forming pathway accumulate to an appreciable extent they should be detectable by NMR, provided they are not so large that their line-widths are broadened excessively, as is the case for amyloid fibers (21). Furthermore, the ^{19}F signal is sufficiently sensitive to monitor peptide aggregation at low concentrations that allows a direct comparison with other methods for following aggregation such as CD or fluorescence spectroscopy (Figure 3.1).
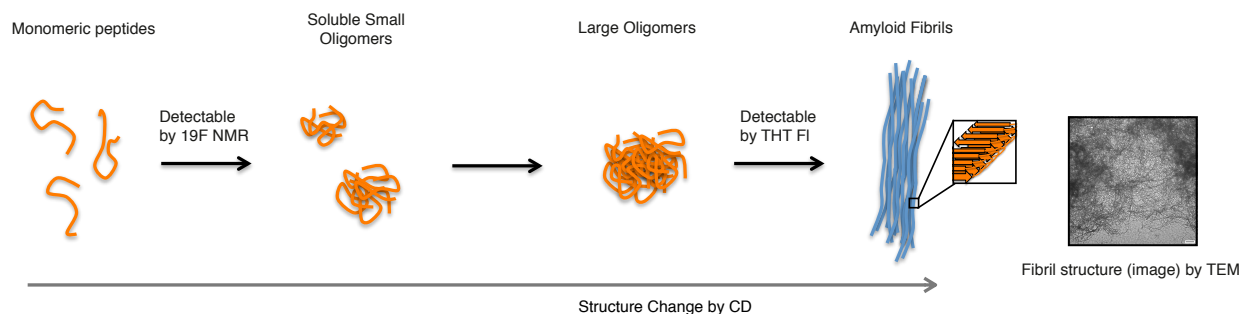
Figure 3.1. Cartoon showing the sensitivities of each method.

The sensitivity of the ^{19}F chemical shift of the tfmPhe23 group to changes in environment was investigated by examining the ^{19}F spectra in different environments (Figure 3.2). A detectable change was noticed for almost all changes in environment, including a substantial change in the chemical shift in urea, even though IAPP is considered to be natively unfolded (51).

The consumption of monomeric IAPP-tfmPhe23 (initial concentration 85 μM in 20 mM sodium phosphate, 50 mM NaCl pH 7.3) during amyloid fibrillogenesis was monitored by ^{19}F NMR (Figure 3.3). The monomeric peptide exhibits a single sharp peak near 14.7 ppm in the NMR spectrum. As expected, the signal intensity due to the monomeric peptide decreased in intensity over time in the characteristic sigmoidal manner observed in many studies of amyloid fiber formation (54-56). No signal was observed due to the large amyloid fibers as the peaks are broadened beyond detection. To determine the sensitivity of this method, the rate of monomer consumption was detected by measuring changes in ^{19}F NMR signal intensity changes at three different temperatures: 10, 25 and 37 °C (Figure 3.3). As expected, both the lag time and elongation rate of fibril formation were temperature dependent (15, 16, 57). Even at higher

temperatures (37 °C) and accelerated aggregation rates, I was able to monitor monomer

consumption during aggregation efficiently using this technique
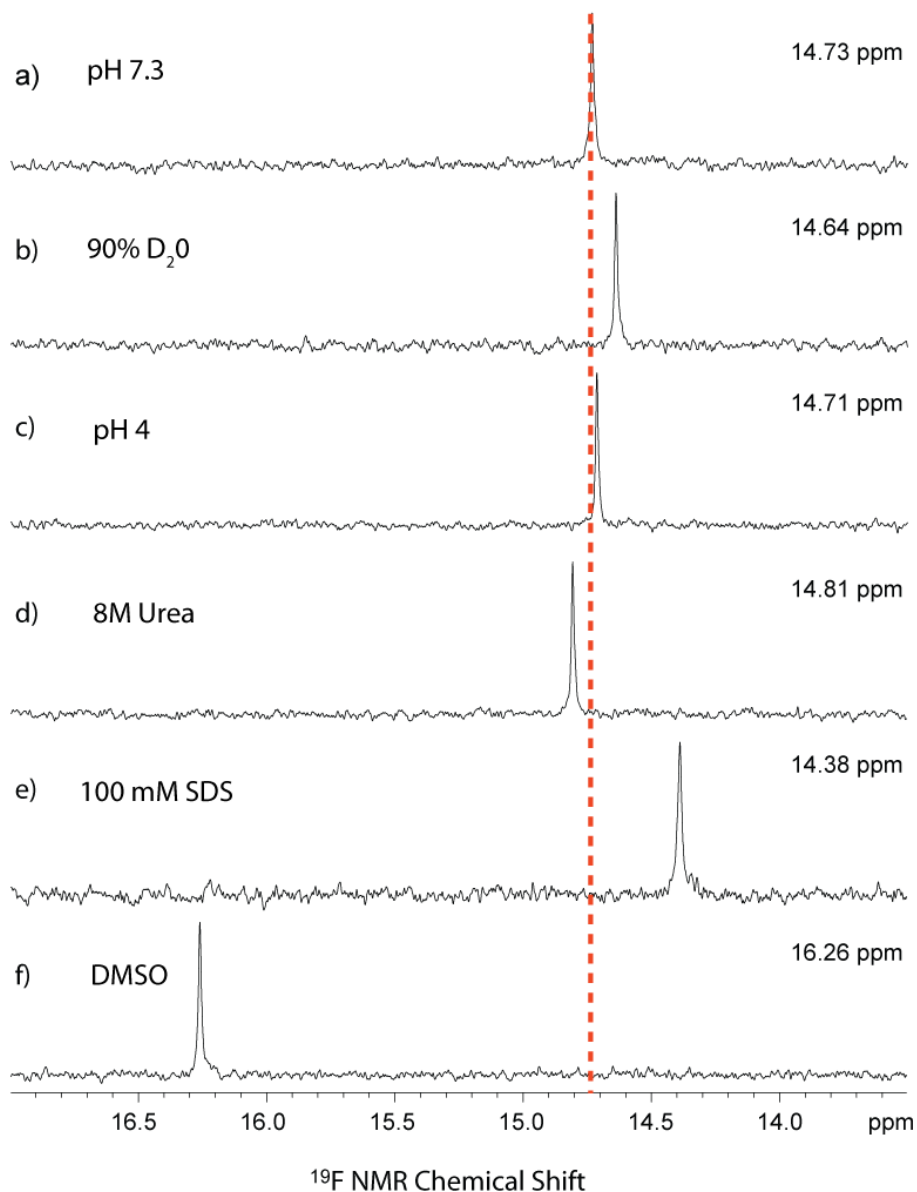
Figure 3.2. Environmental sensitivity of the tfmPhe23 group. ^{19}F NMR spectra of IAPP-tfmPhe23 were acquired under various conditions after 5 minutes of incubation at 25 °C: **(a)** 20 mM sodium phosphate, 50 mM NaCl, 10% D$_2$O, pH 7.3 **(b)** 90% D$_2$O, 20 mM sodium phosphate, 50 mM NaCl, pH 7.3 **(c)** 100 µM HCl, 10% D$_2$O, pH 4 **(d)** 8M Urea, 10% D$_2$O **(e)** 100 mM SDS, 20 mM sodium phosphate, 20 mM NaCl, 10% D$_2$O, pH 7.3, **(f)** 90% DMSO, 10% D$_2$O. Spectra were referenced to an external TFE standard (in solution of 20 mM Pi, 50 mM NaCl, pH 7.3) at 0 ppm.
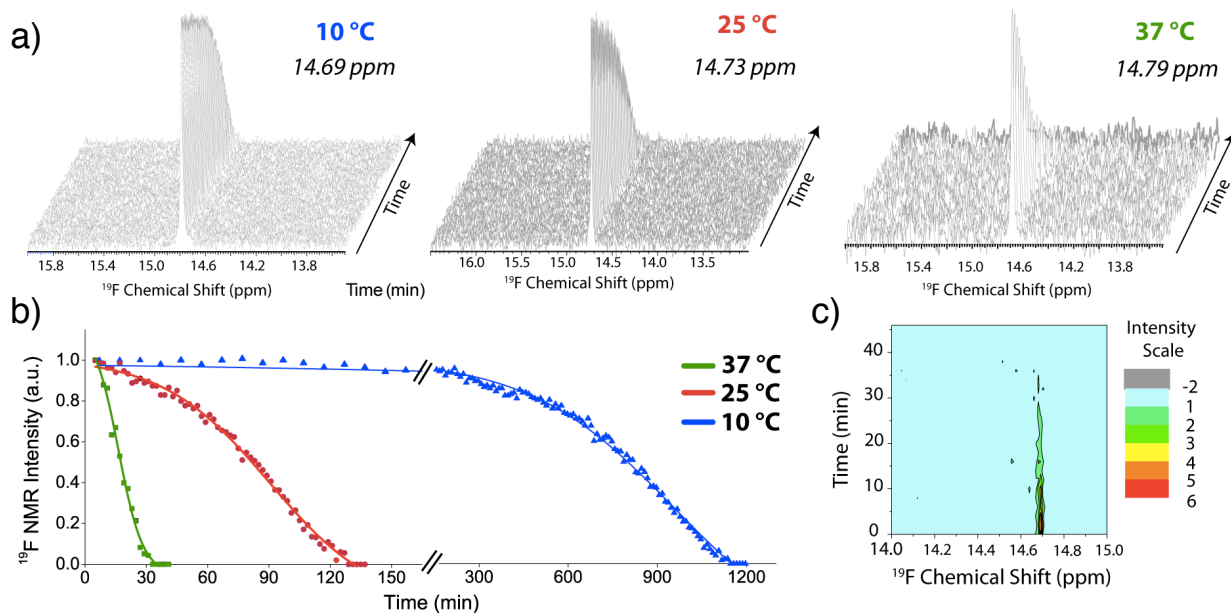
Figure 3.3. Kinetics of the disappearance the IAPP-tfmPhe23 monomer followed by ^{19}F NMR. (a) Stacked plots of ^{19}F NMR spectra (TFE = 0.0 ppm). The experiment was conducted at 10 °C (left), 25 °C (center), and 37 °C (right) at pH 7.3 **(b)** Plots of peak intensity of the main resonance from (A) as a function of time. Solid lines represent sigmoidal fits to the ^{19}F data. **(C)** Contour plot of the ^{19}F NMR spectra at 37 °C showing the absence of new peaks.

3.3.2. IAPP-tfmPhe23 Forms Fibers from Monomers without Accumulation of Non-fibrillar Intermediates

No additional peaks were observed in the ^{19}F spectrum of the peptide during the time-course of the experiment, even at 10 °C where fibril formation is slowest (Figure 3.3). The position of the main resonance also did not change over the course of the experiment (Figure 3.3c), consistent with fluorescence studies that show Phe-23 remains exposed during the lag-phase of aggregation (19). It was also confirmed that tfmPhe23 is actually sensitive to the formation of small oligomers, were they to be formed in significant concentrations by cross-linking IAPP-tfmPhe23 with EDC/sulfo-NHS (58). In contrast to IAPP-tfmPhe23 alone,

additional peaks can clearly be seen downfield of the main peak when IAPP-tfmPhe23 is incubated with various concentration of EDC/sulfo-NHS (Figure 3.4). The intensity of the additional peaks increase with time as the main peak decreases, confirming its presence is the result of the cross-linking reaction.
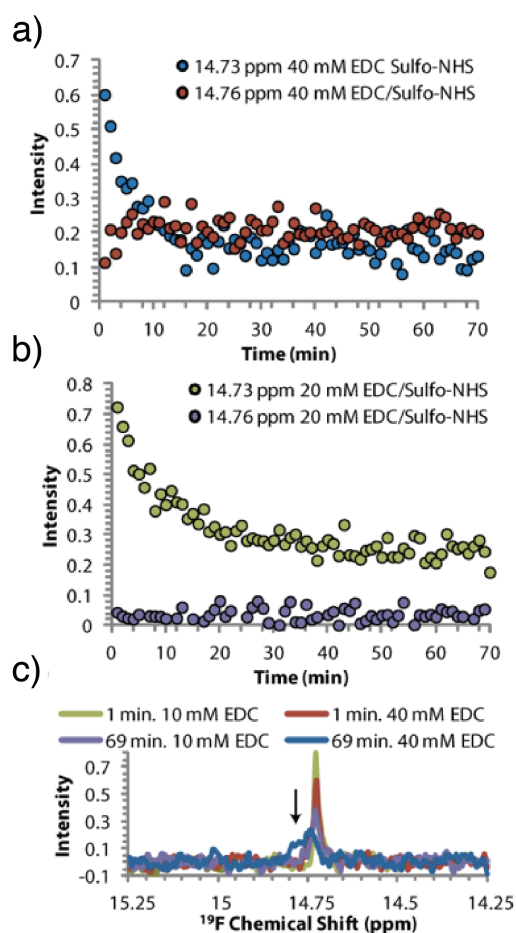
Figure 3.4. Changes in the ^{19}F spectra of IAPP-tfmPhe23 upon cross-linking. (a, b) Intensity change with time of the main peak at 14.73 ppm and the second peak at 14.76 ppm with 40 mM **(a)** and 10 mM **(b)** EDC/Sulfo-NHS. **(c)** Superposition of the first and final spectra of IAPP-tfmPhe23 with 40 and 10 mM EDC/Sulfo-NHS. The position of the second peak at 14.76 ppm is indicated by an arrow.

It is also important to note that even if an oligomer population is not directly detectable by ^{19}F NMR because it is either structurally inhomogeneous (which would broaden the signal),

too large to be detected by NMR, or the IAPP-tfmPhe23 ^{19}F NMR shift is unaffected by oligomerization, it still may be indirectly detected by a comparison of the monomer loss curves observed by ^{19}F NMR and the ThT and CD measurements of amyloid formation. If large oligomers or undetectable oligomers accumulate to a significant extent, a delay between the disappearance of monomer (as measured by NMR) and the appearance of fibrils (as measured by ThT fluorescence and CD) would be observed (22, 59).
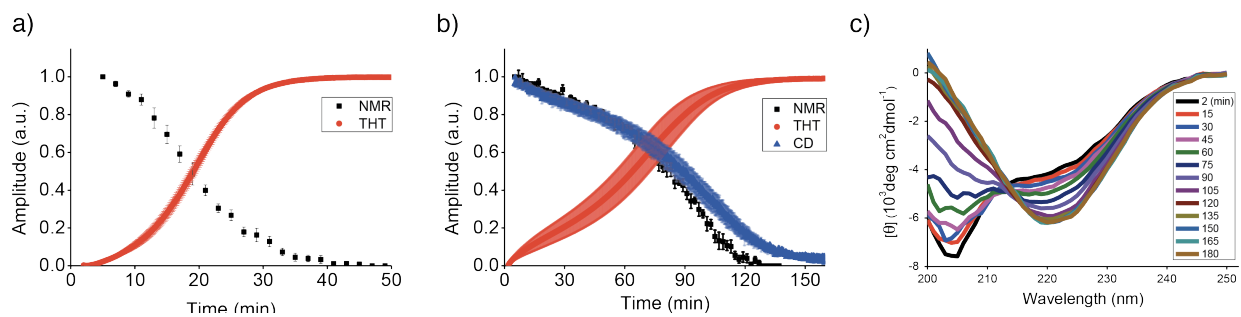
Figure 3.5. Comparison of the rates of monomer consumption and fiber formation (a) Overlay of kinetic traces from ^{19}F NMR (black), ThT fluorescence (red) at 37 °C. Error bars indicate S.E.M. (n=4). **(b)** Overlay of kinetic traces from obtained ^{19}F NMR (black), ThT fluorescence (red), and CD (blue) at 25 °C. Error bars indicate standard error of measurement (n=4 for NMR and CD and n=5 for ThT). The close correspondence between the curves suggests fiber formation closely follows monomer consumption at 25 °C, similar to the measurements at 37 °C. **(c)** CD spectra showing the time evolution of secondary structure.

To test this possibility, I followed the aggregation of similarly prepared samples of IAPP-tfmPhe23 by ThT fluorescence, CD spectroscopy, and ^{19}F NMR (Figure 3.5, parameters from the sigmoidal fit can be found in Table 3.1). The rate of monomer consumption of IAPP-tfmPhe23 closely matches the rate of amyloid formation when performed under identical buffer and peptide concentrations at 25 and 37 °C (Figure 3.5). The ThT and NMR curves match well at 37°C ($t_{1/2}$=18.8±0.8 and 16.8±1.6, respectively, p=0.30) and the CD and NMR curves match very

closely at 25°C ($t_{1/2}$=91.8±6.3 and 91.9±3.1, respectively, p=0.99). A relatively small (in this context) but statistically significant (p=0.02) difference was observed between the ThT and NMR curves at 25 °C ($t_{1/2}$=64.3±6.9 and 91.9±3.1, respectively). This small difference in the kinetics between the two measurements may be caused by differences between the shape and size of the NMR tube and fluorescence cuvette, as interactions between sample and container surfaces are known to nucleate amyloid formation (60-62). This difference is magnified at the slower nucleation rates occurring at lower temperatures (60).

NMR/CD	ThT
$I = 1 - \dfrac{1}{1 + e^{\frac{x-t_{1/2}}{dx}}}$	$I = 1 - \dfrac{1}{1 + e^{\frac{x-t_{1/2}}{dx}}}$

25°C	$t_{1/2}$	dx
ThT	64.3±6.9	17.4±1.3
NMR	91.9±3.1	24.9±1.4
CD	91.8±6.3	22.8±1.4

37°C	$t_{1/2}$	dx
ThT	18.8±0.8	4.2±0.2
NMR	16.8±1.6	6.1±0.7

Table 3.1. Parameters from the sigmoidal fit of Figure 3.5.

The fact that the NMR, CD, and ThT curves closely track each other suggests the monomeric peptide is converted into a large, mostly β-sheet, ThT-reactive species without the substantial accumulation of non-fibrillar intermediates. The absence of a substantial population of non-fibrillar oligomeric species along the aggregation pathway is notably different from what

has been observed for many other amyloidogenic proteins (17, 63, 64). For example, many intermediate species are formed during the aggregation of Aβ, including a distinct α-helical intermediate (12, 17, 63-65). Systems that are known to have non-fibrillar oligomeric intermediates typically show a much larger difference in rates of monomer depletion and fiber formation. For example, the midpoints of the monomer consumption and fiber formation curves of Aβ can differ by an order of magnitude (17). Similarly, monomer consumption and fiber formation curves of the curli protein CsgA differ by a factor of 2 (22). The correspondence between the curves suggests any transient oligomers that are formed by IAPP-tfmPhe23 comprise only a minor population of the total at any given point in time.

The close coincidence of the midpoints of aggregation determined by the ^{19}F NMR and the ThT and CD measurements impose fairly stringent requirements on the type of non-fibrillar oligomers that can be formed. However, the data do not distinguish between certain kinetic mechanisms. For example, our data cannot exclude the presence of large, off-pathway oligomers whose concentration does not change appreciably in the lag-phase of aggregation (15, 16). In addition, transient oligomers that do not accumulate to a significant extent will not be observed in the experiment (16).

Transmission electron microscopy (TEM) images acquired at the mid- and end-points of aggregation also support this conclusion (Figure 3.6). Images taken at the mid-point of aggregation show fibers that are similar in morphology to those found at the end-point but with a smaller density of fibers on the grid (Figure 3.6b). Non-fibrillar aggregates large enough to be resolved in the TEM image, such as the spherical and annular intermediates frequently detected for α-synuclein and Aβ and implicated in toxicity, are noticeably absent (7, 65).

a)

b)
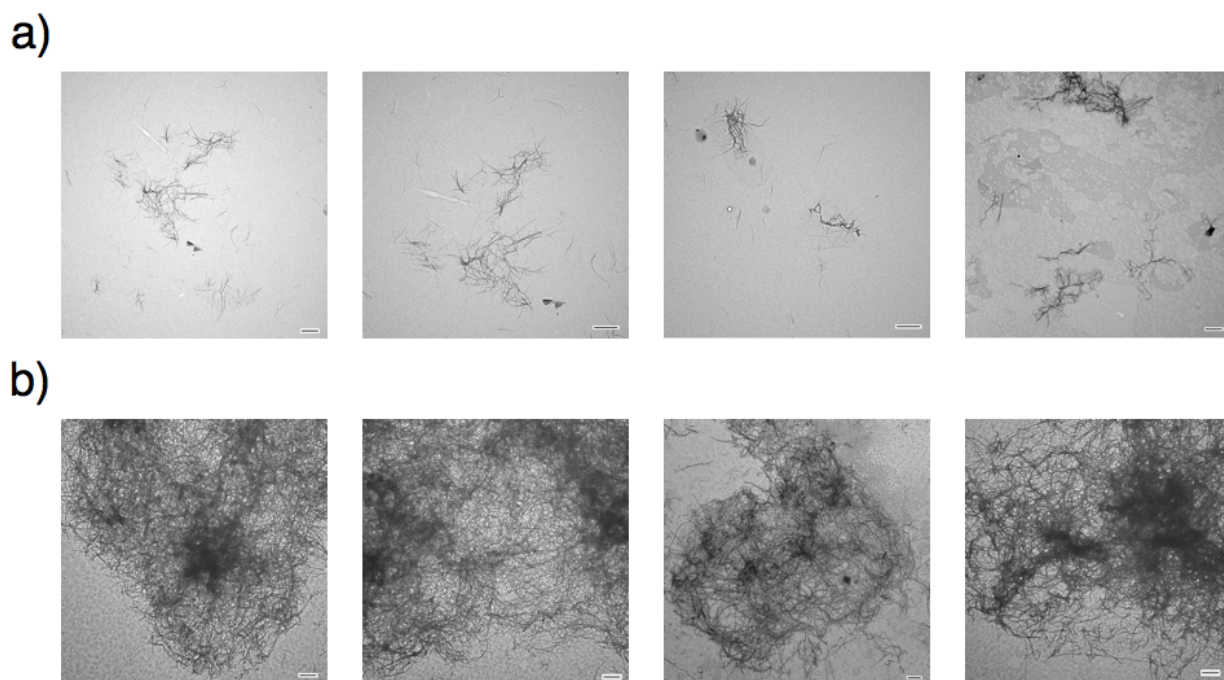
Figure 3.6. TEM images of IAPP-tfmPhe23 after ½ (a) and complete (b) depletion of the ^{19}F signal intensity at 25 °C. Scale bars represent 500 nm.

3.3.3. ^{19}F NMR Measurement of the Interaction of Polyphenolic Inhibitor, EGCG with IAPP without Interference from External Probe, ThT

Having demonstrated the utility of ^{19}F NMR to follow the kinetics of amyloid formation, the technique was used it to investigate the mechanism by which EGCG (Figure 3.7a) inhibits IAPP-tfmPhe23 amyloid formation. EGCG is the most abundant catechin found in tea and is a potent antioxidant, making it a potential therapeutic for many disorders. It has been reported that EGCG inhibits fiber formation *in vitro* for many amyloidogenic proteins including Aβ, α-synuclein, and polyglutamine peptides (66-71). Meng et al recently showed that EGCG not only inhibits IAPP amyloid formation effectively but is one of the few small molecule compounds that also disaggregates IAPP amyloid fibrils *in vitro* (68). However, the mechanism of inhibition by EGCG is not known for IAPP (68). Optical measurements of fiber inhibition by EGCG and

other polyphenols are complicated by the background signal from these compounds and, potentially, by competitive binding with extrinsic probes like ThT (67, 72-75). In contrast, measurements of the rate of monomer consumption by ^{19}F NMR are easily quantified and are not affected by the nature of the inhibitor.

The kinetics of IAPP-tfmPhe23 aggregation were studied in the presence of 0.2, 0.5, 1.0, and 5.0 molar equivalents of EGCG by ^{19}F NMR and ThT fluorescence (Figure 3.7b and c). It is apparent from both the ^{19}F and ThT measurements that EGCG inhibits fiber formation in a dose-dependent manner. However, a comparison of the data in Figures 3.7b and 7c reveals some important differences between the ThT and ^{19}F NMR measurements of the apparent effects of EGCG. When IAPP is incubated with an excess of EGCG (green lines in Figures 3.7b and c), the ThT assay shows a complete inhibition of fiber formation while the ^{19}F NMR measurement shows a slow but steady decrease at longer time-periods. This delay between the disappearance of monomer and the appearance of fibrils is consistent with the production of large non-fibrillar aggregates that are not fluorescent when incubated with ThT (66).
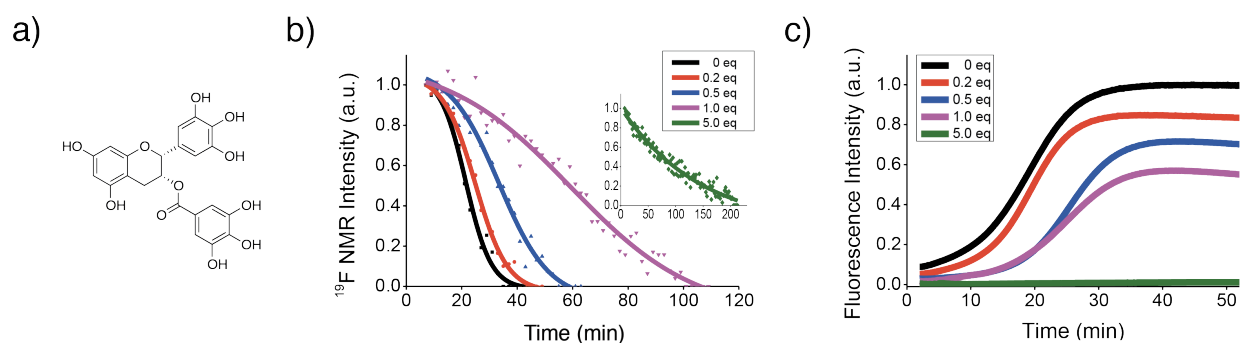
Figure 3.7. EGCG inhibits IAPP-tfmPhe23 amyloid fibrillogenesis (a) Structure of EGCG. (b, c) Time course for peptide aggregation followed by ^{19}F NMR (b) and ThT fluorescence (c) of IAPP-tfmPhe23 alone (85 μM, black) and at 1:5 (red) 1:2 (blue), 1:1 (magenta), 5:1 (57) molar ratios of EGCG to IAPP at pH 7.3, 37°C. Solid lines represent sigmoidal fits to the ^{19}F data. 100 μM ThT is present in the ThT samples (c) but is absent in the NMR samples (b).

This interpretation is supported by the analysis of TEM images taken at the end-points of aggregation, which show the appearance of large non-fibrillar aggregates at higher concentrations of EGCG but with a greatly reduced density of fibers (Figure 3.8). However, the TEM images are not definitive by themselves as EGCG by itself polymerizes over time to form aggregates with a similar morphology as the aggregates seen in Figure 3.8 (Figure 3.9) (17). While the delay between the disappearance of monomer and the appearance of fibrils is indicative of the formation of large non-fibrillar aggregates, sub-stoichiometric amounts of EGCG shift the ^{19}F NMR curve to later times relative to ThT measurements (blue and pink curves in Figure 3.7b and 3.7c, 0.5 and 1 equivalent of EGCG respectively). This result seems to imply that the monomer disappears *after* the appearance of fibrils at low concentrations of EGCG. This apparent contradiction is most likely due to interfence by EGCG with ThT binding assay as discussed below.
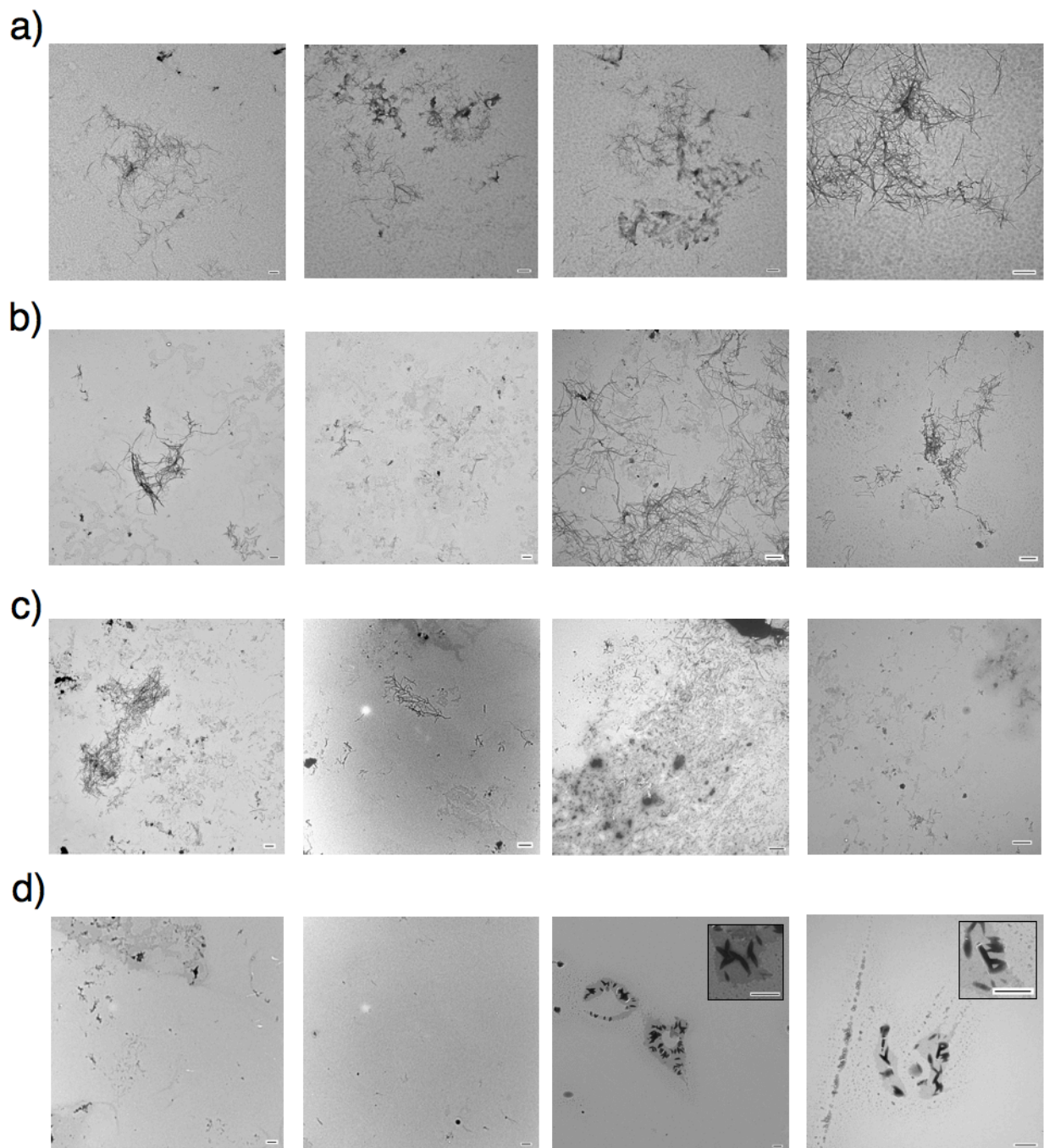
Figure 3.8. TEM images of IAPP-tfmPhe23 aggregation as a function of EGCG concentration. TEM images after the complete depletion of the ^{19}F signal for IAPP-tfmPhe23 in the presence of **(a)** 0.2 eq, **(b)** 0.5 eq, **(c)** 1.0 eq, and **(d)** 5.0 eq of EGCG in the absence of ThT. Scale bars represent 500 nm.
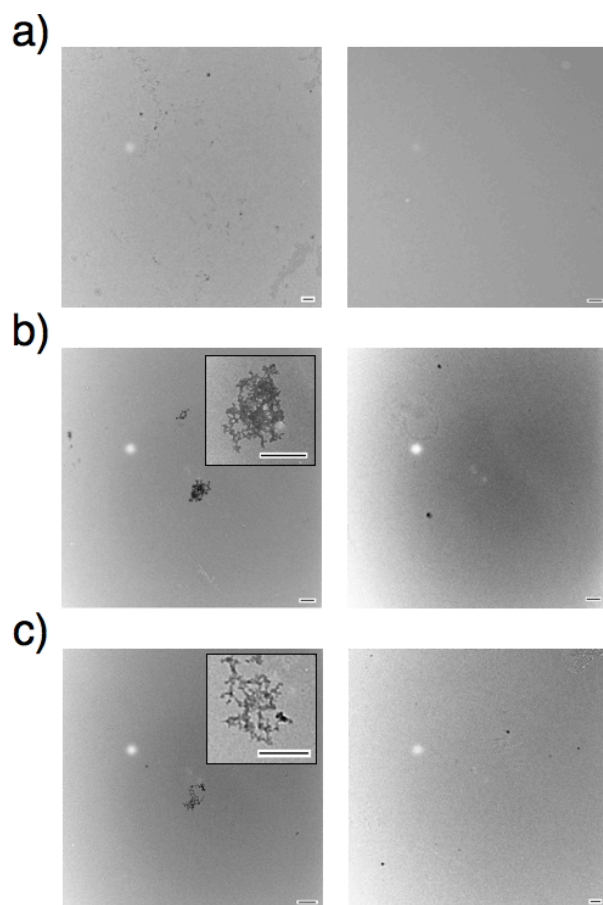
Figure 3.9. TEM images of aggregate formation by EGCG in the absence of IAPP-tfmPhe23. (a) phosphate buffer alone (20 mM Pi, 50 mM NaCl, pH 7.3), (b) 425 μM EGCG in phosphate buffer, and (c) 425 μM EGCG with 100 μM THT in phosphate buffer. Samples were incubated for 3 hours at 37 °C before acquisition. Scale bars represent 500 nm.

3.3.4. ThT and EGCG Competitively Bind to IAPP Fibers

In Figure 3.7, 100 μM ThT is present during the ThT assay but not in the NMR measurements. To determine more accurately the effect of ThT on EGCG inhibition, we first determined if ThT by itself has any effect on amyloid aggregation. The rate of disappearance of monomer was not significantly changed by the presence of ThT (Figure 3.10), indicating that ThT by itself does not affect the kinetics of fiber formation.

67
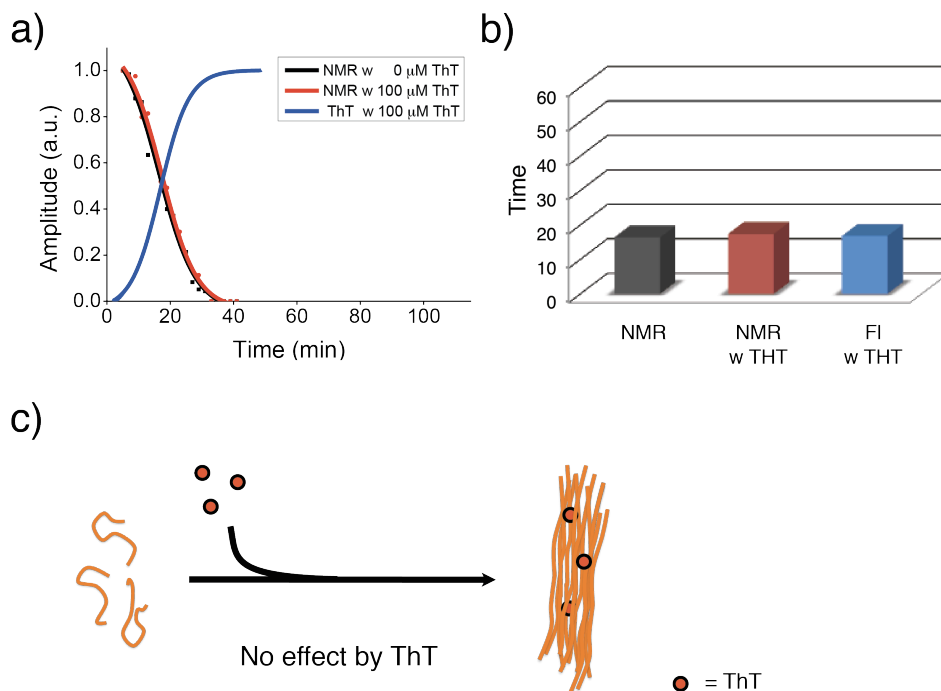
Figure 3.10. Effect of ThT for amyloid fiber formation (a) Overlay of kinetic traces from ^{19}F NMR (black: 0 μM ThT and red: 100 μM ThT) and ThT fluorescence (blue: 100 μM ThT). Solid lines represent sigmoidal fits to the ^{19}F data. (b) $t_{1/2}$ from kinetic traces (a). (c) Cartoon schematic of ThT binding to amyloid fiber.

However, although ThT has little effect on the rate of monomer depletion on its own, it may indirectly influence the rate of aggregation by significantly attenuating the inhibitory effect of EGCG. If ThT competes for the same binding site as EGCG on the amyloid fiber, the decrease in the amount of bound EGCG in the ThT assay would be reflected in lower levels of inhibition. This effect would not be observable when EGCG is in great excess of ThT (green lines Figure 3.7b and 3.7c).

To check for this possibility, the ^{19}F measurements were performed using the same concentration of ThT as in the ThT assay (100 μM, Figure 3.11). In samples with EGCG, the addition of ThT causes a substantial shift of the NMR curves to earlier times, indicating monomer depletion happens at a faster rate in samples with EGCG when ThT is present (Figure

3.11). This shift is not observed in samples without EGCG. This finding indicates that while ThT has little effect on the rate of aggregation by itself, it significantly attenuates the inhibitory effect of EGCG, consistent with ThT effectively competing with EGCG for binding to IAPP fibrils. Similarly, the observation that high concentrations of EGCG prevent amyloid fiber formation (Figure 3.7c) may be attributed to effective competition of EGCG for ThT binding sites when it is in sufficient excess over ThT.
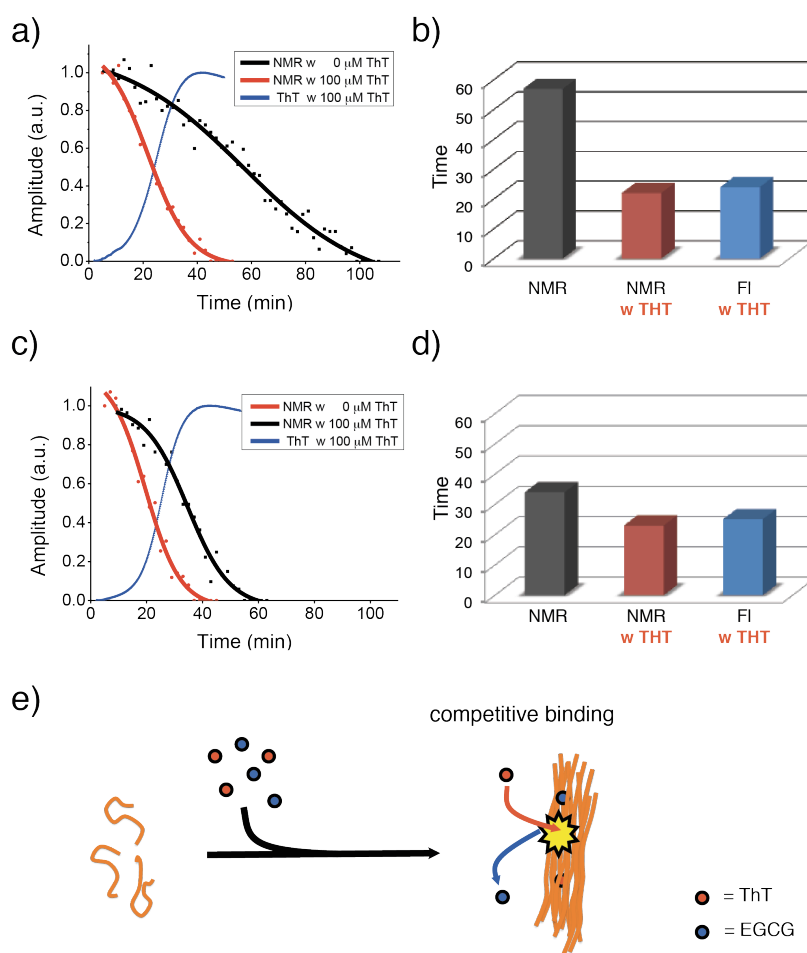
Figure 3.11. Competition for amyloid binding between ThT and EGCG (a) Overlay of kinetic traces from ^{19}F NMR (black: 0 μM ThT and red: 100 μM ThT) and ThT fluorescence (blue: 100 μM ThT) in the presence of 1 equivalents of EGCG to peptide. Solid lines represent sigmoidal fits to the ^{19}F data. (b) $t_{1/2}$ from kinetic traces. (a). (c) Kinetic traces obtained under the same conditions as (a) but performed in the presence of 0.5 equivalents of EGCG. (d) $t_{1/2}$ from kinetic traces (c). (e) Cartoon schematic of competitive binding effect between ThT and EGCG.

69

3.3.5. EGCG Diverts Amyloid Aggregation to Non-fibrillar Aggregates

Given the many proposed modes of action of polyphenolic compounds against amyloidogenic proteins, it is difficult to determine the precise mechanism by which EGCG inhibits IAPP amyloid formation. The chemical shift of IAPP-tfmPhe23 was unchanged by the presence of either EGCG or ThT, indicating neither compound binds to the monomeric peptide, as has been proposed to happen for some amyloidogenic proteins (Figure 3.12) (67, 71, 76, 77).
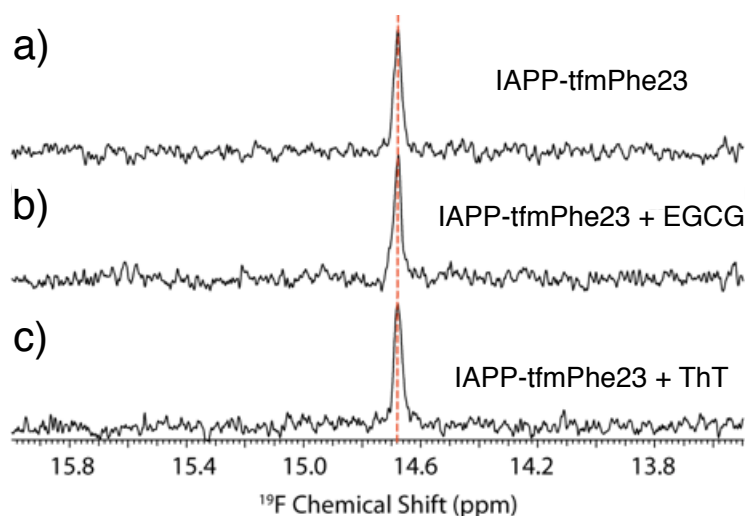
Figure 3.12. EGCG and ThT do not likely interact with monomeric IAPP-tfmPhe23. ^{19}F NMR spectra of (a) IAPP-tfmPhe23 alone, (b) IAPP-tfmPhe23 with 85 μM EGCG, (c) with 100 μM THT (c). Spectra were acquired at pH 7.3, 37°C after 5 minutes of incubation.

As shown in Figure 3.11, competition between EGCG and ThT introduces significant artifacts when the ThT concentration is close to the peptide concentration. This is an important observation, because ThT is commonly used at relatively high concentrations in aggregation studies. However, when the concentration of ThT was lowered to 10 μM, competition between ThT and EGCG was lessened and it was possible to obtain accurate results for both the rate of fiber formation and monomer consumption (Figure 3.13). From the ^{19}F results, it is apparent that

the monomer is almost completely consumed in the presence of EGCG during the lag-time

before the formation of fibers (Figure 3.13). This result is in striking contrast to the kinetics

observed in the absence of EGCG, where fiber formation and monomer consumption occur

virtually simultaneously.
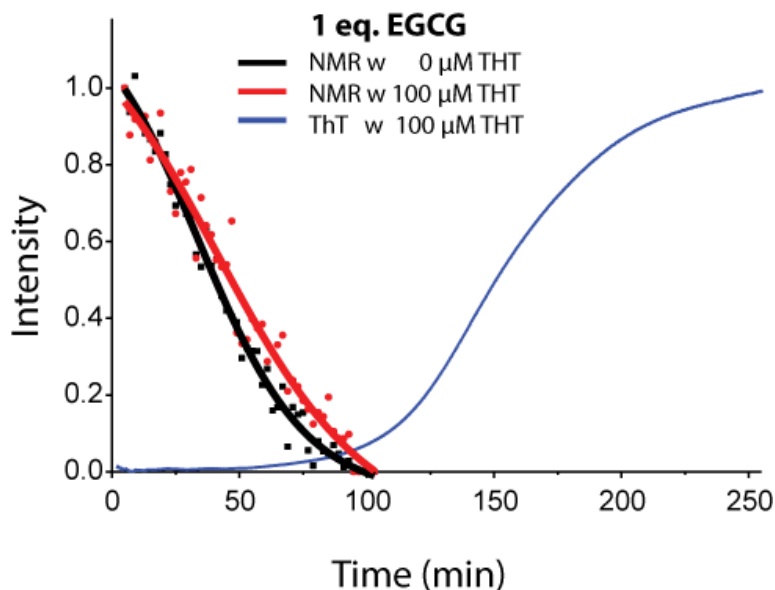
Figure 3.13. Competition between ThT and EGCG is decreased at lower ThT concentration.
Overlay of kinetic traces from ^{19}F NMR (black: 0 μM ThT and red: 10 μM ThT) and ThT fluorescence
(blue: 10 μM) with 1eq. of EGCG. Solid lines represent sigmoidal fits to the ^{19}F data.

The delay between monomer consumption and fiber formation suggests that EGCG

stabilizes the formation of non-fibrillar aggregates that are too large to be detected by NMR (66).

To test this possibility, the reverse reaction was examined by testing the ability of EGCG to

disaggregate IAPP-tfmPhe23 amyloid fibrils using ^{19}F NMR and ThT fluorescence. As Figure

3.14 shows, the addition of a 5-fold molar excess of EGCG after the formation of IAPP amyloid

fibrils caused a significant decrease in ThT fluorescence suggestive of the breakup of fibrils.

However, no signals due to IAPP-tfmPhe23 were observed by ^{19}F NMR after the addition of

EGCG (Figure 3.14), as would be expected if the fibers were completely broken up by EGCG to the monomeric peptide or small oligomers. An examination of the TEM images of supports this conclusion (Figures 3.15). TEM images taken at the end-point of aggregation show small aggregates that are much shorter in length (Figures 3.15 b) than the regular fibers formed by IAPP (Figures 3.15 a) that are similar to those found with Aβ and α-synuclein incubated with EGCG. Instead of stabilizing the monomeric state, EGCG apparently diverts aggregation of IAPP towards large oligomers with a different morphology than the amyloid fiber (Figure 3.16). In this respect, the interaction of EGCG with IAPP is similar to many but not all amyloidogenic proteins (66, 78, 79).
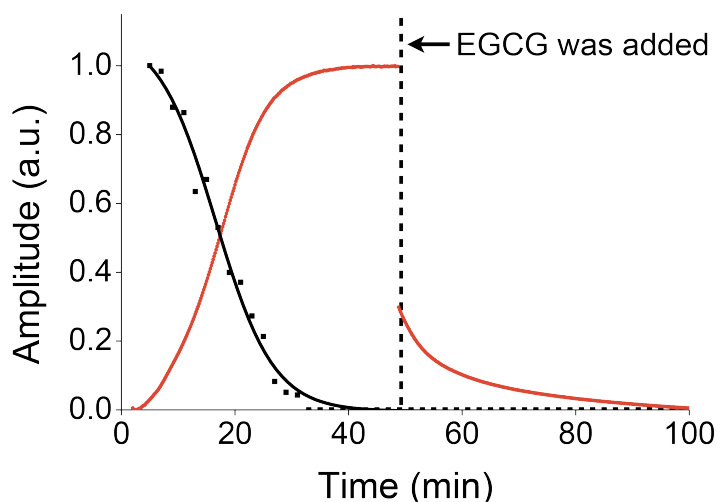
Figure 3.14. Disaggregation of amyloid fibrils due to the addition of EGCG (a) Kinetic traces from ^{19}F NMR (black) and ThT fluorescence (red) measurements at 37 °C. Disaggregation of amyloid fibril formation was complete by the addition of 5 equivalents of EGCG at the time point indicated. Solid lines represent sigmoidal fits to the ^{19}F data.
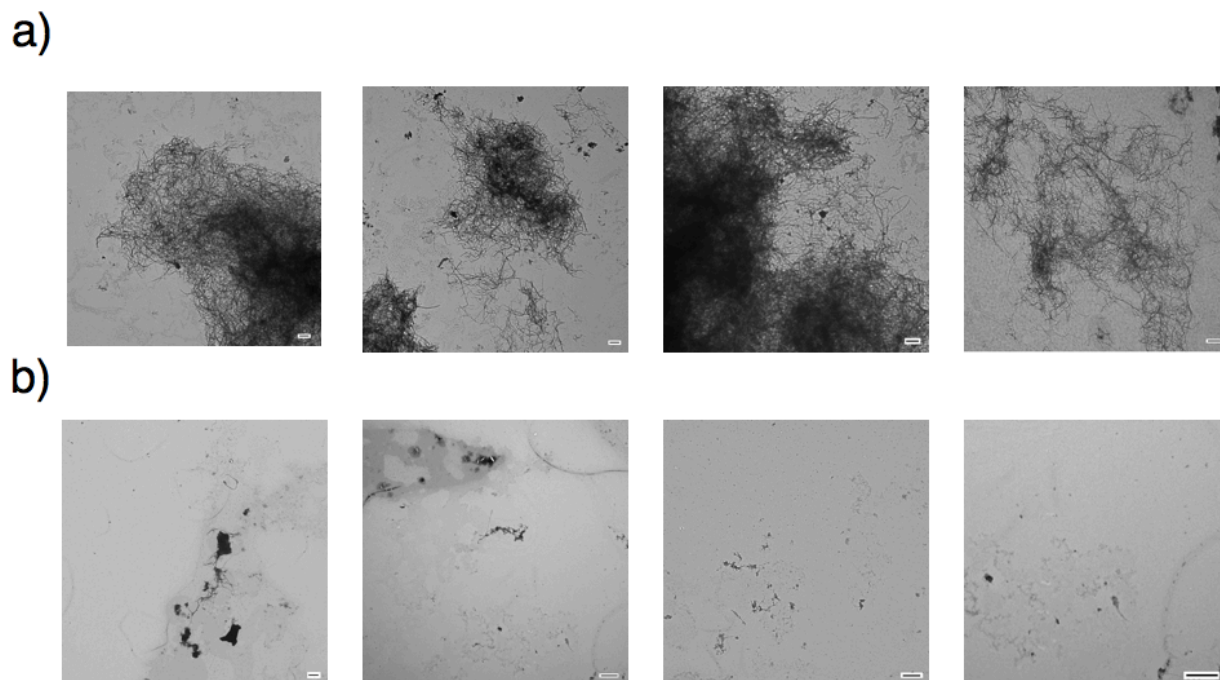
Figure 3.15. EGCG disrupts preformed fibers of IAPP-tfmPhe23. TEM images acquired just before the addition of 5 equivalents of EGCG to preformed fibers of IAPP-tfmPhe23 **(a)** and after complete depletion of THT fluorescence intensity **(b)**. Scale bar represents 500 nm.

● = ThT
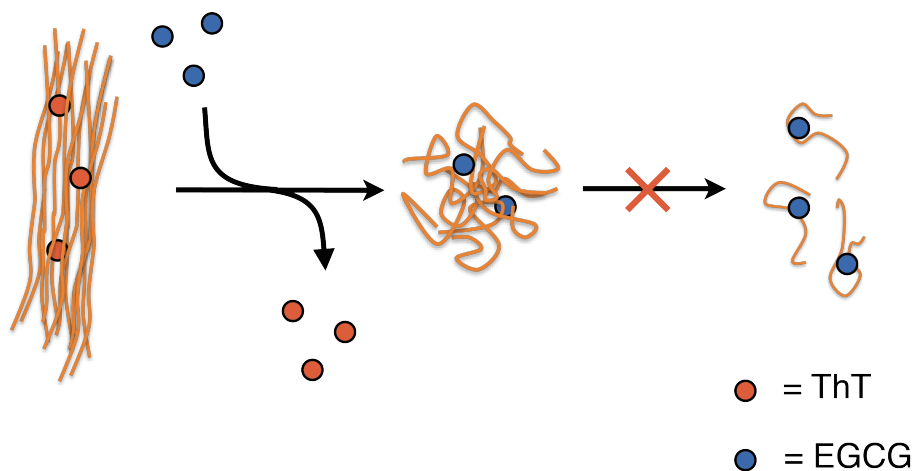
● = EGCG

Figure 3.16. Cartoon schematic of disaggregation of amyloid fiber due to the addition of EGCG. EGCG disaggregates amyloid fiber to incompletely into large oligomers but not fully into monomeric peptides.

3.4. Conclusion

These studies demonstrate the utility of using ^{19}F NMR to follow fibrillogenesis in real-time by observing the rate of monomer consumption. Most of the methods typically used for monitoring the kinetics of aggregation measure the rate of appearance of the final product. By providing an additional independent measurement of the starting material, ^{19}F NMR can help distinguish between alternative pathways of aggregation, a task that is difficult to accomplish by other methods. Since fluorine is not found in most biological systems, there is no competition from background signals, a problem that often afflicts measurements using ^{1}H, ^{13}C, and ^{15}N NMR. The absence of a fluorophore simplifies detection and analysis of amyloid formation by other techniques. Therefore, the use of ^{19}F NMR should be applicable for automated screening of amyloid inhibitors without the false negative and positives that might be present with other techniques.

3.5. References

1. Suzuki, Y., Brender, J. R., Hartman, K., Ramamoorthy, A., and Marsh, E. N. G. (2012) Alternative Pathways of Human Islet Amyloid Polypeptide Aggregation Distinguished by ^{19}F Nuclear Magnetic Resonance-Detected Kinetics of Monomer Consumption, *Biochemistry 51*, 8154 – 8162

2. Chiti, F., and Dobson, C. M. (2006) Protein misfolding, functional amyloid, and human disease, *Annu. Rev. Biochem. 75*, 333-366.

3. Luca, S., Yau, W. M., Leapman, R., and Tycko, R. (2007) Peptide conformation and supramolecular organization in amylin fibrils: constraints from solid-state NMR, *Biochemistry 46*, 13505-13522.

4. Nelson, R., and Eisenberg, D. (2006) Recent atomic models of amyloid fibril structure, *Curr. Opin. Struct. Biol. 16*, 260-265.

5. Tycko, R. (2011) Solid-state NMR studies of amyloid fibril structure, *Annu. Rev. Phys. Chem. 62*, 279-299.

6.   Harrison, R. S., Sharpe, P. C., Singh, Y., and Fairlie, D. P. (2007) Amyloid peptides and proteins in review, *Rev. Physiol. Biochem. Pharmacol. 159*, 1-77.

7.   Ferreira, S. T., Vieira, M. N., and De Felice, F. G. (2007) Soluble protein oligomers as emerging toxins in Alzheimer's and other amyloid diseases, *IUBMB Life 59*, 332-345.

8.   Zraika, S., Hull, R. L., Verchere, C. B., Clark, A., Potter, K. J., Fraser, P. E., Raleigh, D. P., and Kahn, S. E. (2010) Toxic oligomers and islet beta cell death: guilty by association or convicted by circumstantial evidence?, *Diabetologia 53*, 1046-1056.

9.   Haataja, L., Gurlo, T., Huang, C. J., and Butler, P. C. (2008) Islet amyloid in type 2 diabetes, and the toxic oligomer hypothesis, *Endocr. Rev. 29*, 303-316.

10.   Lansbury, P. T., and Lashuel, H. A. (2006) A century-old debate on protein aggregation and neurodegeneration enters the clinic, *Nature 443*, 774-779.

11.   Capone, R., Quiroz, F. G., Prangkio, P., Saluja, I., Sauer, A. M., Bautista, M. R., Turner, R. S., Yang, J., and Mayer, M. (2009) Amyloid-β-induced ion flux in artificial lipid bilayers and neuronal cells: resolving a controversy, *Neurotox. Res. 16*, 1-13.

12.   Chimon, S., Shaibat, M. A., Jones, C. R., Calero, D. C., Aizezi, B., and Ishii, Y. (2007) Evidence of fibril-like β-sheet structures in a neurotoxic amyloid intermediate of Alzheimer's β-amyloid, *Nat. Struct. Mol. Biol. 14*, 1157-1164.

13.   Yoshiike, Y., Minai, R., Matsuo, Y., Chen, Y. R., Kimura, T., and Takashima, A. (2008) Amyloid oligomer conformation in a group of natively folded proteins, *PLoS One 3*, e3235.

14.   Masuda, M., Hasegawa, M., Nonaka, T., Oikawa, T., Yonetani, M., Yamaguchi, Y., Kato, K., Hisanaga, S., and Goedert, M. (2009) Inhibition of α-synuclein fibril assembly by small molecules: analysis using epitope-specific antibodies, *FEBS Lett 583*, 787-791.

15.   Soong, R., Brender, J. R., Macdonald, P. M., and Ramamoorthy, A. (2009) Association of highly compact type II diabetes related islet amyloid polypeptide intermediate species at physiological temperature revealed by diffusion NMR spectroscopy, *J. Am. Chem. Soc. 131*, 7079-7085.

16.   Vaiana, S. M., Ghirlando, R., Yau, W. M., Eaton, W. A., and Hofrichter, J. (2008) Sedimentation studies on human amylin fail to detect low-molecular-weight oligomers, *Biophys. J. 94*, L45-47.

17.   Lee, J., Culyba, E. K., Powers, E. T., and Kelly, J. W. (2011) Amyloid-β forms fibrils by nucleated conformational conversion of oligomers, *Nat. Chem. Biol. 7*, 602-609.

18.   Groenning, M. (2010) Binding mode of Thioflavin T and other molecular probes in the context of amyloid fibrils-current status, *J. Chem. Biol. 3*, 1-18.

19. Marek, P., Mukherjee, S., Zanni, M. T., and Raleigh, D. P. (2010) Residue-specific, real-time characterization of lag-phase species and fibril growth during amyloid formation: a combined fluorescence and IR study of p-cyanophenylalanine analogs of islet amyloid polypeptide, *J. Mol. Biol. 400*, 878-888.

20. Marek, P., Gupta, R., and Raleigh, D. P. (2008) The fluorescent amino acid p-cyanophenylalanine provides an intrinsic probe of amyloid formation, *ChemBioChem 9*, 1372-1374.

21. Mishra, R., Geyer, M., and Winter, R. (2009) NMR spectroscopic investigation of early events in IAPP amyloid fibril formation, *ChemBioChem 10*, 1769-1772.

22. Horvath, I., Weise, C. F., Andersson, E. K., Chorell, E., Sellstedt, M., Bengtsson, C., Olofsson, A., Hultgren, S. J., Chapman, M., Wolf-Watz, M., Almqvist, F., and Wittung-Stafshede, P. (2012) Mechanisms of protein oligomerization: inhibitor of functional amyloids templates α-synuclein fibrillation, *J. Am. Chem. Soc. 134*, 3439-3444.

23. Shim, S. H., Gupta, R., Ling, Y. L., Strasfeld, D. B., Raleigh, D. P., and Zanni, M. T. (2009) Two-dimensional IR spectroscopy and isotope labeling defines the pathway of amyloid formation with residue-specific resolution, *Proc. Natl. Acad. Sci. U.S.A. 106*, 6614-6619.

24. Wang, L., Middleton, C. T., Singh, S., Reddy, A. S., Woys, A. M., Strasfeld, D. B., Marek, P., Raleigh, D. P., de Pablo, J. J., Zanni, M. T., and Skinner, J. L. (2011) 2DIR spectroscopy of human amylin fibrils reflects stable β-sheet structure, *J. Am. Chem. Soc. 133*, 16062-16071.

25. Larson, J. L., Ko, E., and Miranker, A. D. (2000) Direct measurement of islet amyloid polypeptide fibrillogenesis by mass spectrometry, *Protein Sci. 9*, 427-431.

26. Cole, H. L., Kalapothakis, J. M., Bennett, G., Barran, P. E., and Macphee, C. E. (2010) Characterizing early aggregates formed by an amyloidogenic peptide by mass spectrometry, *Angew. Chem. Int. Ed. 49*, 9448-9451.

27. Maezawa, I., Hong, H. S., Liu, R., Wu, C. Y., Cheng, R. H., Kung, M. P., Kung, H. F., Lam, K. S., Oddo, S., Laferla, F. M., and Jin, L. W. (2008) Congo red and thioflavin-T analogs detect Aβ oligomers, *J. Neurochem. 104*, 457-468.

28. Cobb, S. L., and Murphy, C. D. (2009) ^{19}F NMR applications in chemical biology, *J. Fluorine Chem. 130*, 132-143.

29. Kitevski-LeBlanc, J. L., and Prosser, R. S. (2012) Current applications of ^{19}F NMR to studies of protein structure and dynamics, *Prog. Nucl. Magn. Reson. Spectrosc. 62*, 1-33.

30. Bann, J. G., Pinkner, J., Hultgren, S. J., and Frieden, C. (2002) Real-time and equilibrium ^{19}F-NMR studies reveal the role of domain-domain interactions in the folding of the chaperone PapD, *Proc. Natl. Acad. Sci. U.S.A. 99*, 709-714.

31. Li, H., and Frieden, C. (2007) Observation of sequential steps in the folding of intestinal fatty acid binding protein using a slow folding mutant and ^{19}F NMR, *Proc. Natl. Acad. Sci. U.S.A. 104*, 11993-11998.

32. Li, H., and Frieden, C. (2007) Comparison of C40/82A and P27A C40/82A barstar mutants using ^{19}F NMR, *Biochemistry 46*, 4337-4347.

33. Schlesinger, A. P., Wang, Y., Tadeo, X., Millet, O., and Pielak, G. J. (2011) Macromolecular crowding fails to fold a globular protein in cells, *J. Am. Chem. Soc. 133*, 8082-8085.

34. Anderluh, G., Razpotnik, A., Podlesek, Z., Macek, P., Separovic, F., and Norton, R. S. (2005) Interaction of the eukaryotic pore-forming cytolysin equinatoxin II with model membranes: ^{19}F NMR studies, *J. Mol. Biol. 347*, 27-39.

35. Glaser, R. W., Sachse, C., Durr, U. H., Wadhwani, P., and Ulrich, A. S. (2004) Orientation of the antimicrobial peptide PGLa in lipid membranes determined from ^{19}F-NMR dipolar couplings of 4-CF$_3$-phenylglycine labels, *J. Magn. Reson. 168*, 153-163.

36. Afonin, S., Grage, S. L., Ieronimo, M., Wadhwani, P., and Ulrich, A. S. (2008) Temperature-dependent transmembrane insertion of the amphiphilic peptide PGLa in lipid bilayers observed by solid state ^{19}F NMR spectroscopy, *J. Am. Chem. Soc. 130*, 16512-16514.

37. Suzuki, Y., Buer, B. C., Al-Hashimi, H. M., and Marsh, E. N. G. (2011) Using Fluorine Nuclear Magnetic Resonance To Probe Changes in the Structure and Dynamics of Membrane-Active Peptides Interacting with Lipid Bilayers, *Biochemistry 50*, 5979-5987.

38. Buer, B. C., Chugh, J., Al-Hashimi, H. M., and Marsh, E. N. G. (2010) Using fluorine nuclear magnetic resonance to probe the interaction of membrane-active peptides with the lipid bilayer, *Biochemistry 49*, 5760-5765.

39. Li, C., Wang, G. F., Wang, Y., Creager-Allen, R., Lutz, E. A., Scronce, H., Slade, K. M., Ruf, R. A., Mehl, R. A., and Pielak, G. J. (2010) Protein ^{19}F NMR in Escherichia coli, *J. Am. Chem. Soc. 132*, 321-327.

40. Jackson, J. C., Hammill, J. T., and Mehl, R. A. (2007) Site-specific incorporation of a ^{19}F-amino acid into proteins as an NMR probe for characterizing protein structure and reactivity, *J. Am. Chem. Soc. 129*, 1160-1166.

41. Shi, P., Wang, H., Xi, Z., Shi, C., Xiong, Y., and Tian, C. (2011) Site-specific ^{19}F NMR chemical shift and side chain relaxation analysis of a membrane protein labeled with an unnatural amino acid, *Protein Sci. 20*, 224-228.

42. Liu, J. J., Horst, R., Katritch, V., Stevens, R. C., and Wuthrich, K. (2012) Biased signaling pathways in β2-adrenergic receptor characterized by ^{19}F-NMR, *Science 335*, 1106-1110.

43.   Li, C., Lutz, E. A., Slade, K. M., Ruf, R. A., Wang, G. F., and Pielak, G. J. (2009) ^{19}F NMR studies of α-synuclein conformation and fibrillation, *Biochemistry 48*, 8578-8584.

44.   Maisch, D., Wadhwani, P., Afonin, S., Bottcher, C., Koksch, B., and Ulrich, A. S. (2009) Chemical labeling strategy with (R)- and (S)-trifluoromethylalanine for solid state ^{19}F NMR analysis of peptaibols in membranes, *J. Am. Chem. Soc. 131*, 15596-15597.

45.   Westermark, P., Andersson, A., and Westermark, G. T. (2011) Islet amyloid polypeptide, islet amyloid, and diabetes mellitus, *Physiol. Rev. 91*, 795-826.

46.   Hoppener, J. W., Ahren, B., and Lips, C. J. (2000) Islet amyloid and type 2 diabetes mellitus, *N. Engl. J. Med. 343*, 411-419.

47.   Brender, J. R., Salamekh, S., and Ramamoorthy, A. (2012) Membrane disruption and early events in the aggregation of the diabetes related peptide IAPP from a molecular perspective, *Acc. Chem. Res. 45*, 454-462.

48.   Page, K., Hood, C. A., Patel, H., Fuentes, G., Menakuru, M., and Park, J. H. (2007) Fast Fmoc synthesis of hAmylin1-37 with pseudoproline assisted on-resin disulfide formation, *J. Pept. Sci. 13*, 833-838.

49.   Pace, C. N., Vajdos, F., Fee, L., Grimsley, G., and Gray, T. (1995) How to measure and predict the molar absorption coefficient of a protein, *Protein Sci. 4*, 2411-2423.

50.   Brender, J. R., Hartman, K., Nanga, R. P., Popovych, N., de la Salud Bea, R., Vivekanandan, S., Marsh, E. N. G, and Ramamoorthy, A. (2010) Role of zinc in human islet amyloid polypeptide aggregation, *J. Am. Chem. Soc. 132*, 8973-8983.

51.   Yonemoto, I. T., Kroon, G. J., Dyson, H. J., Balch, W. E., and Kelly, J. W. (2008) Amylin proprotein processing generates progressively more amyloidogenic peptides that initially sample the helical state, *Biochemistry 47*, 9900-9910.

52.   Wiltzius, J. J., Sievers, S. A., Sawaya, M. R., Cascio, D., Popov, D., Riekel, C., and Eisenberg, D. (2008) Atomic structure of the cross-β spine of islet amyloid polypeptide (amylin), *Protein Sci. 17*, 1467-1474.

53.   Wiltzius, J. J., Sievers, S. A., Sawaya, M. R., and Eisenberg, D. (2009) Atomic structures of IAPP (amylin) fusions suggest a mechanism for fibrillation and the role of insulin in the process, *Protein Sci. 18*, 1521-1530.

54.   Linse, B., and Linse, S. (2011) Monte Carlo simulations of protein amyloid formation reveal origin of sigmoidal aggregation kinetics, *Mol. BioSyst. 7*, 2296-2303.

55.   Kodaka, M. (2004) Requirements for generating sigmoidal time-course aggregation in nucleation-dependent polymerization model, *Biophys. Chem. 107*, 243-253.

56.   Jarrett, J. T., and Lansbury, P. T., Jr. (1993) Seeding "one-dimensional crystallization" of amyloid: a pathogenic mechanism in Alzheimer's disease and scrapie?, *Cell 73*, 1055-1058.

57.   Kayed, R., Bernhagen, J., Greenfield, N., Sweimeh, K., Brunner, H., Voelter, W., and Kapurniotu, A. (1999) Conformational transitions of islet amyloid polypeptide (IAPP) in amyloid formation in vitro, *J. Mol. Biol. 287*, 781-796.

58.   Schulz, D. M., Ihling, C., Clore, G. M., and Sinz, A. (2004) Mapping the topology and determination of a low-resolution three-dimensional structure of the calmodulin-melittin complex by chemical cross-linking and high-resolution FTICRMS: direct demonstration of multiple binding modes, *Biochemistry 43*, 4703-4715.

59.   Powers, E. T., and Powers, D. L. (2006) The kinetics of nucleated polymerizations at high concentrations: amyloid fibril formation near and above the "supercritical concentration", *Biophys. J. 91*, 122-132.

60.   Giehm, L., and Otzen, D. E. (2010) Strategies to increase the reproducibility of protein fibrillization in plate reader assays, *Anal. Biochem. 400*, 270-281.

61.   Jean, L., Lee, C. F., Lee, C., Shaw, M., and Vaux, D. J. (2010) Competing discrete interfacial effects are critical for amyloidogenesis, *FASEB J. 24*, 309-317.

62.   Pronchik, J., He, X., Giurleo, J. T., and Talaga, D. S. (2010) In vitro formation of amyloid from α-synuclein is dominated by reactions at hydrophobic interfaces, *J. Am. Chem. Soc. 132*, 9797-9803.

63.   Kirkitadze, M. D., Condron, M. M., and Teplow, D. B. (2001) Identification and characterization of key kinetic intermediates in amyloid β-protein fibrillogenesis, *J. Mol. Biol. 312*, 1103-1119.

64.   Ding, H., Wong, P. T., Lee, E. L., Gafni, A., and Steel, D. G. (2009) Determination of the oligomer size of amyloidogenic protein β-amyloid$_{1-40}$ by single-molecule spectroscopy, *Biophys. J. 97*, 912-921.

65.   Lambert, M. P., Barlow, A. K., Chromy, B. A., Edwards, C., Freed, R., Liosatos, M., Morgan, T. E., Rozovsky, I., Trommer, B., Viola, K. L., Wals, P., Zhang, C., Finch, C. E., Krafft, G. A., and Klein, W. L. (1998) Diffusible, nonfibrillar ligands derived from Abeta$_{1-42}$ are potent central nervous system neurotoxins, *Proc. Natl. Acad. Sci. U.S.A. 95*, 6448-6453.

66.   Ehrnhoefer, D. E., Bieschke, J., Boeddrich, A., Herbst, M., Masino, L., Lurz, R., Engemann, S., Pastore, A., and Wanker, E. E. (2008) EGCG redirects amyloidogenic polypeptides into unstructured, off-pathway oligomers, *Nat. Struct. Mol. Biol. 15*, 558-566.

67.   Popovych, N., Brender, J. R., Soong, R., Vivekanandan, S., Hartman, K., Basrur, V., Macdonald, P. M., and Ramamoorthy, A. (2012) Site specific interaction of the

polyphenol EGCG with the SEVI amyloid precursor peptide PAP(248-286), *J. Phys. Chem. B 116*, 3650-3658.

68.   Meng, F., Abedini, A., Plesner, A., Verchere, C. B., and Raleigh, D. P. (2010) The flavanol (-)-epigallocatechin 3-gallate inhibits amyloid formation by islet amyloid polypeptide, disaggregates amyloid fibrils, and protects cultured cells against IAPP-induced toxicity, *Biochemistry 49*, 8127-8133.

69.   Ferreira, N., Cardoso, I., Domingues, M. R., Vitorino, R., Bastos, M., Bai, G., Saraiva, M. J., and Almeida, M. R. (2009) Binding of epigallocatechin-3-gallate to transthyretin modulates its amyloidogenicity, *FEBS Lett. 583*, 3569-3576.

70.   Hauber, I., Hohenberg, H., Holstermann, B., Hunstein, W., and Hauber, J. (2009) The main green tea polyphenol epigallocatechin-3-gallate counteracts semen-mediated enhancement of HIV infection, *Proc. Natl. Acad. Sci. U.S.A. 106*, 9033-9038.

71.   Huang, R., Vivekanandan, S., Brender, J. R., Abe, Y., Naito, A., and Ramamoorthy, A. (2012) NMR characterization of monomeric and oligomeric conformations of human calcitonin and its interaction with EGCG, *J. Mol. Biol. 416*, 108-120.

72.   Hudson, S. A., Ecroyd, H., Kee, T. W., and Carver, J. A. (2009) The thioflavin T fluorescence assay for amyloid fibril detection can be biased by the presence of exogenous compounds, *FEBS J. 276*, 5960-5972.

73.   Chandrashekaran, I. R., Adda, C. G., Macraild, C. A., Anders, R. F., and Norton, R. S. (2011) EGCG disaggregates amyloid-like fibrils formed by Plasmodium falciparum merozoite surface protein 2, *Arch. Biochem. Biophys. 513*, 153-157.

74.   Liu, K. N., Wang, H. Y., Chen, C. Y., and Wang, S. S. (2010) L-Arginine reduces thioflavin T fluorescence but not fibrillation of bovine serum albumin, *Amino Acids 39*, 821-829.

75.   Meng, F., Marek, P., Potter, K. J., Verchere, C. B., and Raleigh, D. P. (2008) Rifampicin does not prevent amyloid fibril formation by human islet amyloid polypeptide but does inhibit fibril thioflavin-T interactions: implications for mechanistic studies of β-cell death, *Biochemistry 47*, 6016-6024.

76.   Hudson, S. A., Ecroyd, H., Dehle, F. C., Musgrave, I. F., and Carver, J. A. (2009) (-)-epigallocatechin-3-gallate (EGCG) maintains kappa-casein in its pre-fibrillar state without redirecting its aggregation pathway, *J. Mol. Biol. 392*, 689-700.

77.   Miyata, M., Sato, T., Kugimiya, M., Sho, M., Nakamura, T., Ikemizu, S., Chirifu, M., Mizuguchi, M., Nabeshima, Y., Suwa, Y., Morioka, H., Arimori, T., Suico, M. A., Shuto, T., Sako, Y., Momohara, M., Koga, T., Morino-Koga, S., Yamagata, Y., and Kai, H. (2010) The crystal structure of the green tea polyphenol (-)-epigallocatechin gallate-transthyretin complex reveals a novel binding site distinct from the thyroxine binding site, *Biochemistry 49*, 6104-6114.

78. Bieschke, J., Russ, J., Friedrich, R. P., Ehrnhoefer, D. E., Wobst, H., Neugebauer, K., and Wanker, E. E. (2010) EGCG remodels mature α-synuclein and amyloid-β fibrils and reduces cellular toxicity, *Proc. Natl. Acad. Sci. U.S.A. 107*, 7710-7715.

79. He, J., Xing, Y. F., Huang, B., Zhang, Y. Z., and Zeng, C. M. (2009) Tea catechins induce the conversion of preformed lysozyme amyloid fibrils to amorphous aggregates, *J. Agric. Food. Chem. 57*, 11391-11396.

Chapter 4

Resolution of Oligomeric Species during the Aggregation of Aβ$_{1-40}$ Using ^{19}F NMR

4.1. Introduction

The work described in this chapter is currently in preparation for publication. The co-authors were very helpful in conducting this research and analyzing the results. Numerous suggestions and guidance on experiments came from Dr. Jeffrey R. Brender and Prof. Ayyalusamy Ramamoorthy. I also would like to thank Dr. Janarthanan Krishnamoorthy for expertise for NMR experiments, Molly Soper and Prof. Brandon Ruotolo for expertise and analysis of the ESI-IMMS, and Dr. Yunlong Zhou and Prof. Nicholas Kotov for expertise and use of the AFM microscopy.

The accumulation of misfolded proteins is a common pathological feature of a number of human disorders, including neurodegenerative disorders such as Alzheimer's disease and Parkinson's disease and several metabolic diseases such as type II diabetes. Under pathological conditions, the soluble precursor form of these proteins is triggered to self-assemble into amyloid fibers (Figure 1.8 and 1.9) (1). These are long, linear and often twisted structures a few nanometers in diameter and many nanometers in length (2). The morphologies of amyloid fibers show a characteristic cross-β sheet X-ray diffraction pattern indicating a cross β-sheet

conformation of β-sheets running perpendicular to the fibril axis (2, 3).

In Alzheimer's disease, the amyloid plaques are largely composed of the Aβ peptide. Aβ peptides are derived from proteolytic cleavage of the amyloid precursor protein (APP) to produce peptides varying from 36-43 amino acids in length, of which $A\beta_{1-40}$ is the most common (4). Because pathogenic mutations in the APP lead to early onset versions of Alzheimer's diseases and aggregated forms of $A\beta_{1-40}$ are toxic *in vivo* and also to some extent in mouse models, Aβ plaque formation has been proposed to be the ultimate upstream cause of Alzheimer's disease (amyloid cascade hypothesis) (5-7). The process of amyloid formation has been repeatedly shown for multiple amyloidogenic proteins to disrupt the regular function of tissue. Unfortunately, how this occurs has been obscured by our lack of knowledge about the aggregation process itself (4). In particular, identifying potentially toxic species in Aβ has been difficult because of the heterogeneity of the samples and inter-conversion among species (8). NMR is an attractive method for following the reaction in real-time because of the strong relationship between chemical shift and peptide structure. However, applications of real-time NMR to amyloid formation have been limited (9, 10). This is largely due to the complexities of one dimensional ^1H spectra and the difficulties in obtaining multidimensional spectra within the aggregation time-frame.

^{19}F NMR is an attractive alternative because of the excellent sensitivity of the ^{19}F nucleus to small changes in conformation. The high sensitivity of ^{19}F chemical shift to the chemical environment enables the use of simple 1D spectra to detect the changes of protein conformations (11-19). In addition, fluorine is extremely rare in biological systems so that there is no competition from background signals, a problem that often afflicts measurements of the most commonly used nuclei including ^1H, ^{13}C, and ^{15}N. This advantage also allows difficult studies

including those involving multiple protein complexes as well as *in vivo* applications, where signals from protein of interest are often attenuated in other NMR techniques.

In chapter 3, I used this approach to study the oligomerization of IAPP, an amyloidogenic polypeptide implicated in β-cell death in type II diabetes (20). ^{19}F NMR showed aggregation of IAPP is essentially an all-or-nothing event; monomeric IAPP is rapidly converted to fibrillar IAPP without the buildup of intermediates detected by ^{19}F NMR. This finding is in agreement with other studies of IAPP aggregation, which show small oligomers of less than 100 kDa do not build up to an appreciable extent during aggregation (21-23).

By contrast, many off- and on-pathway oligomeric intermediates of Aβ have been isolated both *in vitro* and *in situ* from tissue samples of Alzheimer's patients. Characterization of these oligomeric species is particularly important as a current hypothesis holds that small to intermediate size (~5−6 nm in diameter) oligomers may be responsible for much of the toxicity of amyloid proteins (24, 25). In this chapter, I have demonstrated ^{19}F NMR real-time measurements to investigate the formation of small oligomeric intermediates during the formation of amyloid fibers from $A\beta_{1-40}$.

4.2. Experimental Procedures

4.2.1. Synthesis of Fmoc-L-trifluoromethionine

The synthesis of Fmoc-L-homocysteine (Fmoc-hCys-OH) was based on a modified version of the procedure of Jiang et al (26). Bis-L-homocysteine was purchased from Toronto Research Chemicals Inc. A dioxane solution of Fmoc *N*-hydroxysuccinimide ester (Fmoc-Osu) was added dropwise with vigorous stirring into L-homocysteine in 10% w/v $NaHCO_3$ (aq) overnight. After adjustment of the pH to 4 using citric acid, dioxane was removed under reduced

pressure followed by extraction with ethyl acetate (3x). The ethyl acetate layers were combined, dried over anhydrous sodium sulfate, and evaporated under reduced pressure to yield the product. It was then dissolved into a Dimethylformamide (DMF)/H_2O solution followed by the addition of 1.5 eq. of tris(2-carboxyethyl)phosphine (TCEP), and the reaction mixture stirred overnight. DMF was then removed under reduced pressure and the aqueous solution was extracted with ethyl acetate (3x) to yield pure product. The overall yield for the two steps was 60 % without any purification step. The analytical data for Fmoc-hCys-OH matched as previously reported (26, 27).

Fmoc-L-trifluoromethionine (Fmoc-tfMet-OH) was then synthesized from Fmoc-hCys-OH using the procedure developed by Togni and his colleagues (28). Togni reagent (1-Trifluoromethyl-3,3-dimethyl-1,2-benziodoxole) was purchased from TCI America. Briefly, a solution of Fmoc-L-homocysteine in methanol was cooled to -78 °C, and then 1 eq of Togni reagent was added dropwise with vigorous stirring. After completion of reaction overnight, the reaction mixture was dried under vacuo and purified by flash chromatography to yield desired product. The analytical data for Fmoc-tfMet-OH matched as previously reported (29).

4.2.2. Peptide Preparation

$A\beta_{1-40}$-tfMet35 peptide was synthesized manually by solid-phase Fmoc-based chemistry using a dimethoxybenzyl (Dmb) dipeptide, Fmoc-Val-(Dmb)Gly-OH (at position 36 and 37), to disrupt aggregation during synthesis. Fmoc-tfMet-OH was substituted for Met at position 35. The peptide was cleaved from the resin using 92.5 % TFA, 2.5 % H_2O, 2.5 % ethanedithiol, and 2.5 % anisole. The crude peptide was dissolved in 20 % acetic acid (v/v) and the purified by reverse-phase HPLC using a Waters semi-preparative C18 column equilibrated in 0.045% HCl.

The peptides were eluted with a linear gradient of 0% to 80% acetonitrile at a flow rate of 10 ml/min. The identity of the target fraction was confirmed using MALDI-MS, which gave corresponding to the correct mass of 4384.

4.2.3. Sample Preparation

To remove preformed aggregates, the purified peptide was dissolved in 2 % ammonium hydroxide followed by removal of the solvent by lyophilization. The lyophilized peptide was first dissolved in 1 mM NaOH and sonicated for 15 min. The peptide solution was then buffered into 20 mM sodium phosphate (pH 7.4) and 10% D_2O to final peptide concentrations. The sample solution was then passed though a 0.22 μm filter immediately before the start of each experiment.

4.2.4. ^{19}F NMR Spectroscopy

All ^{19}F NMR experiments were performed using a Varian VNMRS 500 MHz NMR spectrometer equipped with a double-resonance ^{1}H ^{19}F probe. 5 mm Shigemi NMR tubes (Shigemi Inc, BMS-005V) were used for this study. A series of ^{19}F spectra were recorded without spinning immediately after filtration of sample at 37 °C as described above. For time course experiments, each ^{19}F spectrum was obtained from 512 scans with a 1.0 s recycle delay between each transient. To measure solvent isotope-induced changes in chemical shifts, samples were first prepared with 10% D_2O in PBS (pH 7.4) and measured as mentioned above. The samples were then diluted with D_2O to prepare 70% D_2O samples. ^{19}F chemical shifts are referenced to 100 μM trifluoroethanol (TFE) at 0 ppm, and ^{19}F signal intensity was normalized to TFE. A line broadening of 2.0 Hz was used to process the final spectra. Origin 8.5 and

Mestrenova were used for plotting the data.

The hydrodynamic radius of the initial conformation of the 46 μM sample was approximated by the measuring the diffusion constant of the corresponding resonance by diffusion ordered spectroscopy (DOSY). ^{19}F DOSY experiments of the ^{19}F nucleus were carried out using the gradient-compensated stimulated echo (GCSTE) sequence with squared gradient pulses of constant duration (2 ms) and a variable gradient amplitude along the longitudinal axis (30). Other experimental parameters include a 90° pulse width of 9.5 μs, a gradient stabilization delay of 0.5 ms, a stimulated-echo delay of 50 ms, a recycle delay of 0.5 s, and a spectral width of 25.51 kHz. Radio frequency pulses were phase cycled to remove unwanted echoes. 2048 transients were collected for each gradient and 10 gradients were used for each sample for a total experimental time of approximately 6 hours. The stability of the sample was confirmed by comparison of the ^{19}F spectra at the beginning and end of the DOSY experiments. All spectra were processed with 3 Hz exponential line broadening prior to Fourier transformation. The diffusion coefficients were determined from the slope of a log plot of the intensity as a function of gradient strength using the Stejskal-Tanner equation (31). The hydrodynamic radius was then calculated from the diffusion coefficient using the Einstein-Stokes relation and the viscosity of water at 25 $^{\circ}$C.

4.2.5. Circular Dichroism

CD measurements were performed with an Aviv 62DS spectropolarimeter using a 0.1 cm pathlength cell. Samples were prepared as described above for the NMR samples. Molar CD per residue values were calculated using $\varepsilon = \theta_{obsd}/(3298lcn)$ where θ_{obsd} is the ellipticity measured in

millidegrees, c is the molar concentration, l is the cell path length in centimeters, and n is the number of residues in the peptide.

4.2.6. Atomic Force Microscopy

Aliquots were directly taken from sample prepared as described above on SiO_2 substrates at the time-points indicated. This sample was diluted five times before use. Samples were imaged using a Nanoscope III (Digital Instruments/Veeco Metrology Group).

4.2.7. Electrospray Ionization Ion Mobility Mass Spectrometry

Protein ions were generated using a nESI source and optimized to allow transmission of noncovalent protein complexes unless stated otherwise. Nanoflow electrospray capillaries were prepared in-house as previously described (32). To generate protein complex ions, an aliquot of the sample (*ca*. 5 μL) was sprayed from the nESI emitter using capillary voltages ranging from $1.4 - 1.6$ kV, with the source operating in positive ion mode and the sample cone operated at 20 V. The mass spectra were acquired with the following settings and tuned to avoid ion activation and preserve non-covalent protein–ligand complexes. The bias voltage was 40 V, with backing pressure at 5.39 mBar and ToF pressure at 9.74×10^{-7} mBar. The traveling-wave IM separator was operated at a pressure of approximately 3.5 mbar of nitrogen and helium. Mass spectra were calibrated externally using a solution of cesium iodide (100 mg/mL) and analyzed using Masslynx 4.1 and Driftscope 2.0 software (Waters). Samples were prepared by mixing an aliquot of the NMR sample with 100 mM ammonium acetate at pH 7.0 at 1:1 ratio followed by filtration through a 100 or 30 kDa membrane as described.

4.3. Results

4.3.1. Design and Synthesis of Aβ$_{1-40}$-tfMet35

To study the process of Aβ aggregation using ^{19}F NMR, a ^{19}F-labeled Aβ$_{1-40}$ peptide (Aβ$_{1-40}$-tfMet35) was synthesized in which Met-35 was replaced by tfMet **7** (Figure 4.1). Met-35 was chosen as a probe site because a fluorine nucleus on the flexible side-chain of Met undergoes additional motional averaging compared to other more rigid, fluorinated amino acids like tfmPhe **2**. The additional flexibility of the tfMet side-chain is important as the motional averaging contributes to a smaller effective rotational correlation time, which increases the probability of detecting larger aggregates.

a)

b)

DAEFRHDSGYEVHHQKLVFFAEDVGSNKGAIIGL(tfMet)VGGVV-OH
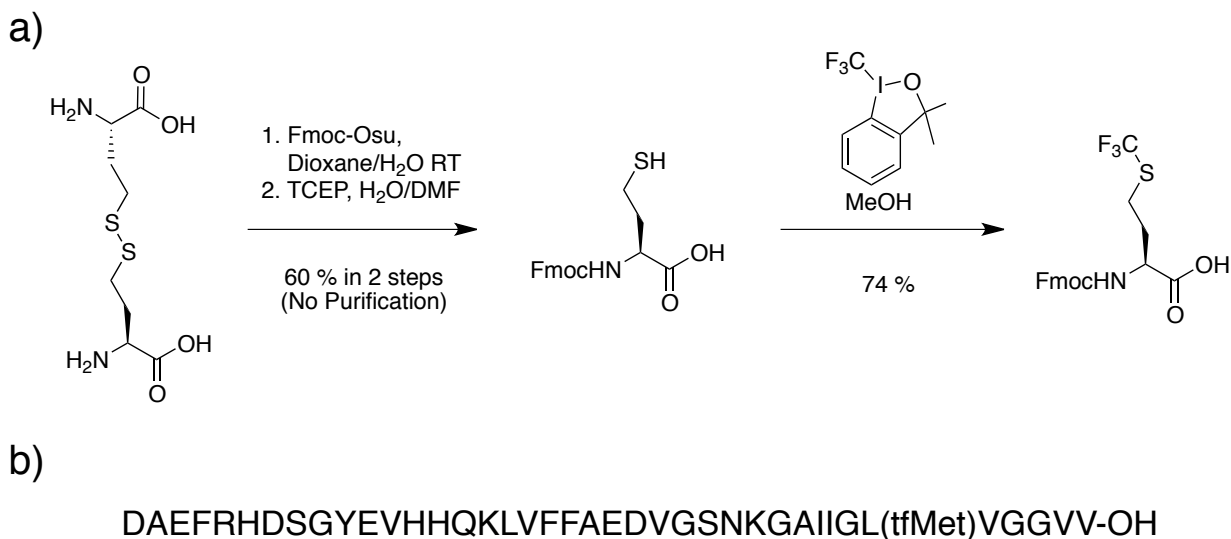
Figure 4.1. Preparation of Aβ$_{1-40}$-tfMet35 (a) Synthesis of Fmoc-tfMet-OH. (b) Sequence of Aβ$_{1-40}$-tfMet35. tfMet replaces Met35 in Fmoc-based peptide synthesis.

To construct the Aβ$_{1-40}$-tfMet35 peptide, Fmoc-tfM-OH was first synthesized with the use of Togni reagent for trifluoromethylation as shown in Figure 4.1 (28). This optimized synthetic route improves yields by reducing the number of synthetic steps from 5 to 3 eliminating the need

for racemization. $A\beta_{1-40}$-tfMet35 peptide was then synthesized using an optimized Fmoc procedure with Fmoc-tfMet-OH. The ^{19}F chemical shifts and line-widths of the trifluoromethyl groups should change significantly as the peptide changes either its secondary structure or oligomerization state, as has been observed for other fluorinated peptides and proteins (20). In particular, if oligomeric intermediates on the amyloid-forming pathway accumulate to an appreciable extent they should be detectable by NMR, provided they are not so large that their line-widths are broadened excessively, as is the case for amyloid fibers (9).

4.3.2. $A\beta_{1-40}$-tfMet35 reversibly forms oligomers immediately after preparation at high concentration

Recent studies have shown that the pathway of $A\beta_{1-40}$ amyloid formation is strongly dependent on the initial concentration (33, 34). To examine these differences, two samples of $A\beta_{1-40}$-tfMet35 were prepared at concentrations of 46 μM and 182 μM and their aggregation followed in parallel. The ^{19}F NMR spectra of both samples immediately after preparation are shown in Figure 4.2. Both spectra show a single intense resonance at 35.85 ppm (Figure 4.2a, b), which DOSY experiments show corresponds to a species with a hydrodynamic radius of 1.28 nm (Figure 4.2c). This value is nearly identical to previous values obtained for non-aggregated $A\beta_{1-40}$ in buffer (1.29 nm) and in NaOH (1.32 nm) (35) and similar to single molecule measurements of monomeric $A\beta_{1-40}$ (0.9 nm) (36). The main resonance in the ^{19}F spectra at the initial time point therefore is very likely to correspond to the monomeric peptide in both samples.
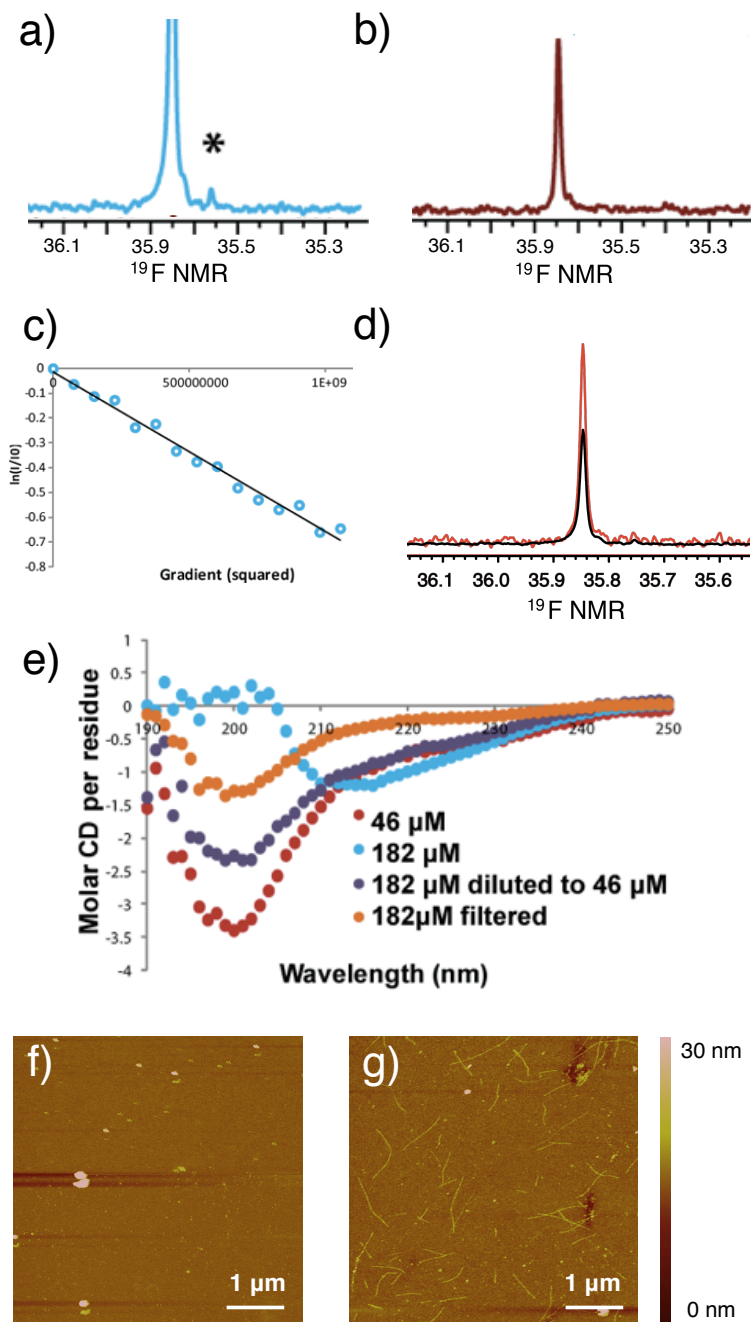
Figure 4.2. Characterization of Aβ$_{1-40}$-tfMet35 immediately after preparation. (a, b) ^{19}F NMR spectra of (a) 182 μM and (b) 46 μM samples of Aβ$_{1-40}$-tfMet35. A small additional peak not present in the low concentration sample is marked with an asterisk. (c) ^{19}F DOSY experiment of 46 μM immediately after preparation. (d) ^{19}F spectra following dilution from 182 (black) to 45 μM (red) ^{19}F signal intensities are normalized to an internal TFE standard. (e) CD spectra of 182 μM and 46 μM Aβ$_{1-40}$-tfMet35 at the initial time-point and the influence of filtration and dilution to 46 μM on the 182 μM sample. (f, g) AFM images of 46 μM (f) and 182 μM (g) samples of Aβ$_{1-40}$-tfMet35 on SiO$_2$ substrates at the initial time-point.

However, differences in the two samples are apparent even at this initial time point. Rod-like short protofibers can be seen at the initial time-point in atomic force microscopy (AFM) images of the high concentration sample (Figure 4.2g) while they are conspicuously absent in the low concentration sample (Figure 4.2f). Consistent with this finding, the high concentration sample shows a strong β-sheet component in the CD spectrum, as expected of protofibers (Figure 4.2e). However this signal is absent in the low concentration sample. The change in the CD spectra after filtration through 100 KDa cutoff membrane in the high concentration sample confirmed the β-sheet component arises from larger oligomers (Figure 4.2e). The presence of large oligomeric species at the initial time point can also be indirectly inferred from the ^{19}F spectra (Figure 4.2d). The intensity of the 182 μM sample is 44% less than the 46 μM sample after normalization for concentration, consistent with the formation of large, NMR-invisible protofibers which give rise to the β-sheet CD spectra and are observed in the AFM images. Perhaps surprisingly in light of the large thermodynamic favorability of β-sheet formation in amyloid fibers (36), oligomer formation of this type appears to be reversible. The CD spectrum after dilution from 182 μM to 46 μM reverts to a largely random coil conformation (Figure 4.2e) and the normalized intensity increases upon dilution (Figure 4.2d). Similarly, a small additional peak at 35.75 ppm found in the 182 μM sample but not in the 46 μM sample disappears upon dilution.

### 4.3.3. Early time evolution of Aβ$_{1-40}$-tfMet35 aggregation monitored by ^{19}F NMR, CD, and AFM

The time evolution of the ^{19}F NMR spectra of Aβ$_{1-40}$-tfMet35 is noticeably different than the two-state kinetics seen for IAPP-tfmPhe23 as described in chapter 3 (20). Figures 4.3, 4.4, and 4.5 show peak intensity as a function of time for both samples. The singlet at 35.85 ppm in Figure 4.3 (the red dots in Figure 4.5) represents the monomeric peptide. In both the high and low concentration samples, the monomer concentration drops exponentially without a noticeable lag phase (10). This behavior is quite different from the behavior observed for IAPP-tfmPhe23. In IAPP-tfmPhe23, the kinetics for monomer consumption were sigmoidal; the intensity of the IAPP-tfmPhe23 monomer peak remained constant for a significant lag phase before dropping sharply (20). The sigmoidal kinetics observed for monomer depletion by ^{19}F NMR reflected the kinetics of fiber formation, with close correspondence between the rate of monomer depletion measured by ^{19}F NMR and CD measurements of secondary structure and ThT measurements of fiber formation (20). Similarly, time-lapse TEM images of fiber formation of IAPP-tfmPhe23 show only that the density of fibers increases as time progresses; non-fibrillar oligomers do not form a major population at any time (20).

For Aβ$_{1-40}$-tfMet35, on the other hand, it is clear that the pathway is more complex, with intermediates accumulating very early in the lag phase of amyloid formation (Figure 4.5). This is apparent from both analysis of the CD spectra and from the appearance of new peaks in the ^{19}F spectra. First, a slow conversion of peptide in the random coil conformation (200 nm) to another species characterized by a minimum at 205 nm in the CD spectrum occurs on roughly the same time scale as the decrease in peak intensity seen in ^{19}F NMR (Figure 4.5 and 4.6) in the low concentration sample. While the close correspondence between the kinetics of conformational
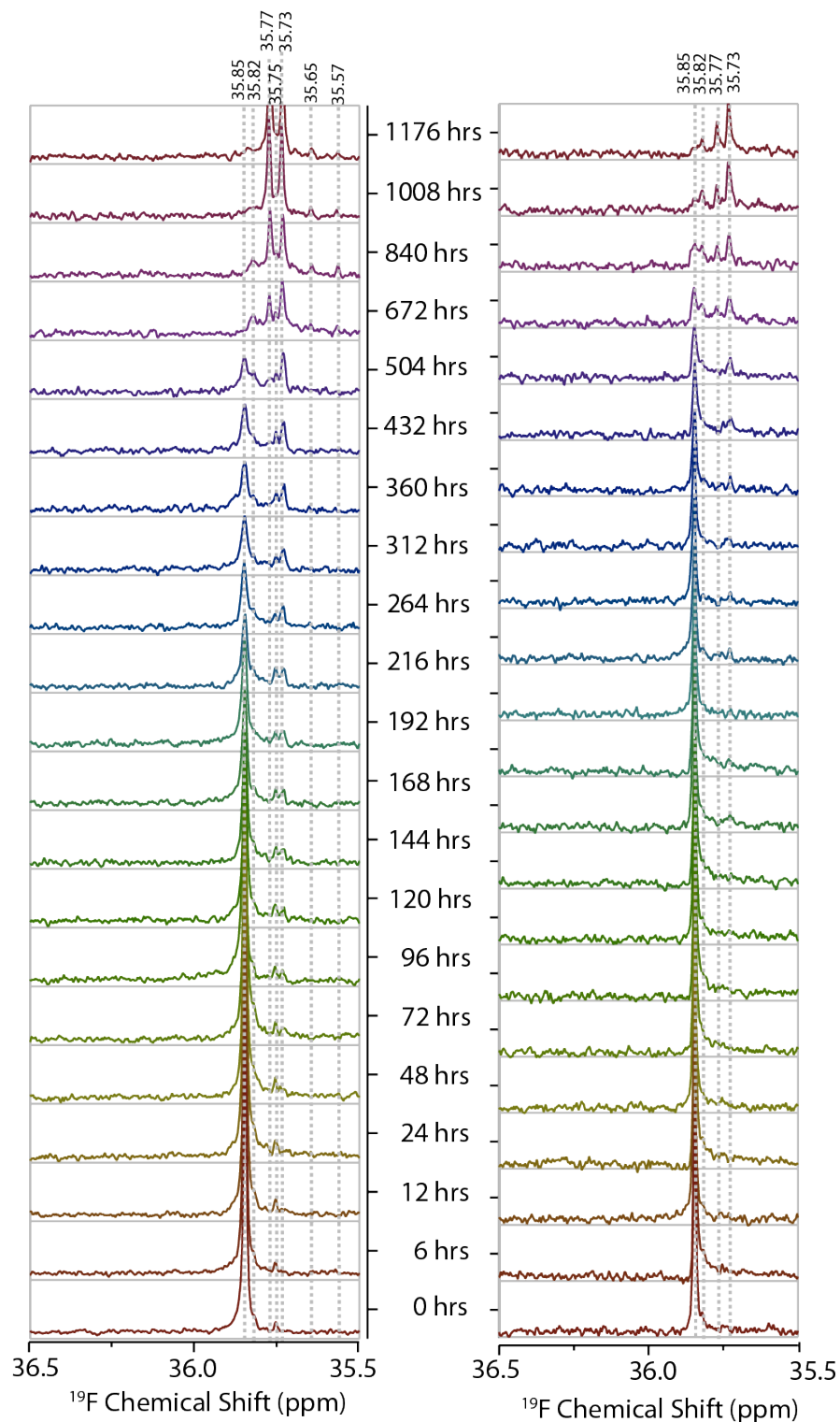
**Figure 4.3. Monitoring of Aβ$_{1-40}$-tfMet35 aggregation by ^{19}F NMR.** Samples at different concentrations (182 μM (left) and 46 μM (right)) are measured in parallel. The signal intensity of each spectrum was normalized to an internal TFE standard.

change and rate of monomer depletion is similar to the two state kinetics exhibited by IAPP-tfmPhe23, the minima at 205 nm do not correspond to the known CD spectra of $A\beta_{1-40}$ amyloid fibers (37). Instead, a minimum at 205 nm matches the CD spectra of several types of purified non-fibrillar oligomers of $A\beta_{1-40}$ (37).
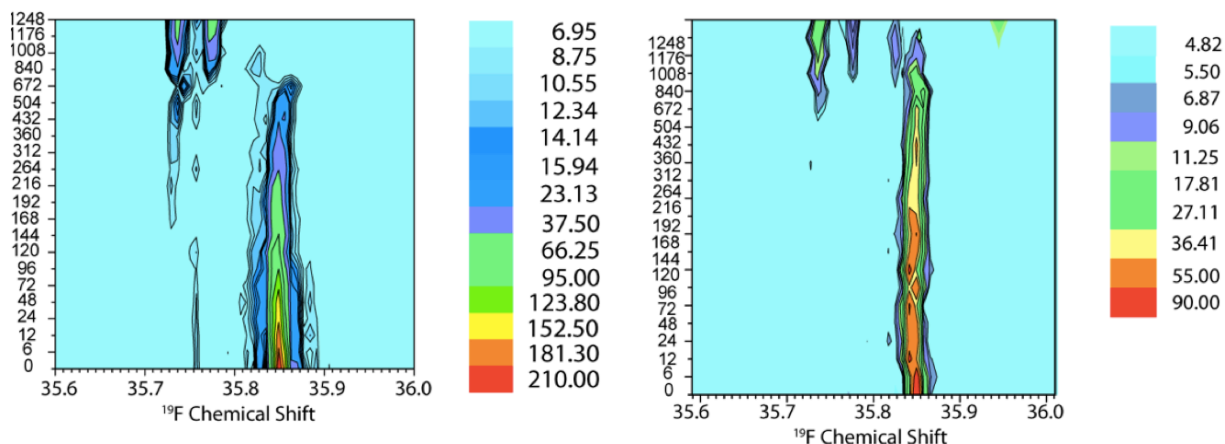
Figure 4.4. Contour plots of Figure 4.3. Time is labeled on the y-axis in hours.

Detection of oligomers by analysis of the CD spectra is more difficult in the high concentration sample. The CD spectrum at the initial time point for this concentration resembles the CD spectra of fibers due to the initial presence of protofibers in the sample (Figure 4.2e). Since the protofibers are not detected in the ^{19}F NMR experiment, any conformational changes within the protofibers would be reflected in the CD spectra but not in the ^{19}F NMR spectra. Similarly, the conversion of random coil monomers to random coil oligomers would be seen in the ^{19}F NMR spectra but not in the CD spectra. The combination of these two factors makes a quantitative analysis difficult. However, the CD spectra at high concentration of $A\beta_{1-40}$-tfMet35 change more rapidly than the ^{19}F NMR spectra, which likely some conversion of the NMR-invisible protofibers into a conformation with a larger fraction of β-sheet takes place.
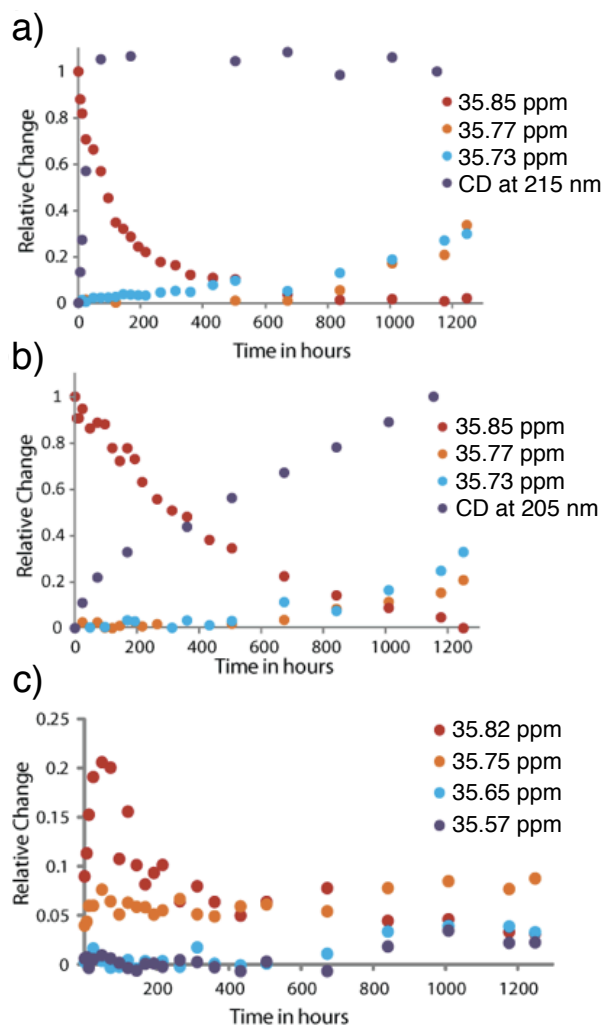
Figure 4.5. Kinetics of aggregation as followed by major and minor peaks in the ^{19}F NMR spectra and CD. (a) 182μM and (b) 46 μM Aβ$_{1-40}$-tfM$_{35}$ and (c) minor peaks in the 182μM sample. ^{19}F NMR values are normalized to the initial intensity of the monomer at 35.85 ppm. CD spectra are normalized to the initial and final values at 215 or 205 nm as indicated.

While analysis of the CD spectra does not directly show oligomer formation, direct evidence of early oligomer formation can be seen in the ^{19}F spectra. A small peak at 35.82 ppm can be seen as a shoulder of the monomeric peak at 35.85 ppm in both samples which resolves into a well-defined peak as the intensity of the monomer peak decreases (Figure 4.3). The intensity of this peak increases rapidly initially before reaching a maximum at 48 hours in both

samples and decaying (Figure 4.5c). This time profile is characteristic of a kinetic intermediate and suggests at least one type of non-fibrillar oligomer is formed early during the lag phase for amyloid formation.
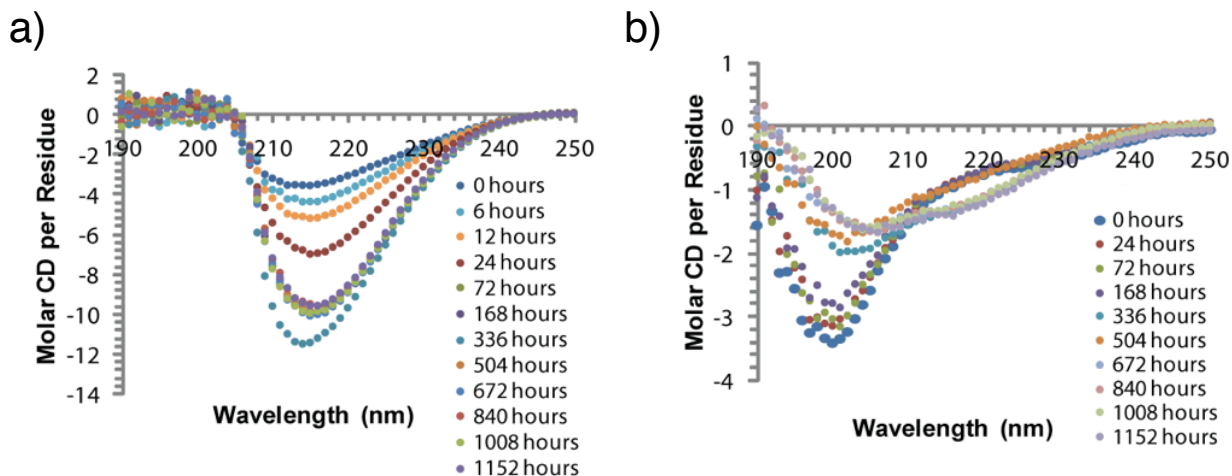
Figure 4.6. Time evolution of the CD spectra for (a) 182 µM and (b) 46 µM Aβ₁₋₄₀-tfMet35.

4.3.4. Characterization of Aβ$_{1-40}$-tfMet35 Aggregates After Monomeric Precursor Consumption

After the disappearance of the monomeric peak, both samples undergo a quiescent period in which the signal intensity of the ^{19}F NMR spectra is very low (from approximately 672-840 hours for the 46 µM sample and from approximately 400-672 for the 182 µM sample). After this period, two new peaks begin to appear in the ^{19}F NMR spectra of both samples. In the low concentration sample, two new peaks are clearly visible at 35.77 and 35.73 ppm (Figure 4.3 and 4.4). The same peaks are visible in the high concentration sample, as well as two minor peaks near 35.65 and 35.57 ppm. The AFM images taken after 12 hours and 45 days are similar (Figure

4.7), suggesting the aggregates corresponding to the new peaks are significantly smaller than the protofibers visible in the AFM images (Figure 4.2).

To characterize these new oligomeric peaks, we attempted to estimate the molecular weight of $A\beta_{1-40}$-tfMet35 aggregates by ultrafiltration and electrospray ionization ion mobility mass spectrometry (ESI-IMMS) experiments (Figure 4.8) (24, 38). The molecular mass corresponding to the new peaks was initially estimated by recording the ^{19}F NMR spectra of the low concentration sample following filtration through a series of ultrafiltration membranes (Figure 4.8a-c). Filtration through a 30 KDa cutoff membrane attenuated the signal, which was even more significant following filtration through a 100 KDa cutoff membrane. The degree of attenuation was significantly higher for the 35.73 ppm peak, indicating the aggregate corresponding to the 35.73 ppm peak is likely larger than the 35.77 ppm aggregate.
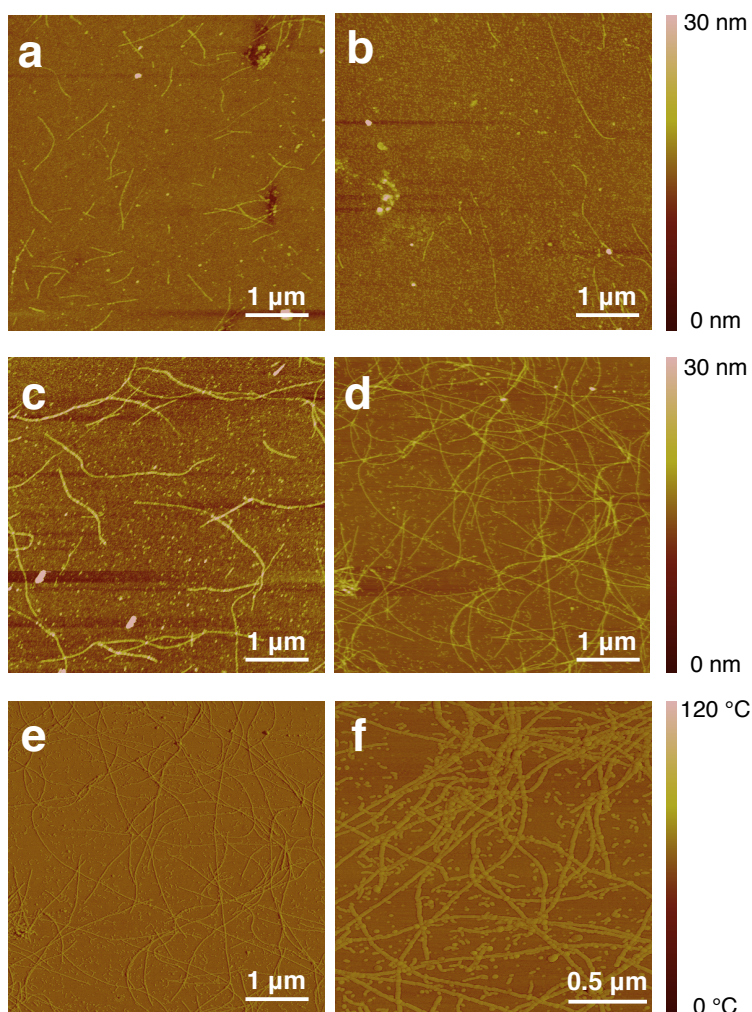
Figure 4.7. AFM images acquired during the aggregation of 182 μM Aβ$_{1-40}$-tfMet35 at the indicated times (a) Time 0 (Initial time point), (b) 6 hours, (c) 24 hours, and (d-f) at the end of time-course experiment. AFM images are taken for height (a-d) and phase (e-f).

ESI-IMMS experiments showed similar results (Figure 4.8d and e). The ESI-IMMS chromatogram of fresh samples of high concentration sample shows a single grouping of peaks corresponding to the +3 and +4 charge states of Aβ$_{1-40}$-tfMet35 along with sodium and sodium phosphate adducts (due to 20 mM phosphate buffer), consistent with a peptide that is monomeric after ionization. After 35 days (high concentration) or 52 days (low concentration) incubation and filtration through a 100 kDa filter, the monomeric peaks disappear and a broad set of peaks

corresponding to unresolved, high molecular weight oligomers is observed instead. These peaks

disappear after filtration through a 30 KDa cutoff membrane, consistent with the NMR results.

The filtration experiments therefore suggest both peaks correspond to aggregates between 30 and

100 KDa in size.
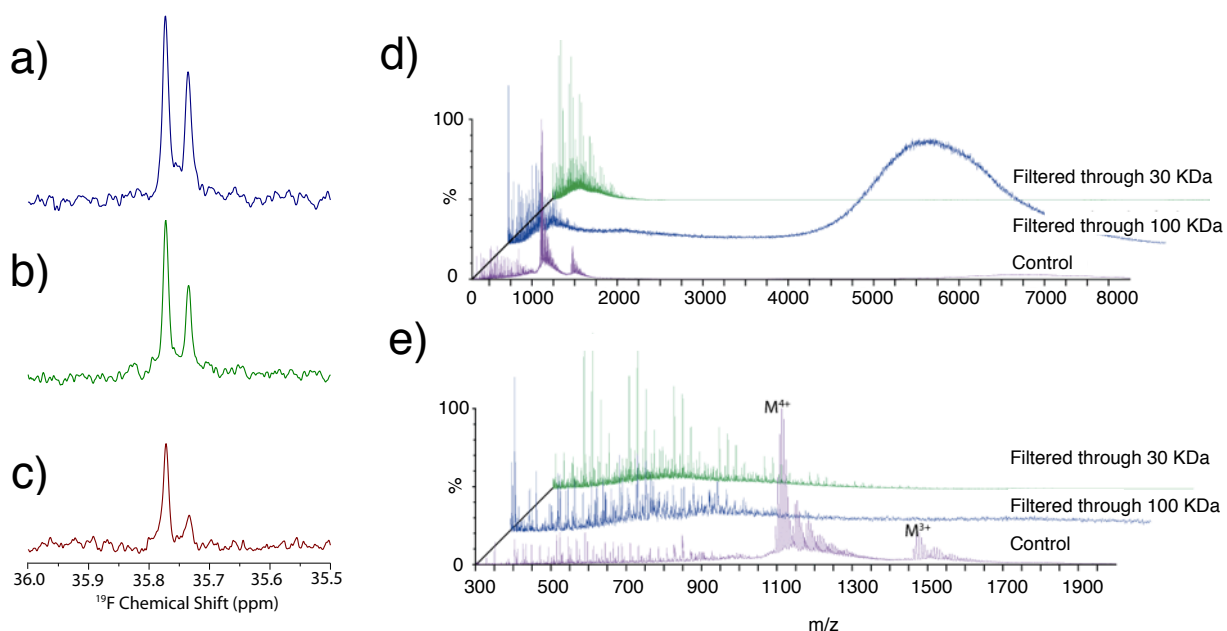
Figure 4.8. Size determination of oligomeric aggregates observed by ^{19}F NMR and ESI-IMMS. The low concentration sample (46 µM) at the end of time course experiment was acquired without filtration (a), after filtering through a 100 KDa cutoff membrane (b), or after a 30 KDa cutoff membrane (c). (d) ESI-IMMS chromatograms of 182 µM of $A\beta_{1-40}$-tfM$_{35}$ sample immediately after preparation (bottom), at the end of the aggregation experiment after filtration through a 100 KDa membrane (middle), and after filtration through a 30 KDa membrane (top). The peaks adjacent to the main peak represent sodium and sodium/phosphate adducts. (e) Zoom into 300 – 1900 m/z of (d).

The CD spectra at the final time-point show a large population of β-sheet structure,

particularly for the high concentration sample (Figure 4.6). However, the CD spectra also include

substantial contributions from large aggregates not visible in the ^{19}F NMR spectra. For this

reason, it is difficult to identify the secondary structure of the new peaks in the ^{19}F NMR spectra

from the CD spectra. Perturbation of the ^{19}F NMR spectra after introduction of an amyloid-

binding compound provided additional confirmation of the existence of β-sheets in the sample. Orange G is a derivative of Congo Red that specifically intercalates between stacked β-sheets (39). Addition of 5 equivalents of Orange G to the high concentration sample at the end of the aggregation experiment resulted in an immediate decrease of the peak at 35.73 ppm (Figure 4.9). Prolonged incubation resulted in the complete disappearance of the peak at 35.73 ppm. At the same time, the intensity of the peak at 35.77 ppm strongly increases. Since Orange G specifically binds to the interface between β-sheets, these changes suggest both peaks correspond to structures that contain a β-sheet binding site. The shift in intensity from 35.73 ppm to 35.77 ppm is suggestive of the inter-conversion of one type of oligomer to another by Orange G. Since the intercalation of Orange G is likely to disrupt the interface between β-sheets, the shift in the equilibrium towards the 35.77 ppm aggregate suggests the interface between β-sheets in the 35.77 ppm aggregate may be more exposed than in the 35.73 ppm aggregate. A similar type of disruption has been reported for $A\beta_{1-40}$ with another intercalating agent, in which it was shown that EGCG unfolds the C-terminal β-sheet but leaves the N-terminal β-sheet intact (40).
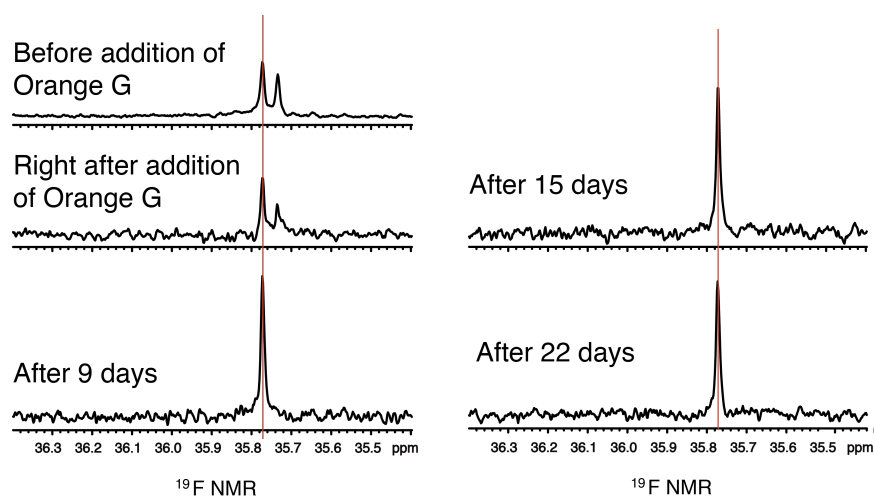
Figure 4.9. Binding of 5 equivalent orange G to aged samples of 182 µM $A\beta_{1-40}$-tfMet35 as followed by ^{19}F NMR. The signal intensity of each spectrum was normalized to an internal TFE standard.

Finally, I examined the solvent exposure of the Met35 side-chain by examining the influence of solvent isotope effect (H_2O/D_2O) on the ^{19}F chemical shift of Aβ_{1-40}-tfmMet35. Fluorine is weak hydrogen bond acceptor, and as such the ^{19}F nucleus is sensitive to isotope effects from exchange of H_2O to D_2O (20). The shift for both peaks at the end of the aggregation experiment is 0.06 ppm (Figure 4.10), which is similar to the shift for the trifluoroethanol internal standard (0.09 ppm). The D_2O exchange experiment therefore indicates tfmMet35 is relatively solvent exposed at this time point, at least for the fraction of the sample that shows a visible NMR peak. Notably, this result is not consistent with current triangular models of Aβ_{1-40} amyloid fibers, in which the C-terminus is sequestered within an internal cavity within the fiber (41, 42). However, it is consistent with several current models of smaller protofibers and non-fibrillar oligomers in which the Met35 side-chain is exposed (43).
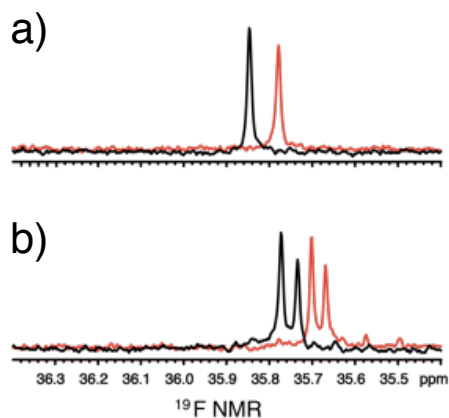
Figure 4.10. Solvent isotope effect on ^{19}F chemical shifts for freshly prepared (a) and aged samples (b). Black spectra show data in 10 % D_2O; red spectra show data in 70 % D_2O.

4.4. Discussion

Several oligomeric, non-fibrillar structures of Aβ$_{1-40}$ and Aβ$_{1-42}$ are highly neurotoxic, and as such, have been heavily investigated as downstream or upstream agents of Alzheimer's disease (25, 44). While detailed structural studies of Aβ oligomers are beginning to emerge (43, 45, 46), most structural and toxicity studies have by necessity required stable and relatively pure preparations of Aβ oligomers (47). Since the aggregation of Aβ naturally tends to lead to a heterogeneous mixture of oligomers and fibers, either purification steps or specialized conditions, such as the addition of SDS (48), low temperature (49), or chemical cross-linkers (37, 50), that are designed to trap specific oligomers are usually necessary for these studies. It is frequently difficult to observe the full pathway from monomeric peptide to oligomer species to the amyloid fiber form under these conditions. Purification also disturbs the equilibrium between Aβ species which can obscure the normal kinetic pathway. Therefore while these non-fibrillar structures are commonly referred to as "intermediates", the actual relationship of almost all non-fibrillar structures along the aggregation pathway is still poorly defined (51).

Elucidating the oligomeric aggregates in a pathway is often an essential step for understanding any biochemical process (51). The kinetics of amyloid formation typically shows a characteristic sigmoidal pattern; amyloid formation is slow or non-existent during an early lag phase before a period of rapid growth. The simplest model to explain this behavior is nucleation dependent polymerization, in which the lag-phase reflects the time for a critical concentration of energetically unfavorable nuclei to form. However, for a process as complex as amyloid formation many kinetic models are also consistent with an apparent lag phase (52). By directly monitoring the rate of monomer depletion during aggregation through ^{19}F NMR along with other biophysical techniques, we are able to show that the early phase of fiber formation actually

consists of at least two distinct steps. In the first step, the monomeric protein is almost entirely converted into a high molecular weight intermediate with a high β-sheet content and proto-fibrillar morphology that is not detectable by ^{19}F NMR. This step occurs without a discernible lag-phase at high temperature, in agreement with previous measurements of monomer depletion during Aβ$_{1-40}$ aggregation (10). This behavior is not consistent with a simple nucleation dependent polymerization model and suggests a more complex model involving an on- or off-pathway intermediate is necessary.

The appearance of multiple intermediates was directly detected in the ^{19}F NMR spectra. One particular type of oligomeric intermediate appears and disappears early in the experiment before the disappearance of the monomer. After the disappearance of this oligomer and a substantial delay, several different types of other low-molecular weight oligomers begin to appear that are in apparent coexistence with the proto-fibrillar species. At least two major types of oligomers between 30 and 100 kDa in size can be identified at this later stage based on the ^{19}F NMR signal and filtration experiments. The first species to appear is smaller than the second, later, oligomer detected, but both likely possess a β-sheet structure based on amyloid dye binding experiments. At least two more minor populations of oligomers in the second step of aggregation can also be detected in addition to these two major populations. A heterogeneous mixture of small oligomers therefore exists in pseudo-equilibrium with fibers and protofibers during early stages of aggregation.

4.5. Conclusion

^{19}F NMR was shown to be useful in the identification of oligomeric species of Aβ$_{1-40.}$ Both initial reversible oligomer formation and at least two types of non-reversible time-

dependent aggregation could be detected. It was also possible to show that one oligomer is larger than the other and furthermore that the rate of formation and relative yields of these oligomers was dependent on the starting concentration. These types of experimental measurements are difficult to perform by other techniques, and the additional level of detail obtained by measuring the rate of monomer depletion by NMR may prove fruitful for further characterization and screening. The presence of multiple oligomers revealed by our results could enable high-resolution structural studies of these species and also aid in the design of compounds to suppress of them.

4.6. References

1.   Harrison, R. S., Sharpe, P. C., Singh, Y., and Fairlie, D. P. (2007) Amyloid peptides and proteins in review, *Rev. Physiol. Biochem. Pharmacol. 159*, 1-77.

2.   Fandrich, M. (2007) On the structural definition of amyloid fibrils and other polypeptide aggregates, *Cell. Mol. Life Sci. 64*, 2066-2078.

3.   Jahn, T. R., Makin, O. S., Morris, K. L., Marshall, K. E., Tian, P., Sikorski, P., and Serpell, L. C. (2010) The Common Architecture of Cross-β Amyloid, *J. Mol. Biol. 395*, 717-727.

4.   Hamley, I. W. (2012) The Amyloid Beta Peptide: A Chemist's Perspective. Role in Alzheimer's and Fibrillization, *Chem. Rev. 112*, 5147-5192.

5.   Hardy, J. (2009) The amyloid hypothesis for Alzheimer's disease: a critical reappraisal, *J. Neurochem. 110*, 1129-1134.

6.   Hardy, J., and Selkoe, D. J. (2002) Medicine - The amyloid hypothesis of Alzheimer's disease: Progress and problems on the road to therapeutics, *Science 297*, 353-356.

7.   Hardy, J. A., and Higgins, G. A. (1992) Alzheimers-Disease - the Amyloid Cascade Hypothesis, *Science 256*, 184-185.

8.   Pryor, N. E., Moss, M. A., and Hestekin, C. N. (2012) Unraveling the Early Events of Amyloid-beta Protein (Aβ) Aggregation: Techniques for the Determination of Aβ Aggregate Size, *Int. J. Mol. Sci. 13*, 3038-3072.

9.   Mishra, R., Geyer, M., and Winter, R. (2009) NMR spectroscopic investigation of early events in IAPP amyloid fibril formation, *ChemBioChem 10*, 1769-1772.

10.   Yan, Y. L., and Wang, C. Y. (2006) Aβ 42 is more rigid than Aβ 40 at the C terminus: Implications for Aβ aggregation and toxicity, *J. Mol. Biol. 364*, 853-862.

11.   Cobb, S. L., and Murphy, C. D. (2009) ^{19}F NMR applications in chemical biology, *J. Fluorine Chem. 130*, 132-143.

12.   Kitevski-LeBlanc, J. L., and Prosser, R. S. (2012) Current applications of ^{19}F NMR to studies of protein structure and dynamics, *Prog. Nucl. Magn. Reson. Spectrosc. 62*, 1-33.

13.   Li, H., and Frieden, C. (2005) NMR studies of 4-[19]F -phenylalanine-labeled intestinal fatty acid binding protein: Evidence for conformational heterogeneity in the native state, *Biochemistry 44*, 2369-2377.

14.   Li, H., and Frieden, C. (2007) Observation of sequential steps in the folding of intestinal fatty acid binding protein using a slow folding mutant and ^{19}F NMR, *Proc. Natl. Acad. Sci. U.S.A 104*, 11993-11998.

15.   Li, H., and Frieden, C. (2007) Comparison of C40/82A and P27A C40/82A barstar mutants using ^{19}F NMR, *Biochemistry 46*, 4337-4347.

16.   Wang, G. F., Li, C., and Pielak, G. J. (2010) Probing the micelle-bound aggregation-prone state of α-synuclein with ^{19}F NMR spectroscopy, *ChemBioChem 11*, 1993-1996.

17.   Li, C., Lutz, E. A., Slade, K. M., Ruf, R. A., Wang, G. F., and Pielak, G. J. (2009) ^{19}F NMR studies of α-synuclein conformation and fibrillation, *Biochemistry 48*, 8578-8584.

18.   Li, C., Wang, G. F., Wang, Y., Creager-Allen, R., Lutz, E. A., Scronce, H., Slade, K. M., Ruf, R. A., Mehl, R. A., and Pielak, G. J. (2010) Protein ^{19}F NMR in Escherichia coli, *J. Am. Chem. Soc. 132*, 321-327.

19.   Schlesinger, A. P., Wang, Y., Tadeo, X., Millet, O., and Pielak, G. J. (2011) Macromolecular crowding fails to fold a globular protein in cells, *J. Am. Chem. Soc. 133*, 8082-8085.

20.   Suzuki, Y., Brender, J. R., Hartman, K., Ramamoorthy, A., and Marsh, E. N. G. (2012) Alternative Pathways of Human Islet Amyloid Polypeptide Aggregation Distinguished by [19]F Nuclear Magnetic Resonance-Detected Kinetics of Monomer Consumption, *Biochemistry 41*, 8154-8162

21.   Soong, R., Brender, J. R., Macdonald, P. M., and Ramamoorthy, A. (2009) Association of highly compact type II diabetes related islet amyloid polypeptide intermediate species at physiological temperature revealed by diffusion NMR spectroscopy, *J. Am. Chem. Soc. 131*, 7079-7085.

22. Vaiana, S. M., Ghirlando, R., Yau, W. M., Eaton, W. A., and Hofrichter, J. (2008) Sedimentation studies on human amylin fail to detect low-molecular-weight oligomers, *Biophys. J. 94*, L45-47.

23. Marek, P., Mukherjee, S., Zanni, M. T., and Raleigh, D. P. (2010) Residue-specific, real-time characterization of lag-phase species and fibril growth during amyloid formation: a combined fluorescence and IR study of p-cyanophenylalanine analogs of islet amyloid polypeptide, *J. Mol. Biol. 400*, 878-888.

24. Lee, J., Culyba, E. K., Powers, E. T., and Kelly, J. W. (2011) Amyloid-β forms fibrils by nucleated conformational conversion of oligomers, *Nat. Chem. Biol. 7*, 602-609.

25. Benilova, I., Karran, E., and De Strooper, B. (2012) The toxic Aβ oligomer and Alzheimer's disease: an emperor in need of clothes, *Nat. Neurosci. 15*, 349-357.

26. Jiang, L., and Burgess, K. (2002) Fluorinated and iodinated templates for syntheses of β-turn peptidomimetics, *Tetrahedron 58*, 8743-8750.

27. Duewel, H., Daub, E., Robinson, V., and Honek, J. F. (1997) Incorporation of trifluoromethionine into a phage lysozyme: Implications and a new marker for use in protein ^{19}F NMR, *Biochemistry 36*, 3404-3416.

28. Kieltsch, I., Eisenberger, P., and Togni, A. (2007) Mild electrophilic trifluoromethylation of carbon- and sulfur-centered nucleophiles by a hypervalent iodine(III)-CF3 reagent, *Angew. Chem. Int. Ed. 46*, 754-757.

29. Garner, D. K., Vaughan, M. D., Hwang, H. J., Savelieff, M. G., Berry, S. M., Honek, J. F., and Lu, Y. (2006) Reduction potential tuning of the blue copper center in Pseudomonas aeruginosa azurin by the axial methionine as probed by unnatural amino acids, *J. Am. Chem. Soc. 128*, 15608-15617.

30. Pelta, M. D., Barjat, H., Morris, G. A., Davis, A. L., and Hammond, S. J. (1998) Pulse sequences for high-resolution diffusion-ordered spectroscopy (HR-DOSY), *Magn. Reson. Chem. 36*, 706-714.

31. Stejskal, E. O., and Tanner, J. E. (1965) Spin Diffusion Measurements: Spin Echoes in the Presence of a Time-Dependent Field Gradient, *J. Chem. Phys. 42*, 288-292.

32. Hernandez, H., and Robinson, C. V. (2007) Determining the stoichiometry and interactions of macromolecular assemblies from mass spectrometry, *Nat. Protoc. 2*, 715-726.

33. Fawzi, N. L., Ying, J. F., Ghirlando, R., Torchia, D. A., and Clore, G. M. (2011) Atomic-resolution dynamics on the surface of amyloid-β protofibrils probed by solution NMR, *Nature 480*, 268-U161.

34. Fawzi, N. L., Ying, J. F., Torchia, D. A., and Clore, G. M. (2010) Kinetics of Amyloid β Monomer-to-Oligomer Exchange by NMR Relaxation, *J. Am. Chem. Soc. 132*, 9948-9951.

35. Pedersen, M. O., Mikkelsen, K., Behrens, M. A., Pedersen, J. S., Enghild, J. J., Skrydstrup, T., Malmendal, A., and Nielsen, N. C. (2010) NMR Reveals Two-Step Association of Congo Red to Amyloid β in Low-Molecular-Weight Aggregates, *J. Phys. Chem. B 114*, 16003-16010.

36. Nag, S., Sarkar, B., Bandyopadhyay, A., Sahoo, B., Sreenivasan, V. K. A., Kombrabail, M., Muralidharan, C., and Maiti, S. (2011) Nature of the Amyloid-β Monomer and the Monomer-Oligomer Equilibrium, *J. Biol. Chem. 286*, 13827-13833.

37. Ono, K., Condron, M. M., and Teplow, D. B. (2009) Structure-neurotoxicity relationships of amyloid β-protein oligomers, *Proc. Natl. Acad. Sci. U.S.A. 106*, 14745-14750.

38. Bernstein, S. L., Dupuis, N. F., Lazo, N. D., Wyttenbach, T., Condron, M. M., Bitan, G., Teplow, D. B., Shea, J. E., Ruotolo, B. T., Robinson, C. V., and Bowers, M. T. (2009) Amyloid-β protein oligomerization and the importance of tetramers and dodecamers in the aetiology of Alzheimer's disease, *Nat. Chem. 1*, 326-331.

39. Landau, M., Sawaya, M. R., Faull, K. F., Laganowsky, A., Jiang, L., Sievers, S. A., Liu, J., Barrio, J. R., and Eisenberg, D. (2011) Towards a Pharmacophore for Amyloid, *PLoS Biol. 9*, e1001080

40. del Amo, J. M. L., Fink, U., Dasari, M., Grelle, G., Wanker, E. E., Bieschke, J., and Reif, B. (2012) Structural Properties of EGCG-Induced, Nontoxic Alzheimer's Disease Aβ Oligomers, *J Mol Biol 421*, 517-524.

41. Paravastu, A. K., Leapman, R. D., Yau, W. M., and Tycko, R. (2008) Molecular structural basis for polymorphism in Alzheimer's β-amyloid fibrils, *Proc. Natl. Acad. Sci. U.S.A. 105*, 18349-18354.

42. Tycko, R. (2011) Solid-state NMR studies of amyloid fibril structure, *Annu. Rev. Phys. Chem. 62*, 279-299.

43. Stroud, J. C., Liu, C., Teng, P. K., and Eisenberg, D. (2012) Toxic fibrillar oligomers of amyloid-β have cross-β structure, *Proc. Natl. Acad. Sci. U.S.A. 109*, 7717-7722.

44. Fandrich, M. (2012) Oligomeric Intermediates in Amyloid Formation: Structure Determination and Mechanisms of Toxicity, *J. Mol. Biol. 421*, 427-440.

45. Scheidt, H. A., Morgado, I., and Huster, D. (2012) Solid-state NMR Reveals a Close Structural Relationship between Amyloid-β Protofibrils and Oligomers, *J. Biol. Chem. 287*, 22822-22826.

46.   Chimon, S., Shaibat, M. A., Jones, C. R., Calero, D. C., Aizezi, B., and Ishii, Y. (2007) Evidence of fibril-like β-sheet structures in a neurotoxic amyloid intermediate of Alzheimer's β-amyloid, *Nat. Struct. Mol. Biol. 14*, 1157-1164.

47.   Rosensweig, C., Ono, K., Murakami, K., Lowenstein, D. K., Bitan, G., and Teplow, D. B. (2012) Preparation of Stable Amyloid β - Protein Oligomers of Defined Assembly Order, *Amyloid Proteins: Methods and Protocols, Second Edition 849*, 23-31.

48.   Yu, L. P., Edalji, R., Harlan, J. E., Holzman, T. F., Lopez, A. P., Labkovsky, B., Hillen, H., Barghorn, S., Ebert, U., Richardson, P. L., Miesbauer, L., Solomon, L., Bartley, D., Walter, K., Johnson, R. W., Hajduk, P. J., and Olejniczak, E. T. (2009) Structural Characterization of a Soluble Amyloid β-Peptide Oligomer, *Biochemistry 48*, 1870-1877.

49.   Lambert, M. P., Barlow, A. K., Chromy, B. A., Edwards, C., Freed, R., Liosatos, M., Morgan, T. E., Rozovsky, I., Trommer, B., Viola, K. L., Wals, P., Zhang, C., Finch, C. E., Krafft, G. A., and Klein, W. L. (1998) Diffusible, nonfibrillar ligands derived from $A\beta_{1-42}$ are potent central nervous system neurotoxins, *Proc. Natl. Acad. Sci. U.S.A. 95*, 6448-6453.

50.   Yamaguchi, T., Yagi, H., Goto, Y., Matsuzaki, K., and Hoshino, M. (2010) A Disulfide-Linked Amyloid-β Peptide Dimer Forms a Protofibril-like Oligomer through a Distinct Pathway from Amyloid Fibril Formation, *Biochemistry 49*, 7100-7107.

51.   Cohen, S. I. A., Vendruscolo, M., Dobson, C. M., and Knowles, T. P. J. (2012) From Macroscopic Measurements to Microscopic Mechanisms of Protein Aggregation, *J. Mol. Biol. 421*, 160-171.

52.   Morris, A. M., Watzky, M. A., and Finke, R. G. (2009) Protein aggregation kinetics, mechanism, and curve-fitting: A review of the literature, *Bba-Proteins Proteom 1794*, 375-397.

Chapter 5

Conclusions and Future Directions

5.1. Conclusions

Fluorine is spin ½ nucleus, which exists in 100 % natural abundance, and has excellent NMR properties that are comparable to those of hydrogen. It also exhibits a wide range of chemical shifts that are sensitive to the surrounding chemical environment of ^{19}F nucleus. In addition, fluorine is rarely found in biological system, so there is no competition from background signals, which is often a problem when using nuclei such as ^{1}H, ^{13}C, and ^{15}N. Therefore, ^{19}F NMR is an invaluable tool for investigating structural changes and dynamics of proteins, as well as for examining the binding of ligands to proteins. With these attractive advantages, fluorine atom has been used as a tool to study proteins and peptides by incorporating fluorinated amino acid analogs (1-20) and fluorinated chemical labels (2, 21, 22). Using these advantages of ^{19}F NMR, I have examined the structure and dynamics of biologically active peptides, including antimicrobial peptides and amyloidogenic proteins.

5.1.1. Investigation of AMP Interaction with Lipid Bilayer Using ^{19}F NMR

The antimicrobial peptide MSI-78 was used as a model system for studying the interactions of bioactive peptides with membranes. Using a series of MSI-78 peptides that incorporate tfeGly **6**, a small and sensitive ^{19}F probe, local structural and dynamic changes that occur upon peptide binding to the lipid bilayer were investigated (23). The fluorinated MSI-78 analogs exhibited position-specific changes in ^{19}F chemical shift ranging from +1.28 to −1.35 ppm upon binding to lipid bilayer. The largest upfield shifts are associated with the most hydrophobic positions in the peptide. Changes in solvent isotope effects on ^{19}F chemical shifts were observed for the peptides that are consistent with MSI-78 forming a solvent-inaccessible hydrophobic core upon binding to the lipid bilayer. Transverse relaxation measurements of the ^{19}F nucleus, using the CPMG pulse sequence, were used to examine changes in the local mobility of MSI-78 that occurs on binding to the lipid bilayer. Positions in the hydrophobic core of the peptide-membrane complex show the greatest decrease in mobility, whereas residues that interact with lipid head groups are more mobile. The most mobile positions are at the N- and C-termini of the peptide. The various experiments by ^{19}F NMR including the changes in ^{19}F chemical shifts, solvent isotope effects on chemical shifts, and changes in ^{19}F longitudinal and transverse relaxation rates, provide support for the proposed mechanism of membrane disruption by MSI-78, and reveal new details of the dynamic changes that accompany membrane binding.

5.1.2. Investigation of Amyloid Fibril Formation Using ^{19}F NMR

Amyloid formation, a complex process involving many intermediate states, is proposed to be the driving force for amyloid-related toxicity in common degenerative diseases. Alternative pathways of aggregation were distinguished by using ^{19}F NMR to monitor monomer

consumption along with complementary measurements of fibrillogenesis. The utility of this technique is demonstrated by tracking amyloid formation in the type II diabetes-related IAPP as well as Alzheimer-related peptide $A\beta_{1-40}$.

A combination of ^{19}F NMR, ThT fluorescence assays, and CD spectroscopy were able to show that IAPP fibrillizes without an appreciable build up of non-fibrillar intermediates (24). To further demonstrate the utility of ^{19}F NMR, the influence of the polyphenolic amyloid inhibitor, EGCG, on the IAPP aggregation pathway was examined (24). Polyphenols have been shown to strongly inhibit amyloid formation in many systems. However, spectroscopic measurements of amyloid inhibition by these compounds can be severely compromised by background signals and competitive binding with extrinsic probes. The ^{19}F NMR studies described in this thesis suggest that ThT strongly competes with EGCG for binding sites on IAPP amyloid fibers. By comparing the rates of monomer consumption and fiber formation, it was found that EGCG stabilizes non-fibrillar large aggregates during fibrillogenesis.

In contrast to IAPP, studies on fluorine-labeled $A\beta_{1-40}$ peptide have shown the build-up of new signals corresponding to small oligomeric aggregates formed on the pathway to $A\beta_{1-40}$ fibrils. The concentration dependence of fiber formation was also investigated by ^{19}F NMR and correlated with structural changes determined by CD studies. In the presence of small oligomers detected by ^{19}F NMR, the co-existence of larger oligomers, protofibrils, and amyloid fibrils are also observed by AFM images. By providing an additional independent measurement of the rate of monomeric peptide consumption, a task that is difficult to accomplish by conventional methods, ^{19}F NMR can help differentiate between alternative pathways of aggregation for further investigation of amyloid formation pathway of other amyloidogenic peptides and proteins.

5.2. Future Directions

The research presented here provides valuable information to the field of protein and peptide structural changes and dynamics. These findings will hopefully contribute to the more widespread use of ^{19}F NMR in chemical biology.

For antimicrobial peptides, future work will aim toward using ^{19}F NMR to study peptide-membrane interactions *in vivo* at physiologically relevant concentrations as well as structural determination using solid-state ^{19}F NMR to examine interactions with whole bacterial cells. For amyloid peptide studies, ^{19}F NMR would be applicable for automated screening to find potential therapeutics in amyloid-related disorders. Although the throughput would be relatively slow, the lowering of false-positive rates would partially compensate for this. As well as AMPs, it would be very interesting to study peptide structural changes due to the interaction of membranes during amyloid fiber formation.

Since many techniques are available to incorporate fluorine probes into peptides and proteins, this technique would be applicable for proteins that are difficult to study with other techniques, either because of their size or because they adopt inherently disordered structures. The use of ^{19}F NMR for *in vivo* studies is a particularly attractive, but challenging, application due to the lack of fluorine in biological systems.

5.3. References

1. Cobb, S. L., and Murphy, C. D. (2009) ^{19}F NMR applications in chemical biology, *J. Fluorine Chem. 130*, 132-143.

2. Kitevski-LeBlanc, J. L., and Prosser, R. S. (2012) Current applications of ^{19}F NMR to studies of protein structure and dynamics, *Prog. Nucl. Magn. Reson. Spectrosc. 62*, 1-33.

3. Li, H., and Frieden, C. (2007) Comparison of C40/82A and P27A C40/82A barstar mutants using ^{19}F NMR, *Biochemistry 46*, 4337-4347.

4. Li, H., and Frieden, C. (2007) Observation of sequential steps in the folding of intestinal fatty acid binding protein using a slow folding mutant and ^{19}F NMR, *Proc. Natl. Acad. Sci. U.S.A. 104*, 11993-11998.

5. Li, H., and Frieden, C. (2005) NMR studies of 4-^{19}F-phenylalanine-labeled intestinal fatty acid binding protein: Evidence for conformational heterogeneity in the native state, *Biochemistry 44*, 2369-2377.

6. Schlesinger, A. P., Wang, Y., Tadeo, X., Millet, O., and Pielak, G. J. (2011) Macromolecular crowding fails to fold a globular protein in cells, *J. Am. Chem. Soc. 133*, 8082-8085.

7. Li, C., Wang, G. F., Wang, Y., Creager-Allen, R., Lutz, E. A., Scronce, H., Slade, K. M., Ruf, R. A., Mehl, R. A., and Pielak, G. J. (2010) Protein ^{19}F NMR in Escherichia coli, *J. Am. Chem. Soc. 132*, 321-327.

8. Wang, G. F., Li, C., and Pielak, G. J. (2010) Probing the micelle-bound aggregation-prone state of α-synuclein with ^{19}F NMR spectroscopy, *ChemBioChem 11*, 1993-1996.

9. Li, C., Lutz, E. A., Slade, K. M., Ruf, R. A., Wang, G. F., and Pielak, G. J. (2009) ^{19}F NMR studies of α-synuclein conformation and fibrillation, *Biochemistry 48*, 8578-8584.

10. Jackson, J. C., Hammill, J. T., and Mehl, R. A. (2007) Site-specific incorporation of a ^{19}F-amino acid into proteins as an NMR probe for characterizing protein structure and reactivity, *J. Am. Chem. Soc. 129*, 1160-1166.

11. Evanics, F., Bezsonova, I., Marsh, J., Kitevski, J. L., Forman-Kay, J. D., and Prosser, R. S. (2006) Tryptophan solvent exposure in folded and unfolded states of an SH3 domain by ^{19}F and ^{1}H NMR, *Biochemistry 45*, 14120-14128.

12. Evanics, F., Kitevski, J. L., Bezsonova, I., Forman-Kay, J., and Prosser, R. S. (2007) ^{19}F NMR studies of solvent exposure and peptide binding to an SH3 domain, *Bba-Gen. Subjects 1770*, 221-230.

13. Kitevski-LeBlanc, J. L., Evanics, F., and Prosser, R. S. (2009) Approaches for the measurement of solvent exposure in proteins by ^{19}F NMR, *J. Biomol. NMR 45*, 255-264.

14. Prosser, R. S., Luchette, P. A., Westerman, P. W., Rozek, A., and Hancock, R. E. (2001) Determination of membrane immersion depth with O_2: a high-pressure ^{19}F NMR study, *Biophys. J. 80*, 1406-1416.

15. Pomerantz, W. C., Wang, N., Lipinski, A. K., Wang, R., Cierpicki, T., and Mapp, A. K. (2012) Profiling the dynamic interfaces of fluorinated transcription complexes for ligand discovery and characterization, *ACS Chem. Biol. 7*, 1345-1350.

16. Anderluh, G., Razpotnik, A., Podlesek, Z., Macek, P., Separovic, F., and Norton, R. S. (2005) Interaction of the eukaryotic pore-forming cytolysin equinatoxin II with model membranes: ^{19}F NMR studies, *J. Mol. Biol. 347*, 27-39.

17.   Luck, L. A., and Falke, J. J. (1991) ^{19}F NMR-Studies of the D-Galactose Chemosensory Receptor. 1. Sugar Binding Yields a Global Structural-Change, *Biochemistry 30*, 4248-4256.

18.   Luck, L. A., Vance, J. E., O'Connell, T. M., and London, R. E. (1996) ^{19}F NMR relaxation studies on 5-fluorotryptophan- and tetradeutero-5-fluorotryptophan-labeled E-coli glucose/galactose receptor, *J. Biomol. NMR. 7*, 261-272.

19.   Buer, B. C., Chugh, J., Al-Hashimi, H. M., and Marsh, E. N. (2010) Using fluorine nuclear magnetic resonance to probe the interaction of membrane-active peptides with the lipid bilayer, *Biochemistry 49*, 5760-5765.

20.   Holzberger, B., Rubini, M., Moller, H. M., and Marx, A. (2010) A Highly Active DNA Polymerase with a Fluorous Core, *Angew. Chem. Int. Ed. 49*, 1324-1327.

21.   Klein-Seetharaman, J., Getmanova, E. V., Loewen, M. C., Reeves, P. J., and Khorana, H. G. (1999) NMR spectroscopy in studies of light-induced structural changes in mammalian rhodopsin: Applicability of solution ^{19}F NMR, *Proc. Natl. Acad. Sci. U. S. A. 96*, 13744-13749.

22.   Liu, J. J., Horst, R., Katritch, V., Stevens, R. C., and Wuthrich, K. (2012) Biased signaling pathways in β2-adrenergic receptor characterized by ^{19}F-NMR, *Science 335*, 1106-1110.

23.   Suzuki, Y., Buer, B. C., Al-Hashimi, H. M., and Marsh, E. N. G. (2011) Using Fluorine Nuclear Magnetic Resonance To Probe Changes in the Structure and Dynamics of Membrane-Active Peptides Interacting with Lipid Bilayers, *Biochemistry 50*, 5979-5987.

24.   Suzuki, Y., Brender, J. R., Hartman, K., Ramamoorthy, A., and Marsh, E. N. (2012) Alternative Pathways of Human Islet Amyloid Polypeptide Aggregation Distinguished by [19]F Nuclear Magnetic Resonance-Detected Kinetics of Monomer Consumption, *Biochemistry 51*, 8154 – 8162.